Optimisation of Signal-to-Background Ratio for Thermal Neutron Detectors

PhD Thesis

Eszter Dian

Supervisor : Dr. Péter Zagyvai
Consultants: Dr. Szabolcs Czifrus
Prof. Dr. Richard Hall-Wilton

HAS Centre for Energy Research
Budapest University of Technology and Economics

Budapest
2019

List of Acronyms

CNCS Cold Neutron Chopper Spectrometer

CSPEC Cold Chopper Spectrometer

DMSC Data Management and Software Centre

ESS European Spallation Source

ILL Institut Laue-Langevin

LHC Large Hadron Collider

LINAC LINear ACcelerator

MCNP Monte Carlo N-Particle

MCPL Monte Carlo Particle List

NAA Neutron Activation Analysis

NGR Neutron-to-Gamma Response ratio

PGAA Prompt Gamma Activation Analysis

SANS Small Angle Neutron Scattering

SBR Signal-to-Background Ratio

SNS Spallation Neutron Source

TAS Triple Axes Spectrometer

ToF Time-of-Flight

T-REX Time-of-flight Reciprocal space Explorer

VOR Versatile Optimal Resolution chopper spectrometer

Contents

Part I

Introduction

Chapter 1

Introduction

Scientific research in many fields from fundamental physics to biology, from climate research to archaeology has achieved great progress in the last decades, thanks to highly-advanced material testing methods. Large-scale material testing instruments became undoubtedly essential tools of modern research. One of these techniques is neutron scattering, which has become widely applied in Europe and world-wide. Nowadays, more than 20 neutron sources enable access to various neutron scattering techniques in Europe. A great effort has been continuously invested for decades in developing novel solutions for keeping and extending the availability of these techniques, maintaining and updating the current instruments and installing new ones in the race for higher performance, efficiency and resolution. The current flagship of this endeavour is the European Spallation Source (ESS) ERIC, which is currently being built in Lund, Sweden, by the joint effort of 17 European member countries.

The ESS has the goal to become the world's leading neutron source for the study of materials by the second quarter of this century [1, 2]. It is going to be the brightest neutron source in the world, serving instruments beyond the limits of the current state-of-the-art.

With this, the ESS will employ an unprecedented set of instrumentation, offering unique investigative power for insight at the molecular or atomic level of matter, that is essential in many current research fronts. Including, but not limited to energy science, ESS will provide an important analytical tool for the exploration of promising novel materials for more effective energy management, e.g. for solar cells, batteries, fuel cells, thermoelectric materials for waste-heat recovery and refrigeration, and reversible hydrogen storage materials for safe usage of hydrogen as an energy carrier. Also for health sciences, with a novel macromolecular diffractometer the ESS opens new frontiers for the study of mechanics of diseases, molecular dynamics, taking part in the development

of novel treatments, effective pharmaceuticals, as well as potential new materials for implants and health-care devices. Other neutron methodologies, like neutron imaging will also benefit from the unique brightness the source, serving research in various fields of science, e.g. archaeology and cultural heritage, or agriculture. A promising project for the latter is the neutron imaging based whole-plant water-uptake analysis. Moreover, as the instrumentation is already challenged at the current neutrons sources, they will also benefit from the ESS-related developments.

The goal of exceeding the limits of the current state-of-the art and the unprecedented neutron yield of the ESS source challenge all aspects of instrument development, especially detectors. Fifteen instruments of various types are developed in parallel in the first phase of the construction, with unique scopes and requirements to face, challenging the scientists to renew their approach, develop new tools and open new frontiers to provide detectors, which can harness the potential of this immense initiative.

1.1 The neutron detector challenge and the ^{3}He-crisis

The challenge that the ESS Detector Group and their partners have to face is that multiple detectors have to be developed at the same time for various instruments, all with different driving requirements [2]. One key feature of the ESS is the unprecedented high incident neutron flux, that enables to study more, or smaller samples, and more phase space, but it also challenges the count rate capability of the detectors. This is a controversy for detectors of Small Angle Neutron Scattering (SANS) instruments and reflectometers, as for these applications the nominal count rate requirement of ESS exceeds the state-of-the-art by 1–2 and 2–3 orders-of-magnitude, respectively. Other challenges are also mostly set by scientific motives. These lead to a need for larger detector areas in case of e.g. direct geometry spectrometers and SANS instruments, and for 2–4 times better spatial resolution for SANS, reflectometry and diffraction. To fulfill all these requirements is a major task in itself, but external circumstances increased the challenge.

One of the traditionally common neutron detectors for scattering experiments has been the ^{3}He-filled proportional counter. This has been widespread due to the excellent neutron absorption and chemical properties (i.e. non-toxic, inert, etc.) of ^{3}He, the simplicity of the technique, as the neutron converter also serves as the counting gas, and the affordable price and availability of the ^{3}He. ^{3}He is produced as a by-product of the fabrication of nuclear missiles; the tritium used in the warhead decays to ^{3}He

with 12.33 year half-life [3], and it has to be purified regularly. Therefore the two major suppliers are USA and Russia. Due to its by-product nature, on one hand, the production of ^{3}He has not been correlated to the demand and the production has exceeded the need for decades, producing a stockpile, although the production decreased with the number of nuclear weapons to be refurbished. On the other hand, the price used to be artificially suppressed, not exceeding 100–200 USD/l, and does not represent production costs [4]. As a consequence, the application of ^{3}He has spread in scientific research (nuclear measurements, cryogenic studies), medical applications (polarised MRI) and nuclear safeguards and security.

However, the events of 9/11 compelled the US Government to increase homeland security, realised as installation of radiation, especially neutron monitors on state and interstate boundaries all over the US [4]. This led to a sudden increase of demand of ^{3}He. Due to this increased demand coming from US homeland security, and the continuously increasing demand of the other afore-mentioned applications, the demand exceeded the yearly production of ^{3}He, resulting in the drastic decrease of the stockpile by 2008. The recognition that the stockpile could be exhausted resulted in restrictions in availability of ^{3}He and the litre price increased by more than an order-of-magnitude. This is the so-called '^{3}He-crisis' [4]. This phenomenon highly affected the whole neutronic community, as well as the construction of ESS. The decision was made that alternative technologies should be applied wherever it is reasonably achievable, without significant decrease of scientific value, and ^{3}He should be saved for applications without sufficient substitute technology.

The ESS in general set the scope on developing alternative detectors wherever it is reasonable, and invested great effort in R&D. A global effort is made by the neutronic community, and one of the most potent alternative is an old, but rarely used technology, the solid boron carbide (B_4C) based detector, used typically with Ar/CO_2 as counting gas [5, 6]. These detectors are developed with the joint effort of several institutes [7–10], including the ESS. To face this challenge the ESS Detector Group developed tools and infrastructure in order to support the development and manufacturing of these new detectors: a 'coating workshop' has been installed co-located close to the Linköping University [10], providing B_4C coatings [11–13], a workshop has been set up for manufacturing prototypes and future detectors, and a robust simulation framework has been developed to support the developments with advanced Monte Carlo simulation studies.

The need for a ^{3}He-substitute technology is the major challenge for e.g. the chopper spectrometers as these instruments require large area detectors with large volume

of counting gas. A potent alternative for the commonly used ^{3}He-tubes for these instruments is the so-called 'Multi-Grid' detector [14, 15], invented at the Institut Laue-Langevin (ILL) [8] and now jointly developed by ESS and ILL. This is an Ar/CO_2-filled proportional chamber with a solid B_4C-converter. However, the application of new materials and structures in high neutron flux raise new questions and may result in new issues to face. The current work takes part in exploring the issues of these re-discovered technologies, especially the Multi-Grid detector, from the aspect of neutron-induced detector background, and its effect on the Signal-to-Background Ratio (SBR).

1.2 The European Spallation Source

The ESS aspires to be the world's brightest neutron source (see Figure 1.1), and the flagship of material studies by the second quarter of this century [2]. The ESS design includes the newest developments in terms of source e.g. an unprecedented 5 MW power proton linear accelerator (LINAC), and the first application of a 'butterfly moderator' [16], in order to maximise the neutron yield, or instrument components, like the currently developed Multi-Blade detector [17], providing submillimetre spatial resolution, far beyond the current state-of-the-art. With the unique characteristics of the source, the sophisticated instrument designs and the novel integrated scientific and computing infrastructure ESS pushes the frontiers of neutron science. Moreover, a Data Management and Software Centre (DMSC) is also established, with the aim of providing user-centred software for instrument control, efficient data reduction, real-time data, visualisation, intuitive data analysis and computational support for modelling and simulations, establishing a new standard for neutron facilities.

The ESS is a pulsed neutron source, where the neutrons are produced from the spallation reaction of the accelerated protons hitting a tungsten target, producing ∼20 neutrons/reaction. It is a specific, 'long-pulsed' source with a 2.86 ms neutron pulse length (for 36.4 meV or 1.5 Å neutrons) and a 14 Hz pulse-repetition rate [2], being a significant contributor to the unique neutron yield of ESS.

The protons are accelerated to 2 GeV (∼96% of the speed of light) by a ∼600 m long LINAC, and deposit 5 MW power in the target. In order to prevent heat damage, the target is a segmented, rotating wheel with He-cooling. The rotation of the wheel matches the frequency of the proton source, so each incoming proton pulse hits a new segment, leaving time for cooling. The wheel is 2.6 m in diameter, and contains 3 tons of tungsten in a form of 6840 itsy-bitsy (24 cm^3) 'bricks', placed inside stainless steel cassettes, so the coolant flows in the gaps between the bricks. This is the first

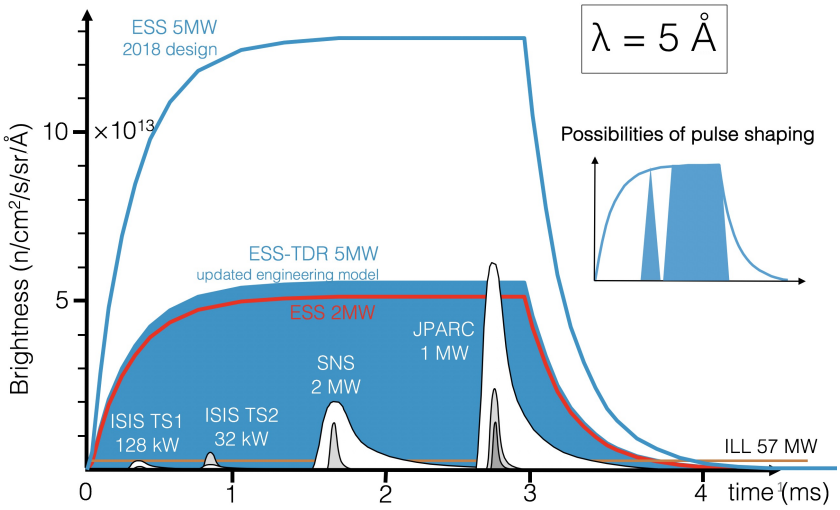

Figure 1.1: Brightness of ESS by original and current design, in comparison with presently operating other neutron sources. Figure courtesy of ESS [18].

high-power spallation source to employ a helium-cooled rotating target. The target is planned to be replaced every 5 years.

The neutrons are extracted from the target through a low dimensional (i.e. 3 cm and 6 cm thin) bi-spectral moderator [16], placed above and below the hot spot of the irradiated segment. The moderator serves 42 (potential) beam ports with different neutron spectra: thermal neutrons cooled by 300 K water ('body') and cold neutrons cooled by 20 K para-hydrogen ('wings'), as it is particularly transparent for cold neutrons. The novel geometry and the application of high-purity para-hydrogen are also major contributors to the unseen brightness of ESS.

The ESS is planned to serve 22 neutron scattering instruments of various types e.g. SANS instruments, direct and indirect geometry inelastic spectrometers, diffractometers, etc. Fifteen of them are currently under development, including the two planned direct geometry spectrometers, that are the focus of the current thesis from the aspect of detector development.

1.2.1 Direct geometry spectrometers at ESS

Inelastic neutron scattering is a very powerful technique for exploring atomic and molecular motion, as well as magnetic and crystal field excitations [19]. In these experiments, the sought-after information is carried by the energy- and momentum transfer between the neutrons and the sample as the vibrational modes are directly connected to energy transitions. The two families of the inelastic instruments are the Triple Axes Spectrometers (TAS) and the ToF instruments (chopper spectrometers), like the di-

rect geometry chopper spectrometers. The main difference between the two families is that in the TAS instruments the initial and final neutron energy is determined (selected) by crystal monochromators, therefore,the recording of a single spectrum is a time-consuming process. On the other hand, in ToF spectrometers the final (direct geometry) or initial neutron energy (indirect geometry) is derived from the measured neutron ToF, allowing a broad phase space to be measured in a single setting; this is typically achieved with a large area detector array [20]. These instruments are equipped with 2–4 m high, large area cylindrically arranged detectors, with an average of 3–4 m radius (i.e. sample-detector distance), covering ∼180° in angle in the horizontal plane (see Section 1.2). As the inelastic signals are orders-of-magnitude lower than the elastic ones, one of the main performance criteria of these spectrometers is typically defined by the Signal-to-Background Ratio (SBR).

Figure 1.2: Schematic design of the CSPEC chopper spectrometer at ESS, involving the target station and the bunker, the choppers and the detector. Figure is adopted from [21].

In direct geometry spectrometers the initial neutron energy is defined by the chopper system, while the final neutron energy is derived from directly measured quantities, i.e. the ToF and the detection coordinates of the neutrons. The ToF measurement is triggered by a chopper signal, and measured up to the detection point. The ToF for the chopper-sample distance is pre-calculated from the initial neutron energy and the geometry, extracted from the total measured ToF, and with this the sample-to-detection ToF is determined. The final neutron energy is derived from this ToF, and the hypothetical flight distance, i.e. the shortest, straight line between the sample and the detection coordinates. With this the energy transfer can be obtained as $E_{trf} = E_{initial} - E_{final}$, and the momentum transfer can also be determined from detection coordinates. Due to

this, the ToF and position resolution of the detector directly affect the energy resolution of the instrument.

Two direct geometry instruments are decided to be installed among the 22 baseline ESS instruments, the CSPEC Cold Chopper Spectrometer and the T-REX Bispectral Chopper Spectrometer. These instruments are currently under construction, planned to be realised within the first 15 instruments. They are expected to contribute to a plethora of fundamental and applied research fields, e.g. energy storage, environmental and health sciences, material sciences, etc. One of the key features is the in situ following of kinetic events, and therefore structures, dynamics. The functionality of large hierarchical systems can be studied, e.g. as inelastic scattering is particularly well-applicable for hydrogen, proton-kinetics can be studied in proteins and other biological samples, as well as quantum materials, functional and battery materials, including but not limited to catalysis metals, ion-transport materials, fuel cell membranes, nanomaterials, thermo-electric and magneto-caloric materials, etc. CSPEC aims at the large user community of soft condensed matter, while T-REX mainly serves the quantum phenomena and materials science community.

All these studies are becoming feasible thanks to the high performance of the instruments. Both CSPEC and T-REX are long instruments with 160 and 170 m source-sample distance, respectively. CSPEC operates with 0.5–20.5 meV incident neutron energy, optimised at 5.1 meV (4.0 Å), while T-REX is a thermal instrument with 2–160 meV incident neutrons. One of the key features of both instruments is the excellent energy resolution, 1–3%, and 1–6% respectively, depending on the energy region. Beside that, CSPEC provides a high, $10^5 - 10^6 \frac{\mathrm{n}}{\mathrm{cm}^2\ \mathrm{s}}$ neutron flux, while T-REX can operate in polarised and non-polarised mode. Both instruments are planned to be equipped with large area Multi-Grid detectors, e.g. with 3.5 m radius and 170° angular coverage of the detector in the CSPEC. Both instruments exceed the limits of the state-of-the-art chopper spectrometers, and their main challenge is the debut of the novel, ^{3}He-substitute Multi-Grid detector.

The current thesis takes part in the development of this solid boron carbide based detector, with the aim to optimise the Signal-to-Background Ratio (SBR) via the development of advanced detector shielding. To this end, the following content structure is organised: the principles of neutron detection and gaseous detectors are summarised in Chapter 2. Here the Ar/CO_2-filled Multi-Grid detector is also introduced, among with the phenomenon of Ar activation in nuclear facilities. The current work is targeted to explore neutron-induced gamma and neutron background in the detector, as well as the neutron-induced activity, distinguish the sources of background, and develop a

complex shielding design for background suppression. These objectives are summarised in Chapter 3. The studies are performed with the MCNP and Geant4 Monte Carlo codes and analytical calculations, as introduced in Chapters 4 and 5, respectively. The implemented detector models are described in Chapter 6. The gamma background and the activation are studied with MCNP simulations and analytical calculations (see Chapter 7), while the scattered neutron background is studied with Geant4 modeling. The model is validated and the scattered neutron background is studied in Chapter 8. Subsequently the model is applied for shielding design and optimisation of SBR in Chapter 9. Finally all the results are concluded in Chapter 10.

Chapter 2

Overview of State-of-the-Art

2.1 Neutron detection

Neutron detectors have a long history in various fields from safeguards to large-scale scientific experiments. A plethora of different detection methods has been invented since the discovery of neutrons either for counting or for dosimetry, spectroscopy and other applications.

2.1.1 Principles of neutron detection

Neutron detection requires a different approach from commonly measured ionising particles, as the neutron is a neutral, indirectly ionising particle. Therefore neutrons are usually not directly detected, but converted into ionising charged particles, for which classical detector types e.g. proportional counters, scintillators etc. can be applied. The potential neutron conversion reactions highly depend on the neutron energy and therefore different detectors should be applied for slow and fast neutron detection, i.e. below and above the 0.5 eV cadmium cutoff. The reactions applied for neutron conversion are the neutron absorption (emitting proton or α-particle), neutron-induced fission and elastic scattering with recoil particles. The most commonly used reaction for slow neutron detection is the absorption, where target nuclei should have a high absorption cross-section, like the ^{157}Gd, which has a 255000 barn neutron absorption cross-section for thermal neutrons, and other lanthanides, light isotopes such as ^{3}He, ^{10}B and ^{6}Li, or fissile isotopes like ^{233}U, ^{235}U and ^{239}Pu [22]. The choice of reaction highly depends on the neutron energy, as well as the specific requirement of the measurement. The conversion reactions and cross-sections are presented in Table 2.1 for the most widely used target nuclei.

The conversion of slow and fast neutrons have two major differences. On one hand,

Table 2.1: Conversion reactions for slow neutron detection. Data imported from [23].

Reaction	Conversion particles	σ [barn] at 25 meV
$^{3}\mathrm{He}(\mathrm{n},\mathrm{p})^{3}\mathrm{H}$	p, ^{3}H	5400
$^{10}\mathrm{B}(\mathrm{n},\alpha)^{7}\mathrm{Li}$	α, ^{6}Li	3480
$^{6}\mathrm{Li}(\mathrm{n},\alpha)^{3}\mathrm{H}$	α, ^{3}H	937

as the energy of slow neutrons is equal or lower than that of their environment and the target material, there is no direct access to the neutron energy in slow neutron detection. Therefore the energy measurement used for indirect neutron spectroscopy can be performed via the measurement of other quantities, e.g. ToF, while for fast neutrons direct neutron spectroscopy is feasible with recoil nuclei of inelastic scattering. On the other hand, the absorption cross-sections of the conversion reactions mostly follow the $\frac{1}{v}$ rule, where v is the velocity of neutron, and therefore their efficiency is much lower for fast neutrons – except in the resonance interval, if it exists, – which affects the detector efficiency as well. In order to increase the efficiency, fast neutrons are often thermalised before detection via scattering on a hydrogen-rich medium. As the ESS provides thermal and cold neutrons, the focus in the following is on slow neutron detection.

The converter materials and reactions shown in Table 2.1 above are used in various neutron detectors. The most widely-used detectors are the gaseous proportional chambers, which have two main types depending on the aggregate of the converter. In case of gaseous converters, such as the ^{3}He or the enriched $^{10}BF_3$, the converter acts as the counting gas as well. These detectors traditionally have simple design and high total efficiency. The other type of detectors are built with a solid converter layer and filled with a conventional counting gas, like the Ar/CO_2 mixture. Obtaining a high efficiency with these detectors is more difficult; the total efficiency is determined by *a)* the conversion efficiency, for which a thick converter layer is preferred to increase the probability of absorption, *b)* the escape-probability of the ions, for which a thin converter layer is advantageous so the conversion particles can leave the layer and enter the sensitive gas volume, and *c)* the detection efficiency of the conversion products. Besides that, a wider range of converter materials are applicable as solid lining, and therefore these detectors can be more tailored to specific requirements (e.g. threshold reactions) than those with gaseous converters. However, all these detectors also maintain the advantages of the gaseous particle detectors, and are the dominant detectors in neutron scattering experimentation.

2.1.2 Gaseous detectors

The gaseous ionisation chamber is one of the most common radiation detectors. The ionisation chamber itself is a gas filled tank that contains two electrodes with DC voltage [23, 24]. The detection method is based on the collision between atoms of the filling gas and the photons or charged particles to detect, during which electrons and positively charged ions are produced. Due to the electric field between the electrodes, the electrons drift to the anode, inducing a measurable electrical signal. However, this measurable signal is very low for discrete particle detection, therefore typically additional wires are included and higher voltage is applied in order to obtain a gain on the signal. In the higher electric field the drifting charged particles gain enough energy for ionisation, producing secondary charged particles, whose number, and therefore the measured signal is sufficiently high, and still proportional to the energy of the measured particle; these are the so-called proportional chambers [5, 6]. Proportional chambers and other gaseous detectors are widespread in many applications from monitoring to large-scale experiments, thanks to their low price, reliability and simplicity.

2.1.3 The Multi-Grid detector

The Multi-Grid [14] is a large area gaseous detector designed for chopper spectroscopy, providing an alternative solution for the currently used ^{3}He-tubes. The Multi-Grid design was invented at the Institute Laue-Langevin (ILL) [8, 25, 26], and the detector now is jointly developed by the ILL and the ESS within the CRISP [27] and BrightnESS [28] projects.

It is an Ar/CO_2-filled proportional chamber with a solid boron-carbide ($^{10}B_4C$) neutron converter, enriched in ^{10}B [11–13]. The basic unit of the Multi-Grid detector is the so-called 'grid' [14], an aluminium frame, which has a low absorption and scattering cross-section for neutrons. Thin aluminium lamellas, the so-called 'blades' are placed in this frame. The series of blades are parallel with ('short blades') or orthogonal to ('long blades') the entrance window of the grid, dividing the grid into cells, as it is shown in Figure 2.1. These blades, either the short blades only, or all of them are coated on both sides with a 0.5–1.5 μm boron-carbide converter layer.

The thickness of the layers is optimised so that the charged particles (α, ^{7}Li) produced in the neutron capture can leave the converter and reach the counting gas with enough energy to be detected, as it is shown in Figure 2.2. This is around 1 μm for thermal neutrons, but for this thickness the conversion efficiency of a single layer is small, $\sim 5\%$ for thermal neutrons. The conversion efficiency can be increased with the

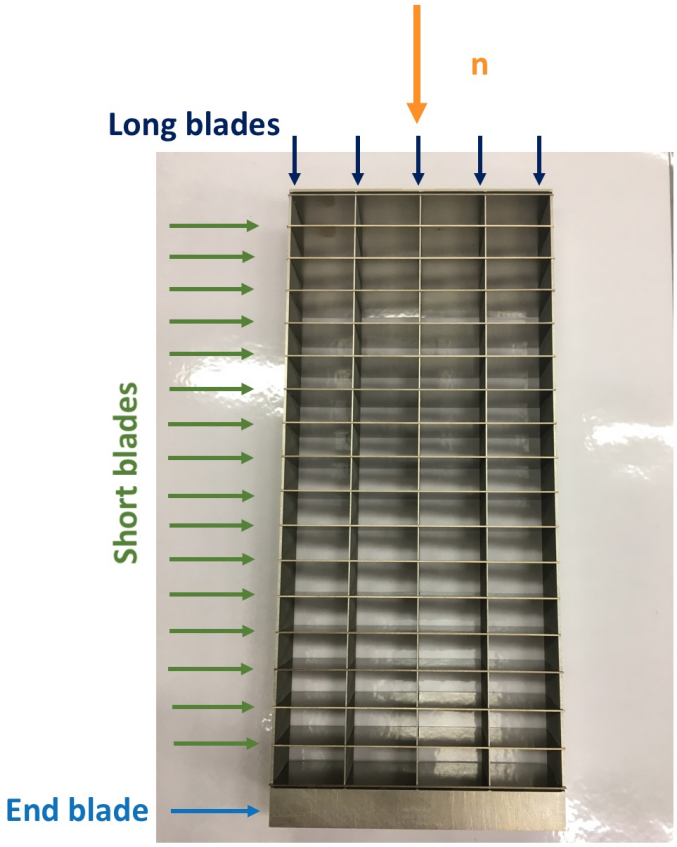

Figure 2.1: Early design aluminium grid of Multi-Grid detector with 4 × 17 cells [14]. An incoming neutron beam indicated in orange, entering at the grid window surface. The so-called 'long blades', marked with black are parallel to the beam, while the 'short blades', marked with green, are orthogonal to it. The 'end blade' with blue marking is a ∼1 cm thick aluminium block at the rear of the grid, interfacing with the read-out electronics.

application of multiple converter layers. With the utilisation of a typical number of 30 B_4C layers in a single grid, a detection efficiency comparable with that of ^{3}He-tubes can be reached [14]. The key advantage of the described grid structure is that both the short and the long blades can be coated before being placed in the basic frame of the grid, leaving a great variability of the coating design.

These grids are stacked, forming 3–4 m high columns. The grids are electrically insulated from one another and serve as cathodes. Anode wires go through the length of the columns in the channels formed by the cells in each grid. The anodes and cathodes can either be grouped or read out individually, depending on the time and position resolution requirements of the measurement. However, the position resolution is predominantly defined by the cell structure of the grid.

The stacks of grids are organised into modules and placed in aluminium 'vessels', filled with counting gas. The detectors are planned to be operated with a continuous

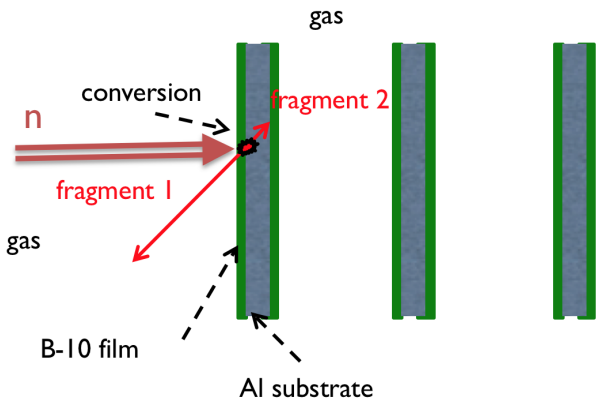

Figure 2.2: Neutron conversion with the multi-grid concept. The purple incident neutron beam is orthogonal to the grey aluminium blades, coated on both sides with enriched B_4C converter marked with green. The charged particles, produced in neutron conversion are shown in red as 'fragment1' and 'fragment2'.

gas flow of ca. 1 detector volume per day rate, with commonly available 1 bar 90/10–70/30 Ar/CO_2 gas mixture. The detector arc is built of these modules (see Figure 2.3). The read-out electronics are mounted on the outer side/top/bottom of each vessel.

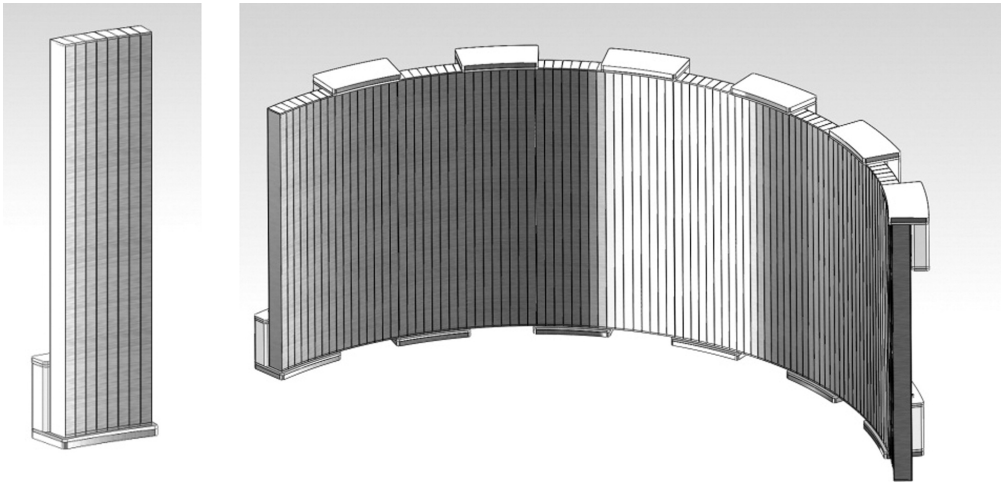

Figure 2.3: Early design of 8-column Multi-Grid module (left) with read-out electronics mounted on the bottom of the vessel, and a detector arc of 12 modules (right) with read-out electronics altering on the bottom and top of the modules. Plots are adopted from [14].

This novel Ar/CO_2-filled large area detector is the chosen solution for two of the planned chopper spectroscopes at ESS: CSPEC [21] and T-REX [29]. The detector development continuously goes on since 2009. Several demonstrators have been built and tested [30, 31], and the detector designs for CSPEC and T-REX are currently being optimised. A significant effort has been made to understand and reduce the background in the Multi-Grid and other boron converter based detectors. As a part

of this, the α-, γ- and fast neutron background components have already been studied and reduced, as described in [32], [33] and [34], respectively.

2.2 Argon activation in nuclear facilities

Experience over the last decades has shown that in facilities, e.g. nuclear power plants, research reactors and research facilities with accelerator tunnels, there is a permanent activity emission during normal operation that mainly contains airborne radionuclei [35–42]. For most of these facilities ^{41}Ar is one of the major contributors to the radiation release. ^{41}Ar is produced via thermal neutron capture from the naturally occurring ^{40}Ar, which is the main isotope of natural argon with 99.3% abundance [3]. ^{41}Ar is produced from the irradiation of the natural argon content of air. In air-cooled and water-cooled reactors ^{40}Ar is exposed in the reactor core as part of the coolant; in the latter case it is coming from the air dissolved in the primary cooling water. Air containing argon is also present in the narrow gap between the reactor vessel and the biological shielding. The produced ^{41}Ar mixes with the air of the reactor hall and is removed by the ventilation system. In other facilities ^{41}Ar is produced in the accelerator tunnel. In all cases, within the radiation safety plan of the facility the ^{41}Ar release is taken into account [43] and well estimated either via simple analytical calculations or Monte Carlo simulations. The average yearly ^{41}Ar release of these facilities can reach a few thousand GBq.

For the ESS the ^{41}Ar release coming from the accelerator and the spallation target is already calculated [44–46]. In addition, the exposure of the large volume of Ar/CO_2 contained in the neutron detectors should also be considered. Due to the 70–90% argon content of the counting gas and the fact that most instruments operate with thermal or cold neutron flux, that leads to a higher average reaction rate, the ^{41}Ar production in the detectors could be of concern. For all the above mentioned reasons, argon activation is an issue to consider at ESS both in terms of activity release and in terms of occupational exposure in the measurement hall.

With this, the principles of neutron detection and the novel, solid boron carbide converter based, Ar/CO_2-filled Multi-Grid detector are introduced, and the issue of Ar activation is highlighted. On this basis, the objectives of this thesis are described in the following chapter.

Chapter 3

Objectives

The ongoing construction of the ESS, the brightest neutron source of the world, the recent ^{3}He-crisis, and the continuous desire to exceed the state-of-the-art instrument performance are currently challenging the neutron detector development. The current thesis work takes part in this challenge in one of the widest fields of research: development of Ar/CO_2-filled proportional chambers with a solid boron-carbide converter, to meet the novel scientific requirements and to provide a cost effective alternative for ^{3}He-tubes. The latter is especially significant when large detector volumes are required, like for indirect geometry chopper spectrometers.

One of the main performance criteria of these spectrometers is typically defined by the Signal-to-Background Ratio (SBR); it is important to understand and enhance it with respect to instrument optimisation. Despite of this, currently the estimation of the SBR is mostly based on 'neutronic folklore'.

The utilisation of large area/large volume Ar/CO_2-filled detectors has so far been uncommon in high neutron irradiation fields. Therefore the large argon content, and the other new materials that appear with the new detector design, e.g. the massive aluminium content of the afore-described Multi-Grid detector contrary to the common stainless steel ^{3}He-tubes, raised the need for a novel, holistic approach in background estimation and design optimisation.

Therefore the aims of the current study are to take the first steps to fulfill this need, in particular in the mapping and understanding the background characteristics in Ar/CO_2-filled neutron detectors, with the recently developed Multi-Grid detector as a study case, and provide an effective, comprehensive method for background reduction via detector shielding optimisation.

3.1 Background sources

Radiation background is one of the key issues in any ionising radiation based experiment or facility, as it has impact in various fields. As for every application of ionising radiation, it has to be considered in terms of radiation safety, as it can be a source of occupational exposure, as well as in terms of nuclear waste management, due to the activation in various instrument components or shielding materials. However, the current study set the scope on background radiation in the measurement technique sense, i.e. regarding its impact on the experimental data. Neutron scattering instruments, especially if served by a spallation neutron source, also have to deal with a wide range of background radiation of various particles and energies, as listed in the following, in the spirit of the above interpretation:

- Environmental background: terrestrial and cosmic radiation background.
- Source and instrument background: fast neutron radiation (penetrating the monolith shielding, streaming down, leakage from nearby beam lines), prompt pulse, electromagnetic and hadronic showers (high energy photons, X-rays, bremsstrahlung, secondary neutron radiation, etc.), neutron-induced radiation in the experimental cave.
- Sample background: scattered neutron radiation from the bulk.
- Detector background: neutron-induced background, natural radiation background of detector component (e.g. α-emission from aluminium alloys [32]).

In order to improve the quality of the measurements via background suppression – taking into account cost, scientific and engineering requirements –, mapping and understanding the impact and these sources of the occurring complex radiation background is essential. The current study aims to explore and reduce the neutron-induced background produced in the new, large area Ar/CO_2-filled neutron detectors. Two main types of neutron-induced radiations are considered: gamma radiation from neutron activation, (both prompt- and decay-gamma), as well as elastic and inelastic neutron scattering in the components in and around of the detector (see Figure 3.1.)

3.2 Neutron-induced gamma radiation

Neutron activation occurs during the (n,γ) reaction where a neutron is captured by a target nucleus. The capture itself is usually followed by an instant photon emission;

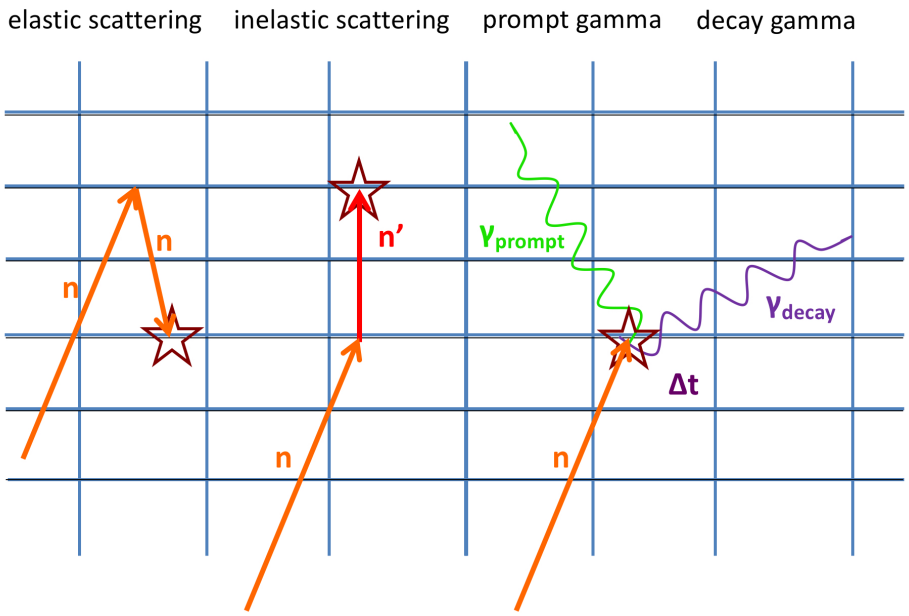

Figure 3.1: Sources of neutron-induced scattered and gamma background. The background products from an orange incident neutron (from left to right) are the followings: elastically scattered neutron in orange, inelastically scattered neutron in red, green prompt γ and purple decay γ from absorption.

these are the so-called 'prompt photons'. The energies of the emitted prompt photons are specific to the target nucleus. After capturing the neutron, in most cases the nucleus gets excited, and becomes radioactive; this is the process of neutron activation, and the new radionuclide suffers decay with its natural half-life. Due to their higher number of neutrons, the activated radionuclei mostly undergo β^- decay, accompanied by a well-measurable decay gamma radiation, where the gamma energies are specific to the radionucleus.

The neutron activation is a general concern for Ar/CO_2-filled neutron detectors due to the activation of the argon (see Section 2.2) and other uncommon solid materials. The aim of the current study is to determine the produced prompt- and decay-gamma radiation background in a generic Ar/CO_2-filled detector, as well as its impact on the SBR at various incident neutron energies. Also due to the generality of the problem, an additional aim is to provide easy-to-scale data on prompt- and decay-gamma yields, as input for 'back of the envelope' calculations for various irradiation setups.

As many of these detectors come with a large gas volume, the argon-activation can be an issue in terms of occupational hazard, nuclear waste production and activity emission as well. The activity production is also determined, as it should be of concern in detector development.

3.3 Scattering neutron background in detector

Neutron scattering can occur in any detector system, either on the solid components, e.g. housing, entry window, etc., or on the counting gas itself. If these elastically or inelastically scattered neutrons do not escape the detector, but get recorded, they lead to an 'intrinsic' scattered neutron background, specific to the detector. Consequently this background highly depends on the detector materials and may scale with its size.

In the current work the Multi-Grid detector (see Section 2.1.3) has been chosen as a subject of the scattered neutron background study. The reason for this is that on one hand these detectors are designed for chopper spectrometers, which are particularly background sensitive, as the measured inelastic signals are few orders-of-magnitude smaller than the commonly measured elastic ones. On the other hand, the large area Multi-Grid detector has a significant, $\sim$3 tonnes of aluminium content in a whole detector arc, due to the grid structure and the detector vessels. As the total neutron cross-section for aluminium is 1.7 barn [47] for thermal neutrons and increasing with $\frac{1}{v}$ for cold neutrons, where v is the velocity, the aluminium content has to be considered as a source of intrinsic background. An example of a scattered neutron is presented in Figure 3.2.

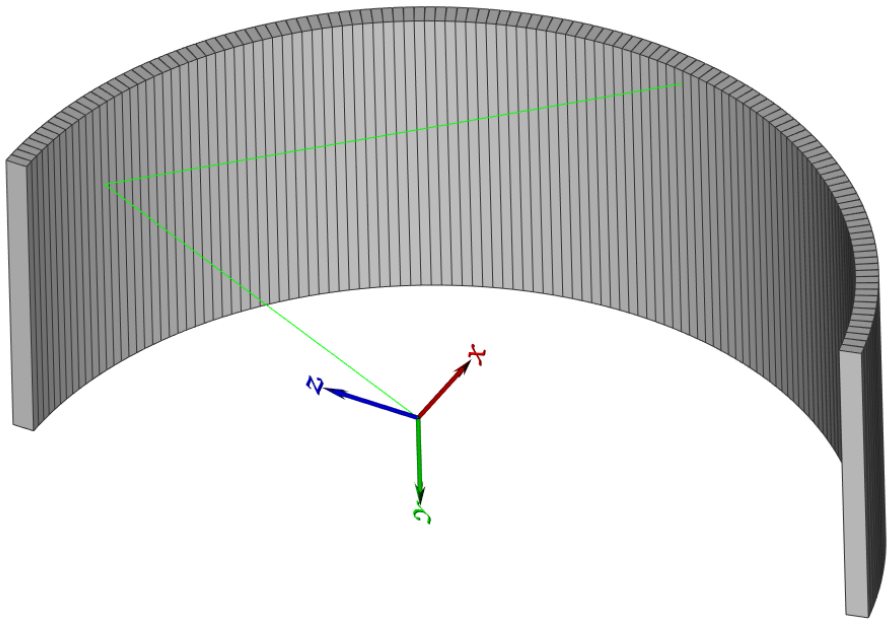

Figure 3.2: Single scattered neutron (green) in the Multi-Grid detector arc. Plot from Geant4 simulation.

In inelastic instruments the data of interest are the energy- and momentum transfer, derived from the measured Time-of-Flight (ToF) and the flight distance, calculated in-turn from the detection coordinates. A scattered neutron is either detected misplaced,

with a mismatch between the measured ToF and the assumed flight distance, leading to a false derived energy or can be detected with a change of real energy due to inelastic intrinsic scattering. Either way, if the shift in ToF, position or energy of a detected neutron exceeds the overall resolution of the experimental setup, that should be considered as a background event.

In the current thesis, different sources of the intrinsic scattered background are considered, e.g. neutron scattering on the aluminium grid structure and the counting gas, scattering on the detector vessel, and especially on the entry window, which is a well-known challenge of neutron detector development, as it is an important mechanical structure item, being part of the vacuum interface. In order to put the impact of these sources into perspective, they are also compared with some instrument-related background sources, such as the scattering on the sample environment and the tank gas of the measurement chamber. In the study elastic and inelastic scattering are simulated as well as interaction with crystalline materials (i.e. aluminium in this case), including both Bragg diffraction and inelastic/incoherent processes.

The aim of the current study is to *a)* develop and validate a detailed, parameterised and easy-to-scale, realistic Geant4 model of the Multi-Grid detector, *b)* use this model to distinguish and quantify the components of the intrinsic scattered neutron background from different sources and *c)* optimise the SBR in the Multi-Grid detector via background suppression with advanced shielding design.

3.4 Shielding materials and design

Shielding is one of the well-known issues of detector development, and neutron shielding itself has a long history both in terms of measurement and radiation safety. Therefore there is a set of neutron shielding materials that are commonly applied in detectors, based on their neutron absorption cross-section, price, availability and also their chemical and physical properties. Four of these materials, boron, cadmium, gadolinium and lithium are studied in the current work. All these materials have isotopes with high neutron absorption cross-section, i.e. ^{10}B, ^{113}Cd, ^{155}Gd, ^{157}Gd and ^{6}Li respectively, and have already been widely applied in neutron detectors or irradiation experiments in various chemical forms and carrier matrices for different purposes. However in many cases, especially for large area shielding, these materials are used with their natural isotopic composition, because of availability and cost considerations, and so is done in the current work. The cross-sections of the studied materials are presented in Figure 3.3.

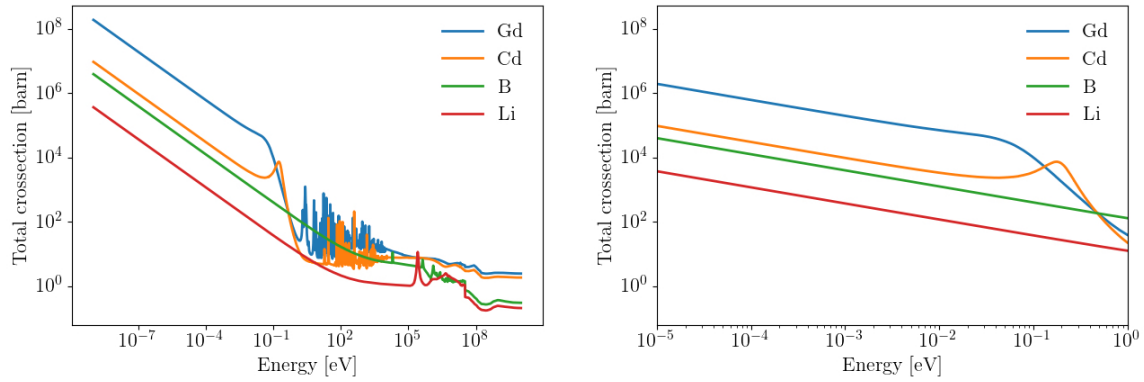

(a) (b)

Figure 3.3: Total cross-section of typical materials for neutron shielding with their natural isotopic composition. Data extracted from Geant4 for whole energy range (a) and for the typical operation range of chopper spectrometers at ESS (b).

In spite of their wide-spread utilisation, their application in a large area detector, such as the Multi-Grid is still challenging. Some of these materials are not used in elemental form, but within compounds, e.g. lithium is most commonly used as LiF, and boron is either used as 'boral', i.e. borated aluminium or as B_4C, as the latter is an industrial abrasive powder, and B_4C powder is therefore cheap and available in grand volume. Most of these materials cannot be placed in their pure chemical form, but have to be added to certain carrier matrices that also potentially alter the properties of the shielding.

Cadmium is one of the exceptions, as it is available as few mm thin pure Cd foil. However, as it is toxic, its application is dissuaded and mainly limited for smaller or closed areas. It is usually applied as shielding of the sample environment or in instrument components, e.g. slits, as it can provide very sharp edges. Nevertheless, due to its convenient structure and excellent absorption properties its application inside the detector vessel can be considered. Pure B_4C sheets can also be produced via sintering, but it is rather expensive, and only used for slits in some cases.

B_4C, LiF and Gd (the latter in the chemical compound Gd_2O_3) are most commonly used in powder form. From these, LiF is a more expensive shielding material, although it has some unique, beneficial properties. As ^{6}Li absorbs neutrons via the ^{6}Li(n,α)^{3}T reaction [48], without accompanying gamma emission, it is preferred in rather gamma-sensitive applications. B_4C, LiF and Gd_2O_3 powders are mixed into plastic, acrylic paint or even rubber. This way easy-to-apply, cost-effective shielding can be designed, like the MirroBor [49], which is a very convenient large area shielding material, pro-

duced by Mirrotron [50] in 2–5 mm thick rubber-like, flexible sheets with 80% B_4C content. These sheets are easy to cut and also to attach, as one of their sides can be self-adhesive. However, these carrier materials have other concerns; on one hand, they can be a source of thermal neutron scattering due to their high hydrogen-content. On the other hand, the aging of these materials can also be an issue: they may crumble and therefore contaminate the counting gas. Due to this the usage of many common shielding solutions is limited within the detector, e.g. friable materials are not used in sealed detectors, and also mostly avoided in the ones operated in flush-mode, or matrices with high hydrogen-content are not encouraged to be applied in large areas.

Having considered all these issues and benefits, the aim of the current study is to *a)* evaluate the background-reducing potential of internal shielding in the Multi-Grid detector, *b)* determine the impact of these shielding materials in the detector and *c)* provide input and perform the first steps towards background suppression via combined shielding design. For these purposes the afore-introduced shielding materials are simulated in various areas in the Multi-Grid detector, in their representative chemical compound. As of the complexity of the problem, in the current thesis the first steps are performed, and therefore the simulations are performed without carrier matrices, except of one case of demonstration. This is the first introduction and application of a novel, holistic approach in detector optimisation, based on complex and advanced Monte Carlo simulations.

In the following, the tools for the performed studies are introduced: two Monte Carlo simulation codes, MCNP, used for gamma background and activation study, and Geant4, used for the scattered neutron background study and shielding optimisation (Chapter 4). For the gamma background and activation study analytical calculations are also performed, and the theory and the used databases are presented in Chapter 5. Then the respective implemented detector models are described in Chapter 6.

Part II

Methodology

Chapter 4

Simulation techniques and their evaluation

The Monte Carlo particle transport has been a valued tool of nuclear and particle physics for decades and its history dates back to the 1940s [51]. The basic concept of the method is to determine the behaviour of the particles in a physical system from the average behaviour of a manifold of individually simulated particles in a certain point of the phase space, according to the Central Limit Theorem. The particle transport through the studied system is performed with the use of the random sampling technique. In a simple Monte Carlo game a particle *a)* is generated by sampling from a well-defined initial distribution of the source term: (E,$\mathbf{r}$,$\mathbf{\Omega}$), i.e. energy, space vector and direction respectively, *b)* is transported by sampling the mean free path and *c)* interacts with the material by sampling the respective reaction cross-sections [52]. Here the particle can collide and continue or get absorbed with or without generating secondary particles. An example for a particle history in Monte Carlo (E',$\mathbf{r}$',$\mathbf{\Omega}$') simulation in a finite parallelepiped volume is presented in Figure 4.1.

In the current thesis two highly advanced Monte Carlo codes are used, i.e. MCNP6 and Geant4. Both codes rely on extensive validated databases and models for particle interactions and treat a great selection of particles in a wide energy range. They both have the features of modern Monte Carlo programs, e.g. multi-threading, visualisation. Due to their original purpose and conditions, they have been developed with different approach and mentality, leading to tools interchangeable only with difficulty. However, they now can be easily combined with the recently developed MCPL (Monte Carlo Particle List) open source code [53–55].

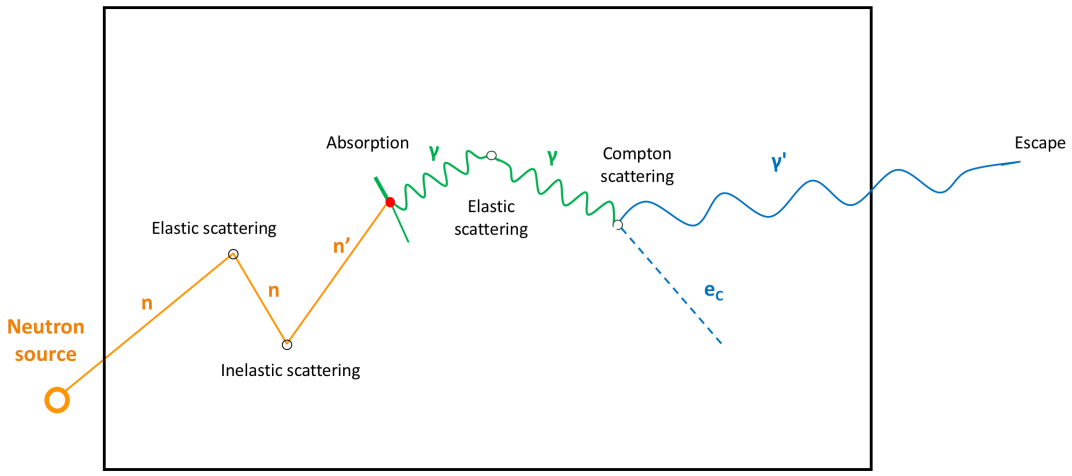

Figure 4.1: Particle history in a Monte Carlo transport simulation. The surrounding rectangle represents a finite simulated volume. An orange incident neutron suffers elastic and then inelastic scattering, and finally gets absorbed. Two green conversion particles are emitted after the absorption, in addition to a green gamma, which undergoes an elastic and a Compton-scattering, producing a Compton-electron and an escaping scattered photon, both in blue.

4.1 MCNP

MCNP (Monte Carlo N-Particle) is a Fortran-based Monte Carlo code, developed at the Los Alamos National Laboratories. The code is export-controlled by the US Government and therefore its distribution is limited. MCNP originates from the MCN neutron transport code, one of the first general-purpose Monte Carlo particle transport codes (1965). After being merged with MCG and MCP gamma and photon transport codes the MCNP was born in 1977. The code was developed with the main purpose of neutron transport, shielding and criticality calculations, but kept being extended and developed ever since. Presently it is applicable in various fields, e.g. radiation protection and dosimetry, radiation shielding, radiography, medical physics, nuclear criticality safety, accelerator target design, fission and fusion reactor design, decontamination and decommissioning, etc.

MCNP6.1 is one of the latest versions of the code, rewritten in ANSI standard Fortran 90. Neutrons are treated from 10^{-11} MeV to 20 MeV for all isotopes, and for some of them up to 150 MeV, while the photons are treated from 1 keV to 100 GeV. The neutron transport is driven mainly by point-wise cross-section data from associated nuclear and atomic data libraries, such as the commonly used ENDF/B-VII [47]. These databases also contain other reaction-related data like angular distribution after scattering, production of secondary particles, etc. For neutron interaction, there are four database types used by MCNP: continuous-energy and discrete reaction interac-

tion data, neutron dosimetry cross-sections and the compact S(α,β) scattering data (where momentum and energy transfer data are stored in a compact form in α and β respectively) for thermal neutrons, treating elastic and inelastic scattering below 2 eV.

In accordance to its main features and reliability, MCNP is the flagship among Monte Carlo codes in radiation protection, accepted by most authorities and also at ESS this code is required to be primarily used for source term, shielding and dosimetrical simulations [56]. In the current work MCNP6.1 is chosen to study activation and neutron-induced gamma background, as this task has relevance in radiation protection (i.e. occupational exposure), as well as nuclear waste management.

4.2 Geant4

Geant4 [57–59] is an open-source, freely available, object-oriented simulation toolkit written in C++, developed by CERN's RD44 collaboration (1994–2006). The code originates from GEANT3 (GEometry ANd Tracking), a FORTRAN-based code also developed at CERN for high energy physics experiments (1982). The Geant4 toolkit was developed with the main focus on detector simulations. The toolkit can handle the fundamental particles of high energy physics in a wide energy range, e.g. hadrons from thermal region up to 1 PeV, and processes like decay, neutron- and proton-induced isotope production, photonuclear reactions, ionisation, etc. It also provides several features motivated by detection processes, like external electromagnetic fields or optical processes (Cherenkov radiation and scintillation).

Geant4 uses data-, theory- or parameterisation-based models, e.g. the neutron transport up to 20 MeV, or 150 MeV in the case of isotopes is performed by data-driven simulation, relying on the same or similar databases as MCNP. In Geant4 the particles, models and cross-section data used for a specific simulation are in the so-called 'physics list' class, offering maximal flexibility for customisation by the user. In addition, several pre-defined, validated 'reference' physics lists are provided as ready-to-use plug-ins. The toolkit also offers very flexible analysis based on histogram-filling. Due to its modular structure and opensourceness, the toolkit is continuously developed and extended, and therefore being applied in various fields, e.g. particle physics, nuclear physics, accelerator design, space engineering, medical physics and radiobiology.

In the current work Geant4 is interfaced with the afore-introduced MCPL tool, as well as with two recently developed libraries, NXSG4 [60, 61] and NCrystal [62, 63], that allow to model thermal neutron interactions with crystalline materials, including both Bragg diffraction and inelastic/incoherent processes. The simulations are performed

within the ESS Coding Framework [64], developed by the ESS Detector Group, where all the new tools are available in an integrated and ready-to-use way, among other features like easy and compact analysis and advanced visualisation.

These simulation tools facilitated the detailed exploration of the neutron-induced detector background, and its impact on the measured signal. However, for the neutron activation study, the MCNP simulations are compared with analytical calculations as well, as subsequently described in Chapter 5.

Chapter 5

Analytical calculation for neutron activation

Neutron activation is a well-known phenomenon, which has long been taken into account in the field of radiation protection and nuclear waste management, and also gives the basics of long-used and reliable analytical techniques, the neutron activation analysis (NAA [65–67]) and the prompt gamma activation analysis (PGAA [68]). Consequently, detailed measured and simulated data, and simple but reliable analytical methods are available for neutron activation calculations. Due to this, these calculations can also be used as reference for the development and implementation of Monte Carlo models for similar calculations, as it is performed in the current work (see Chapter 7)

In the present thesis, neutron activation is studied in the counting gas and solid aluminium housing of Ar/CO_2-filled neutron detectors under typical ESS operational conditions. The purpose of the analytical calculation is to corroborate the developed MCNP model and material setup in a simple configuration, thus allowing their use in more complex geometries.

For shielding and radiation safety purposes the produced activity concentration (a [Bq/cm^3]) and the prompt photon intensity have to be calculated from the number of activated nuclei (N^* [1/cm^3]). The production of radionuclides (*reaction rate*) depends on the number of target nuclei (N_0 [1/cm^3]) for each relevant isotope, the irradiating neutron flux (Φ [n/cm^3/s]) and the (n,γ) reaction cross-section (σ [cm^2]) at the irradiating neutron energies, while the loss of radionuclides is determined by their decay constants (λ [1/s]). A basic assumption is that the number of target nuclei can be treated as constant if the loss of target nuclei during the whole irradiation does not exceed 0.1%. This condition is generally fulfilled, like in the cases examined in

this study, therefore the rate of change of the number of activated nuclei is given by Equation 5.1.

$$\frac{dN^*}{dt} = N_0 \cdot \Phi \cdot \sigma - \lambda \cdot N^* \tag{5.1}$$

With the same conditions, the activity concentration a after a certain irradiation time t_{irr} [s] can be calculated with Equation 5.2.

$$a\left(t_{irr}\right) = N_0 \cdot \Phi \cdot \sigma \cdot \left(1 - e^{\lambda t_{irr}}\right) \tag{5.2}$$

As the activation calculation is based on Equation 5.2, the activation of the naturally present radionuclides (e.g. cosmogenic ^{14}C in CO_2) is ignored in this study due to the very low abundance of these nuclides. The activity yield of the secondary activation products, the products of multiple independent neutron captures on the same target nucleus, are ignored as well, because of the low probability of the multiple interaction.

The prompt gamma intensity (I [1/s/cm^3]) coming from the neutron capture can be calculated similarly to the (n,γ) reaction rate. In this case a prompt gamma-line (i) specific cross-section ($\sigma_{pg,i}$) has to be used [69], which is proportional to the (n,γ) cross-section, the natural abundance of the target isotope in the target element, and the weight of the specific gamma energy with respect to the total number of gamma lines. For this reason in Equation 5.3 the number of target nuclei corresponds to the element (N_0' [1/cm^3]), not the isotope (N_0 [1/cm^3]).

$$I_i = N_0' \cdot \Phi \cdot \sigma_{pg,i} \tag{5.3}$$

In this study, activity concentration, prompt gamma intensity and the respective prompt gamma spectrum are calculated for each isotope in the natural composition [3] of an 80/20 volume ratio of Ar/CO_2 counting gas at room temperature and 1 bar pressure and in an aluminium alloy used for the detector frame. Alloy Al5754 [70] is chosen as a typical alloy used in nuclear science for mechanical structures. Activity concentration and prompt gamma intensity calculations have been performed for several mono-energetic neutron beams in the range of 0.6–10 Å (227.23–0.82 meV). Since for isotopes of interest the energy dependence of the (n,γ) cross-section is in the $\frac{1}{v}$ region [47, 71], the cross-sections for each relevant energy are easily extrapolated from the thermal (1.8 Å) neutron capture cross-sections listed in Table A1.

For all analytical calculations the Gaussian Error Propagation Law is applied, taking into account the uncertainty of the prompt gamma line specific cross-section, given in the IAEA PGAA Database [69], being below 5% for the main lines of all major isotopes, the σ absorption cross-section and the λ decay constant (see Appendix).

The irradiating neutron flux has been approximated with 10^4 n/cm^2/s. This value has been determined for a chopper spectrometer, for a worst case scenario based on the following assumptions (see Figure 5.1): the planned instruments are going to have various neutron fluxes at the sample position and the highest occurring flux can be conservatively estimated to 10^{10} n/cm^2/s [12]. The neutron fraction scattered from the sample is in the range of 1–10%. Calculating with 10%, the approximation remains conservative. A realistic sample surface is 1 cm^2, reducing the scattered flux to 10^9 n/s. The sample-detector distance also varies among the instruments, so the smallest realistic distance of 100 cm was used for a conservative approximation. Therefore, the neutron yield has to be normalised to a 10^5 cm^2 surface area at this sample-detector distance. According to these calculations, 10^4 n/cm^2/s is a conservative estimation for the neutron flux the detector is exposed to. This simple approach allows the result to be scaled to alternate input conditions, i.e. a higher neutron flux or different detector geometry, providing input for fast, simple and conservative 'back-of-the-envelope' calculations for various instruments, equipped with Ar/CO_2-filled detectors. These calculated results on prompt- and decay-gamma spectra and neutron-induced activity also serve as reference for MCNP simulations, as introduced in the followings, in Section 6.1.

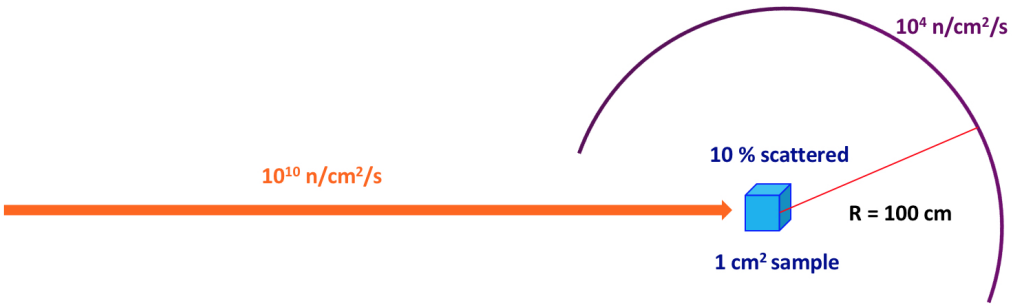

Figure 5.1: General layout of neutron scattering instrument with large area detector. Conservative flux-estimation for analytical activation calculation. Incident neutron beam is indicated in orange, targeted to a blue sample. The schematic detector arch is presented in purple.

Chapter 6

Implemented detector models

6.1 General Ar/CO_2 detector model in MCNP6.1

The argon activation is a well-known issue for nuclear facilities, and may be concerned Ar/CO_2-filled detectors as well, as introduced in Section 2.2. Analytical calculations based on extensive databases are applicable to determine the neutron-induced activity and gamma-background production, as described in the previous chapter (see Chapter 5), although they may be cumbersome to apply for complex geometries or for fast, but conservative estimations. For this reason, Monte Carlo simulations have also been performed, and compared with analytical calculations, in order to determine the expected activity concentration and prompt gamma intensity in the counting gas and the aluminium frame of boron-carbide-based neutron detectors, in a simple, generic Ar/CO_2-filled detector volume, that is easy-to-scale for further irradiation scenarios.

The MCNP6.1 [72] version has been used for the simulations. The detector gas volume has been approximated as a generic 10 cm $\times$ 10 cm $\times$ 10 cm cube, surrounded by a 5 mm thick aluminium box made of Al5754 alloy, representing the detector frame, as it is described in Figure 6.1. In order to avoid interference with the prompt photon emission of the Ar/CO_2, the counting gas was replaced with vacuum while calculating the activation on the aluminium frame. The detector geometry has been irradiated with a mono-energetic neutron beam from a mono-directional disk source of 8.5 cm radius at 50 cm distance from the surface of the target volume. A virtual sphere has been defined around the target gas volume with a 10 cm radius for simplifying prompt photon counting. Both the activity concentration and the prompt gamma intensity determined with MCNP6.1 simulations have been scaled to a 10^4 n/cm^2/s irradiating neutron flux.

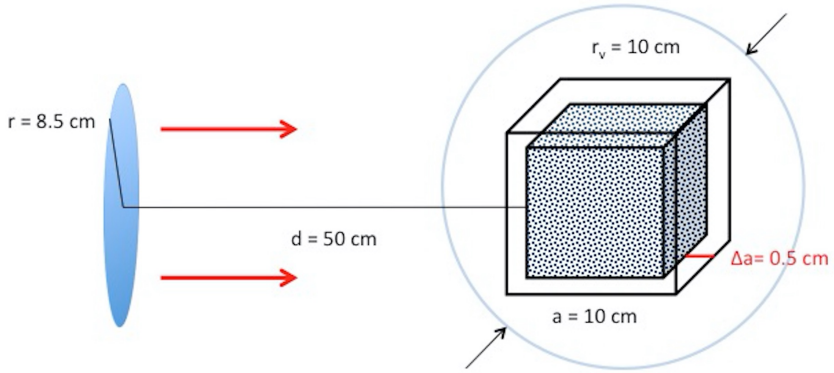

Figure 6.1: Neutron irradiation geometry used in MCNP6 simulation. A gas cube with 10 cm edge length, surrounded with 5 mm aluminium is placed in a virtual sphere, and irradiated with a mono-energetic neutron beam from a mono-directional disk source of 8.5 cm radius.

Different runs have been dedicated for each element in the gas mixture and the Al5754 alloy to determine the prompt gamma spectrum and total intensity. The prompt photon spectrum has been determined for each element with the following method: a virtual sphere has been defined around the cubic target volume. Since the target volume is located in vacuum, all the prompt photons produced in a neutron activation reaction have to cross this virtual surface. Within MCNP, the particle current integrated over a surface can be easily determined (F1 tally [72]). Knowing the volume of the target, the prompt photon intensity can be calculated for the simulated neutron flux (Φ_{MCNP}, [flux/source particle]). After the Φ_{MCNP} average neutron flux in the target volume has been determined (F4 tally [72]), the prompt photon intensity can be scaled for any desired neutron flux, 10^4 n/cm^2/s in this case. With this method the self-absorption of the target gas volume can be considered to be negligible.

The activity concentration of the generated radionuclides is not given directly by the simulation, but can be calculated from the R_{MCNP} reaction rate (reaction/source particle) and the Φ_{MCNP} flux. The R_{MCNP} is calculated in MCNP in the following way: first the track length density of neutrons has to be determined in the target volume (F4 tally [72]), and then this value has to be multiplied with the reaction cross-section of the specific reaction of interest, through the entire spectrum, taking into account the number of target nuclei of the irradiated material (FM tally multiplication card [72]). In the current simulations each isotope has been defined as a different material, with their real partial atomic density ([atom/barn/cm]) in the counting gas or in the aluminium alloy for the (n,γ) reaction (ENDF reaction 102). As the reaction rate given by the MCNP simulation is the saturated reaction rate for the Φ_{MCNP} flux, and contains all

the geometrical and material conditions of the irradiation, the time-dependent activity concentration for any Φ flux can be calculated with Equation 6.1:

$$a\left(t_{irr}\right) = R_{MCNP} \cdot \frac{\Phi}{\Phi_{MCNP}} \cdot \left(1 - e^{\lambda t_{irr}}\right). \tag{6.1}$$

In order to determine the above mentioned quantities, the cross-section libraries have to be chosen carefully for the simulation. Within the current study different libraries have been used to simulate the prompt gamma production and the reaction rates. Several databases have been tested, but only a few of them contain data on photon production for the isotopes of interest. Tables A2 and A4 present the combinations that give the best agreement with the theoretical expectations, especially in terms of spectral distribution. These are the ENDF [47], TALYS [73] and LANL [74] databases.

The MCNP6.1 simulation has been repeated for each isotope in the counting gas and the aluminium frame, and analytical calculations have also been performed to validate the simulation, in order to obtain reliable and well-applicable data on the detector housing and counting gas activation and gamma emission both for shielding and for radiation protection purposes.

In order to demonstrate the effect of gamma radiation on the measured neutron signal, the 'Neutron-to-Gamma Response Ratio' (NGR) has been calculated for a typical and realistic detector geometry. A generic boron-carbide based detector can be represented by a 5–20 mm thick gas volume surrounded by a few millimetre thin aluminium box, carrying the few micrometres thick boron-carbide converter layer(s). The gas volume is determined by the typical distance needed for the energy deposition. In a realistic application, a larger gas volume used to be used for efficiency purposes, built up from the above mentioned subvolumes. As a representative example a $V_{gas} = 256$ cm^3 counting gas volume has been chosen as the source of gamma production, with an $A_{in} = 16$ cm^2 entrance surface area for incident neutrons, divided into 20 mm thick subvolumes by 16 layers of 2 μm thin enriched boron-carbide.

In this study the gamma efficiency has been approximated with 10^{-7} for the entire gamma energy range [30, 33] due to its relatively low energy-dependence, whereas the neutron efficiency has been calculated for all the mentioned energies on the basis of [14], resulting in a neutron efficiency varying between 0.4–0.72 within the given energy range. Therefore the measured neutron response and the response for the gamma background were calculated as in Equations 6.2-6.3, where η_i is the detection efficiency for the particle type i, Φ is the incident neutron flux and I_{photon} is the photon production rate

in a unit gas volume. The Neutron-to-Gamma Response Ratio has been calculated as $S_n/S\gamma$, where

$$S_n = A_{in} \cdot \Phi \cdot \eta_n, \tag{6.2}$$

$$S_\gamma = V_{gas} \cdot I_{photon} \cdot \eta_\gamma. \tag{6.3}$$

All calculations and simulations have been done for a 10^4 n/cm^2/s mono-energetic neutron irradiation for 227.2, 81.8, 25.3, 20.4, 5.1, 3.3 and 0.8 meV incident neutron energies (i.e. for wavelengths of 0.6, 1, 1.8, 2, 4, 5 and 10 Å respectively). Activity concentration has been calculated for $t_{irr} = 10^6$ s irradiation time and $t_{cool} = 10^7$ s cooling time. This irradiation time roughly corresponds to typical lengths of operation cycles for spallation facilities. Photon production has been normalised for a 1 cm^3 volume, irradiated with $\Phi = 1$ n/cm^2/s or $\Phi = 10^4$ n/cm^2/s neutron flux. Therefore, here the photon production in a unit gas or aluminium volume irradiated with a unit flux is given as $\frac{\text{photon/cm}^3\text{/s}}{\text{n/cm}^2\text{/s}}$.

This way the produced results provide a conservative estimation for the activity and gamma radiation background production in the counting gas and other detector components for standard operation conditions the ESS chopper spectrometers. The obtained results are presented and discussed in Chapter 7.

6.2 Multi-Grid detector simulation in Geant4

The Multi-Grid is a recently invented [25, 26] gaseous detector, which is the chosen technology for the two chopper spectrometers of the ESS. The detector is currently being jointly developed by ILL and ESS, to which process this current study contributes. For this reason, the Geant4 model of the detector was implemented in a flexible and well-parameterised way, so it could be easily tailored to the various demonstrators and the meanwhile developed design of the planned ESS detectors.

The Monte Carlo model of the detector was implemented in the afore-introduced Geant4 [58, 59, 75] with the usage of the ESS Coding Framework [76] (See 4.2.) As a first step, a detailed, realistic Multi-Grid model was implemented with the 2015 geometrical design of the detector, considering the potential changes.

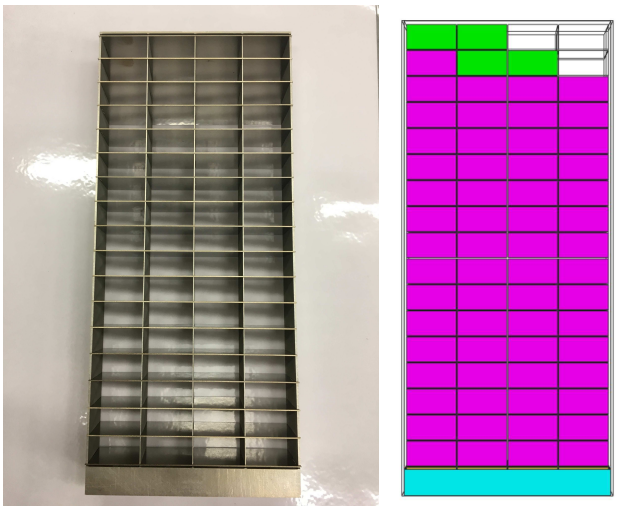

(a) (b)

Figure 6.2: Real grid (a) and grid geometry implemented in Geant4 (b), where the counting gas is shown in green, the rear aluminium blade in cyan, and the shielding appears in brown.

The basic unit of the model is the aluminium grid, whose columns and modules are built in the same way as it is described in Section 2.1.3. The anode wires and the electronics of the detector are excluded from the model, as it is shown in Figure 6.2, where real and implemented grids are compared. In order to increase flexibility, the undecided geometrical parameters, both in the grid (e.g. the size and number of cells in the grid, the thickness of the aluminum blades and the B_4C converter layers) and the parameters of the modules (e.g. number of grids and stacks, or the vessel design) are added as input variables, and the metrics of the complex model is derived from these. The major input parameters of the model are presented in Table 6.1. Examples for the construction of a detector arc from grids are depicted in Figure 6.3, in an idealistic

single column (a and b) design, and an early state, realistic 5-column module (c and d) design, fulfilling engineering requirements.

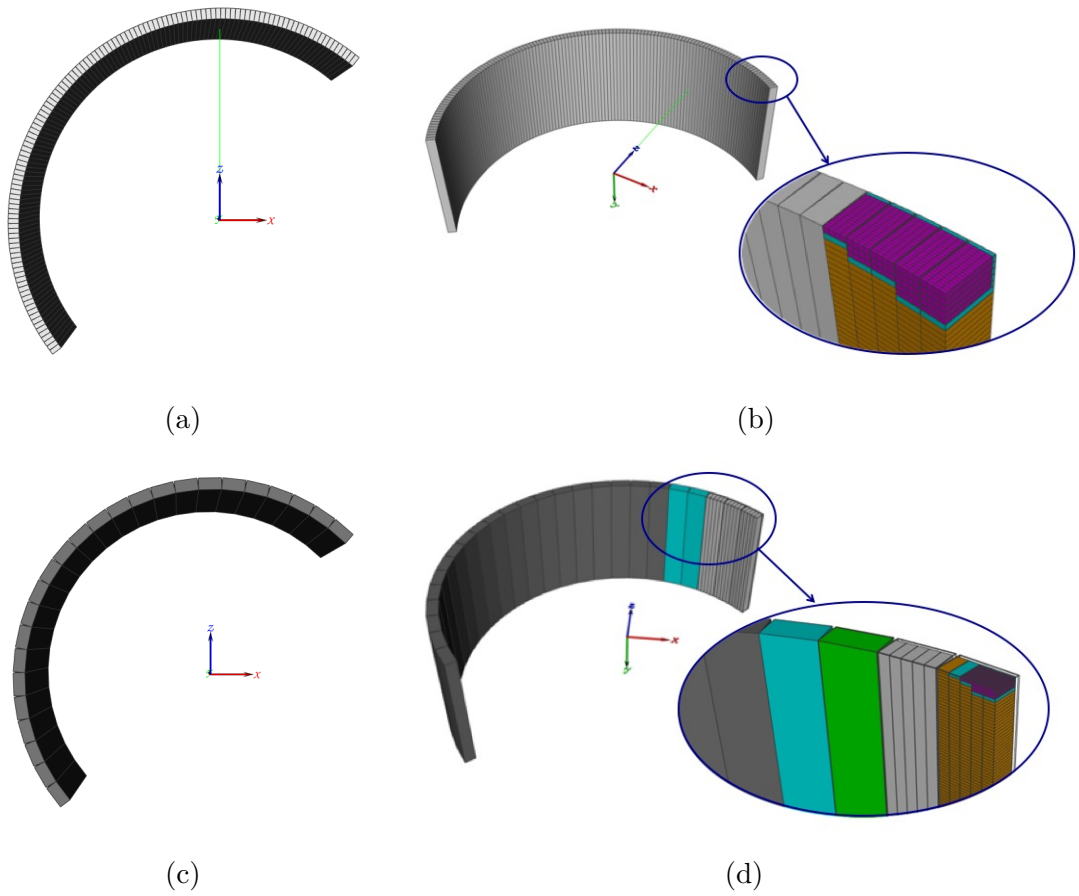

(a) (b)

(c) (d)

Figure 6.3: Implemented general Geant4 model of Multi-Grid detector arc in an idealistic single column (a and b) design, and an early state, realistic 5-column module (c and d) design.

Table 6.1: Major default geometrical parameters of Multi-Grid detector models.

Parameter		Default value			
		Basic model	IN6 model	CNCS model	CSPEC model
Number of cells	width (x)	4	4	4	6
	depth (z)	17	17	17	16
Number of grids in stacks		127	16	48	140
Number of stacks		125[1]	6	2	2
Cell size	width (x)	2.2 cm	2.2 cm	2.2 cm	2.5 cm
	height (y)	2.26 cm	2.26 cm	2.25 cm	2.4 cm
	depth (z)	1.1 cm	1.1 cm	1.1 cm	0.95 cm
Coating thickness	short blade[2] (parallel with window)	1.0 μm	1.0 μm	0.5–1.5 μm	0.5–1.5 μm
	long blade[3] (orthogonal to window)	-	-	-	1.0 μm
Frame entrance thickness		1.0 mm	1.0 mm	2.0 mm	0.5 mm
Frame end thickness		11.6 mm	11.6 mm	12.5 mm	10.0 mm
Frame side thickness		1.0 mm	1.0 mm	1.0 mm	0.5 mm
Blade thickness	short blade	0.6 mm	0.6 mm	0.5 mm	0.5 mm
	long blade	0.5 mm	0.5 mm	0.5 mm	0.5 mm
End-shielding thickness		1.0 mm	10^{-7} mm[2]	1 mm	1.0 mm
Side-shielding thickness		1.0 mm	0 mm	0 mm	1.0 mm
Interstack-shielding thickness		1.0 mm	1.0 mm	1.0 mm	2.0 mm
Intergrid gap		1.0 mm	1.0 mm	1.0 mm	1.0 mm
Interstack gap		1.0 mm	1.0 mm	1.0 mm	6.0 mm
Sample-detector front face distance		4 m	2.48 m	3.33 m	
Modules		no	no	yes	yes
Vessel		-	-	yes	yes
Vessel window thickness		-	-	3.0 mm	4.0 mm
Vessel sidewall thickness		-	-	3.0 mm	4.0 mm
Vessel backwall thickness		-	-	10.0 mm	4.0 mm
Physics list		QGSP_BIC_HP		ESS_QGSP_BIC_HP_TS[3]	
Counting gas		Ar/CO_2	Ar/CO_2	Ar/CO_2	Ar/CO_2
		80/20	90/10	80/20	80/20
Coating		$^{10}B_4C$	$^{10}B_4C$	$^{10}B_4C$	$^{10}B_4C$
				97 % enriched	
Vessel material		-	-	Al[4]	Al[4]
Frame material		Al[5]	Al[5]	Al[4]	Al[4]
PCB material		-	-	-	Al[4], polyethylene
End-shielding		PE/Gd_2O_3	-	PE/Gd_2O_3	PE/Gd_2O_3
		50/50	-	33/67	50/50
Side-shielding		-	-	MirroBor [49]	-
Interstack-shielding		MirroBor	-	MirroBor	-

[1]Number of columns defined to build a typical 180° detector arch.

[2]End shielding is implemented as a volume of PE+Gd_2O_3, therefore 0 mm thickness is not allowed by the code. Lack of shielding was obtained with the minimum applicable thickness.

[3]Customised physics list for the thermal scattering on materials with high hydrogen-content, e.g. polyethylene [77].

[4]Crystalline aluminium enabled with NCrystal.

[5]Crystalline aluminium enabled with NXSG4.

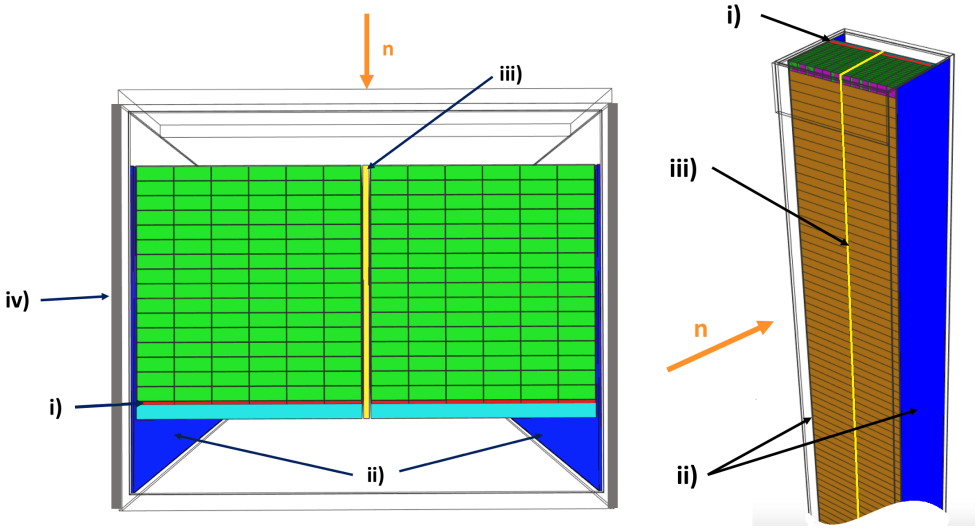

(a) (b)

Figure 6.4: Shielding elements in Multi-Grid detector module geometry. Top view (a) and side view (b) with the studied shielding topologies marked with: red for *i)* 'End-shielding', blue for *ii)* 'Side-shielding', yellow for *iii)* 'Interstack-shielding' and grey for *iv)* 'External vessel-shielding'. (Only marked in a for better visibility.) Counting gas is shown in green, the grid is brown with cyan rear blade, and the incident neutron beam is indicated in orange.

The detector model involves pre-defined volumes for shielding materials (see Table 6.1) in the most common places of the detector, as they are listed here and shown for a two-column module in Figure 6.4.

- 'End-shielding': Layers of shielding (see Figure 6.4, *i)*, red) applied in each grid, placed between the last row of cells (green) and the 1 cm thick aluminium rear blade (cyan) of the grid, to prevent backscattering from the latter. The surface area of the shielding meets the dimensions of the cell.

- 'Side-shielding': Layers of shielding (see Figure 6.4, *ii)*, blue) applied on the inner side of the vessel wall (see Figure 6.4b, transparent).

- 'Interstack-shielding': A sheet of shielding (see Figure 6.4, *iii)*, yellow) placed between the two columns of grids (see Figure 6.4b, brown), to prevent cross-talk. The shielding surface area meets the dimensions of the columns, and the maximum feasible thickness is the width of the gap between the columns.

- 'External vessel-shielding': Layers of shielding (see Figure 6.4, *iv)*, grey) applied on the outer side of the vessel wall to prevent cross-talk between the modules. The shielding surface area is defined by the size of the vessel wall.

In the simulations the primary neutrons are generated at the sample position. The sample is placed at the centre of the geometry, with the 'z' direction chosen as the beam direction, leading to 'x' as horizontal and to 'y' as vertical coordinates. The sample-to-detector distance is defined as the shortest distance from the sample position to the entrance window of the detector: grid window or vessel window, in case the latter is enabled. Common particle guns, like a pencil or conical beam, 4π and cylindrical sources are used, as well as targeted beams to irradiate only the detector surface. Although the physics of the samples themselves is not implemented in the simulations, the above listed particle guns are defined both as point and volume sources ($1 \times 1 \times 1$ cm^3 cube or cylinder with 1 cm diameter). Some instrument effects are introduced via the source definition, like the energy distribution of the incident primary neutrons. An example of the full-scale detector arch irradiated with cone beam is presented in Figure 6.5.

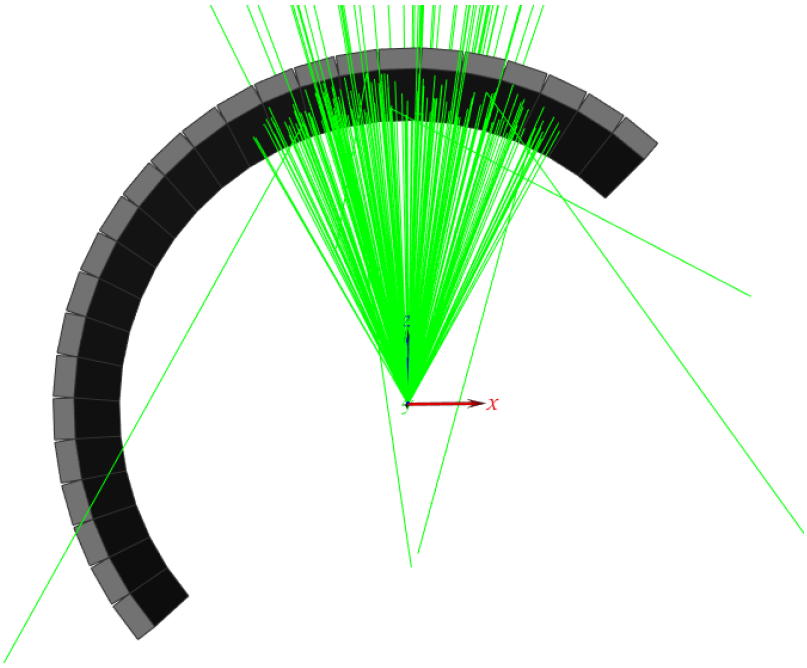

Figure 6.5: Geometry view of full-scale Geant4 detector model in grey, irradiated with a conical beam from sample position. Neutron tracks appear in green.

All materials in the model are implemented as compositions of standard Geant4 materials except aluminium; its poly-crystalline structure is interpreted with the help of the NXSG4 [61], and the NCrystal [63] library as the latter has been developed in parallel with the current study. The physics list is the standard QGSP_BIC_HP, except when material with high hydrogen-content, e.g. polyethylene is included, in which case a customised physics list is preferred instead [53], due to the relevance of thermal scattering on the hydrogen.

The Multi-Grid detector is designed for chopper spectroscopy, where the data of interest are the energy- and momentum-transfer, derived from the measured ToF and the flight distance, calculated in-turn from the detection coordinates. Likewise to real measurements, these parameters are accessible in the simulation as well. In Geant4 the realistic neutron detection is simulated via the detection of charged particles (α and Li) coming from the conversion; this detected event is called a hit, and is accompanied by all realistic physical properties, like detection coordinates, ToF, measured from start of primary neutron source until hit, etc. as it is demonstrated in a two-column detector module simulation in Figures 6.6.

In Figure 6.6a the ToF is measured from the sample position to detection point. A small background shoulder is present before 3.6 ms, containing the neutrons that gained energy in inelastic scattering, appearing with higher velocity in the spectrum. The long, falling tail after the peak consists of the elastically scattered neutrons and the ones with energy loss from inelastic scattering, appearing with lower velocity in the spectra. The broadening of the ToF peak corresponds to the height of the detector module, while the tiny peaks, that clearly appear at the beginning, but are smeared over through the whole peak, reflect the parallel conversion layers within the depth of the detector.

As it is shown in Figure 6.6b, the implemented grid geometry is clearly visible in the hit coordinates: two separate grids with 6 cells in each, and a 6 mm gap between them. The deep and sharp valleys between the cells are attributed to the absorption in the 0.5 mm thick long blades. The impact of the long blade coating on the distribution also appears as detection peaks and shadowed valleys on the inner and outer side of the long blades, respectively.

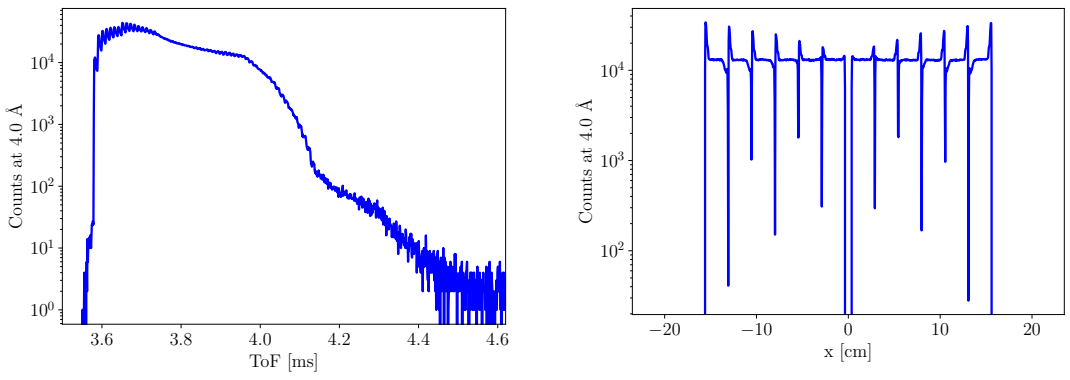

(a) (b)

Figure 6.6: ToF spectrum (a) and position of detected neutrons across the width of the detector (b) at 5.1 meV initial neutron energy (4 Å).

However, the position resolution provided in the simulation is much finer than what can be obtained in real measurements. In order to have a better approximation of the measured quantities, the hit position can be replaced by the the position of the anode wires in the post-processing of the analysis, as it is demonstrated in Figure 6.7. In Figure 6.7b the hits appear in the close proximity of the converter layers, not filling the whole cell volume. The different penetration depth of the α particle and Li ion can also be identified in the band structure of the clouds of hits.

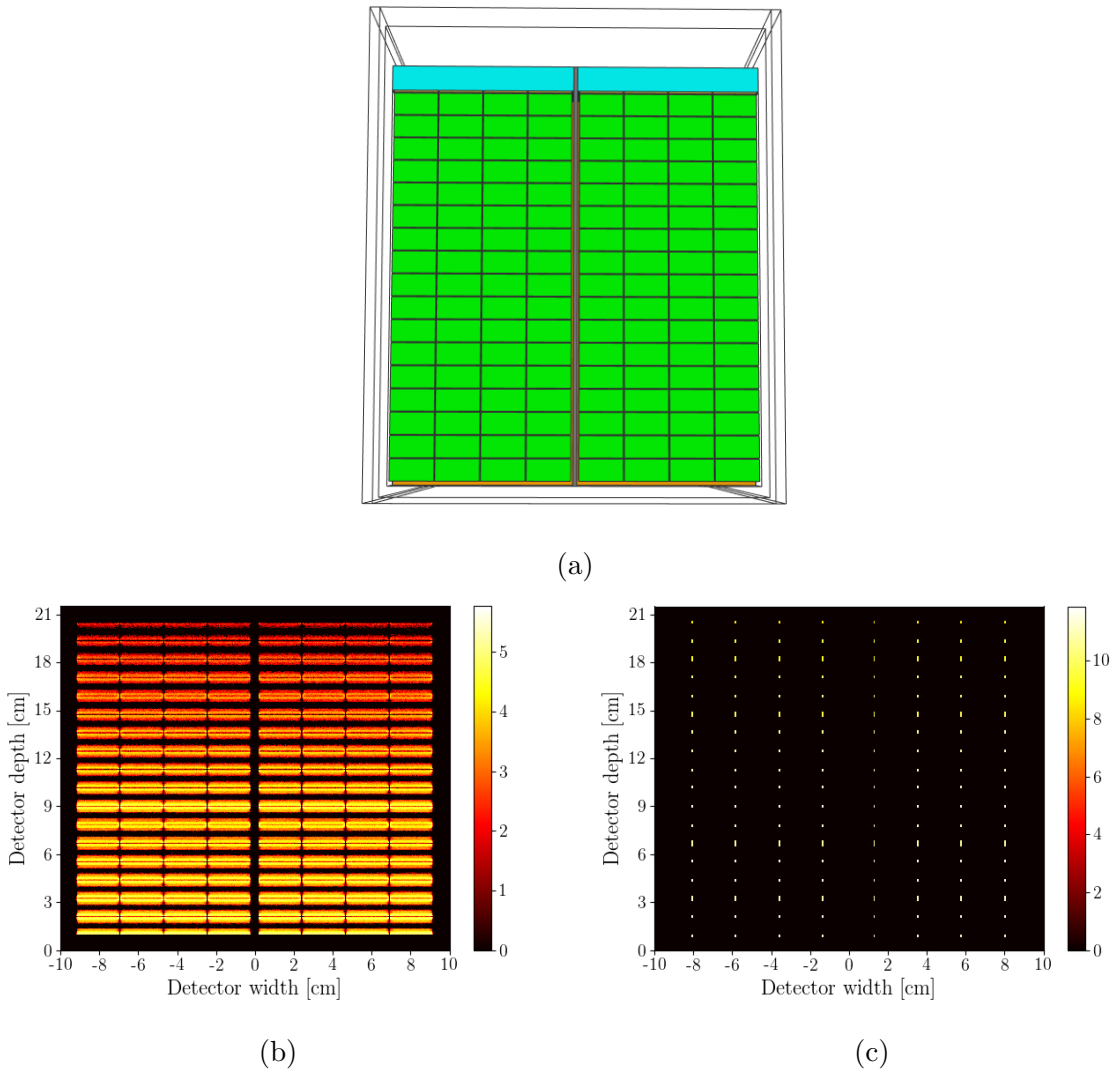

(a)

(b)

(c)

Figure 6.7: Two-column Multi-Grid detector module top view (a) and detection coordinates from hit; raw coordinates (b) and coordinates projected to the centre of the cell (c). Colorbars represent the count rate.

From these quantities the 'measurable' E_{final} neutron energy, and therefore the energy transfer (E_{trf}) can be calculated similarly to the real measurements:

$$E_{trf} = E_{initial} - E_{final}, \tag{6.4}$$

where E_{final} is determined from the t ToF and the r flight distance as $E_{final} = \frac{1}{2} m_n \frac{r^2}{t^2}$.

An example for the simulated energy transfer spectrum is given in Figure 6.8 in a two-column detector module irradiated with a mono-energetic neutron beam of 5.1 meV (4 Å). The elastic peak appears centred around 0 meV. Similarly to the ToF spectrum in Figure 6.6a, a smaller fraction of inelastically scattered neutrons appearing on the negative side of the spectrum, consist of the neutrons that gained energy in scattering, while the shoulder on the positive side consists of the neutrons that lost energy in inelastic scattering, or had an increased ToF due to elastic scattering, and therefore appear as slower. In the case of the mono-energetic neutrons, minor peaks also appear in the close proximity of the elastic peak on the positive side, belonging to a few rows of backscattering from the short blades within the grid. These peaks are smeared out for the longer flight paths, deeper in the grid structure.

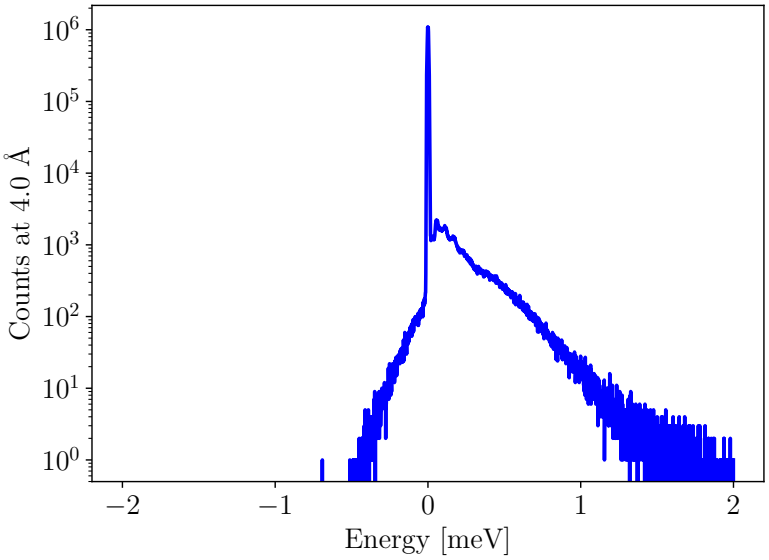

Figure 6.8: Energy transfer in two-column detector module with 5.1 meV (4 Å) incident neutron energy.

However, the simulation allows access to otherwise not measurable quantities as well. All properties of the primary neutrons are provided through their path, like the real $E_{neutron,final}$ before conversion, or the conversion position. The momentum vector of neutrons and all its parameters are also available (polar and azimuthal angle, etc.). Some of these parameters, and other secondary ones derived from these are used in the current study to monitor the correctness of the implementation, as well as for understanding the internal processes of the neutron scattering in the detector.

The simulation studies are performed in models of specific detectors, derived from

the hereby described general model. The model is validated against measured data from previously performed detector tests with different Multi-Grid demonstrators. All the specific simulated detector geometries and their utilisation in the validation and the optimisation are introduced in the following.

6.2.1 IN6 demonstrator

A six-column Multi-Grid prototype has been tested [30] at the IN6 [78] instrument at the ILL. The detector is built up from 6 × 16 grids, 4 × 17 cells in each grid (see Figure 6.9a), with no shielding at the rear end of the grids. As a single grid is 9.15 cm wide, 21 cm deep and 2.26 cm high, one column is 37.8 cm high, and the whole detector is the size of roughly 60 cm × 10 cm × 40 cm. The detector is filled with Ar/CO_2 (90/10 by volume) at nominal room temperature and pressure. The distance from the sample position to the front surface of the grids is 248 cm, as the columns of grids are placed with a curvature that meets this radius. The demonstrator (Figure 6.9a) was tested with neutron beams of 4.87, 3.87 and 3.15 meV (i.e. 4.1, 4.6 and 5.1 Å, respectively), irradiating the entire entrance surface.

The model of the IN6 demonstrator (see Figure 6.9b) is derived from the afore-described general Multi-Grid detector model with the parameter set given in Table 6.1. As this study is focusing on the qualitative impact of the grid structure, the detector housing is neglected from the simulation. The model was validated against the measured and published ToF spectra. Due to the lack of data on the measurement setup (e.g. exact chopper settings and timing references), the measured and simulated ToF spectra are compared either in a relative time scale, or all of them are scaled to the time scale of the simulation, in which the neutrons and their respective ToF are generated at the sample position.

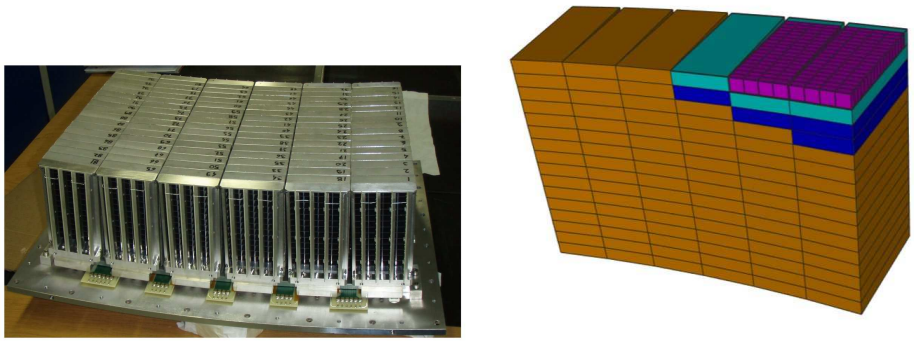

(a) (b)

Figure 6.9: As built IN6 prototype (a) and its Geant4 model (b).

The detector geometry is irradiated with pencil and targeted beams, in order to illuminate the entrance surface (see Figure 6.10), both with sharply mono-energetic and Gauss-smeared initial neutron energy distributions of 4.87, 3.87 and 3.15 meV (4.1, 4.6 and 5.1 Å). For preparing the demonstrative study on the 2-dimensional distributions of the ToF spectra as the function of the depth of detection, a minor simplification was performed: for this demonstration only 1 column of the detector model was used, since in this case z-coordinate (of hits) one-to-one corresponds to the detection depth in the detector, leading to an easy readout.

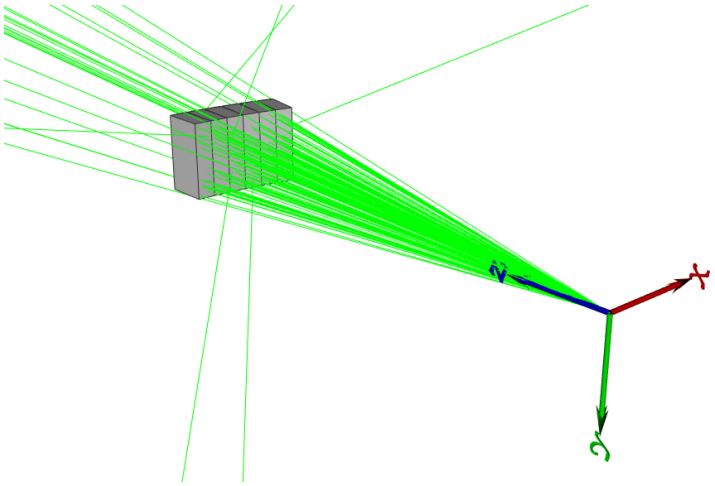

Figure 6.10: Geometry view of the IN6 Geant4 detector model in grey, irradiated with a targeted beam, where neutron tracks appear in green.

6.2.2 CNCS demonstrator

A two-column Multi-Grid prototype (see Figure 6.11) has been tested [31] at the CNCS (Cold Neutron Chopper Spectrometer) [79] instrument at the SNS. On one hand, the results of the experiment are also used for the validation of the Geant4 Multi-Grid model, while on the other hand, the simulated CNCS demonstrator geometry is used for simulations to explore and distinguish the different sources of scattered neutron background, and their impact on the measured data.

The built demonstrator columns consist of 2×48 grids, with 1 mm Gd_2O_3 shielding on the rear end of the grids, and a 2 mm thick MirroBor [49] rubber layer with 80 mass % natural B_4C content is also inserted between the columns to reduce cross-scattering. As a single grid is 9.15 cm wide, 21 cm deep and 2.25 cm high, one column is 1.13 m high. The columns are placed in a ~ 21 cm $\times$ 25 cm $\times$ 140 cm a aluminium vessel, and the whole detector volume is filled with Ar/CO_2 (80/20 by volume) counting gas at nominal room temperature and pressure.

The Geant4 model of the detector was derived from the general Multi-Grid detector model with the same parameters, as it is shown in Table 6.1. In this model some of the instrument components are also present. The measurement chamber is filled with 'tank gas': Ar/CO_2 (98/2 by volume) also at nominal room temperature and pressure. Tank gas is the gas in the cylindrical chamber on the flight path between the sample and the detector. A simplified model of the sample environment is also implemented. It consists of a double-wall aluminium cylinder with radii of 10 and 12 cm and a 2 mm wall-thickness, representing the cryostat, and a 0.5 mm thick aluminium window with 74 cm radius (see Figure 6.12), representing the barrier between air and tank gas. In addition a 2° collimator is involved, placed between the cryostat and the aluminium window. The collimator is built of 136 pieces of 1 m high and 10 cm long stainless steel blades with 2×10 μm Gd_2O_3 painting.

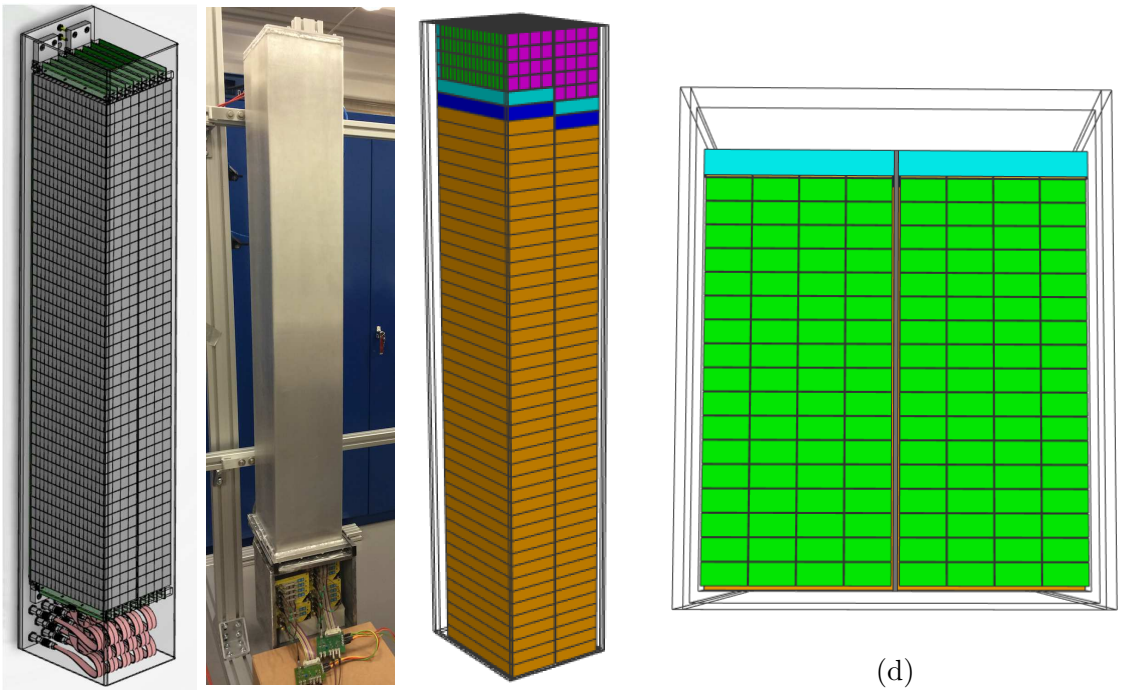

(a) (b) (c) (d)

Figure 6.11: The CNCS demonstrator: technical drawing in CATIA V6 [80] (a, source of plot: [31]), built prototype (b, source of plot: [31]) and Geant4 model (c side view and d top view).

α-, γ- and fast neutron background components are omitted from the simulation, as the remnant background is negligible in comparison with the implemented instrument-related background sources [31]. A series of tests are performed and published with this measurement setup, and the high statistics results with a vanadium sample [31]

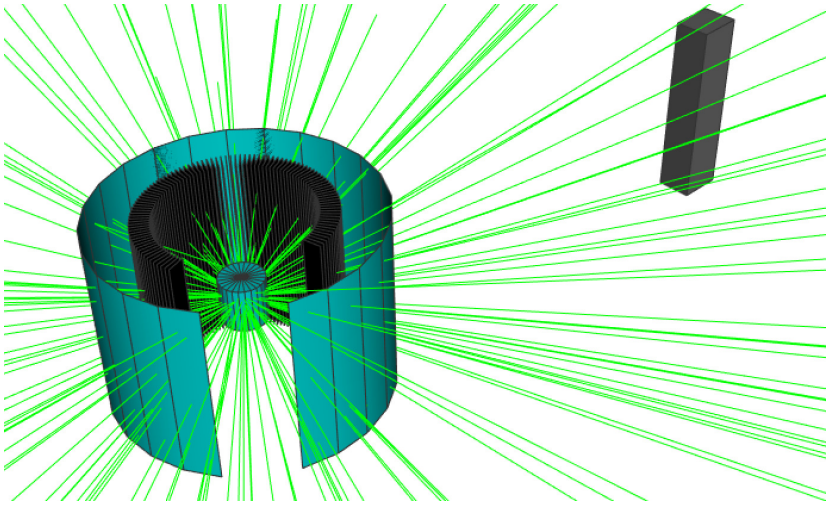

Figure 6.12: Geometry view of CNCS Geant4 model with a simplified sample environment, 4π-source and detector module. The aluminium cryostat (cyan) is surrounded by the 2° collimator (grey), and an aluminium window (also cyan). The detector module is presented in grey, and the neutron tracks appear in green.

at 1.0, 3.678 and 3.807 meV (i.e. 9.04, 4.72 and 4.64 Å, respectively) are selected for simulating. The simulations are performed with multiple geometry configurations, e.g. with and without sample environment or detector vessel, as well as with multiple neutron generators, e.g. a targeted beam irradiating the entire detector surface and a 4π-source, all with mono-energetic and Gaussian initial neutron energy distributions. The σ of the Gaussian distribution is chosen as 0.006 meV for the 1.0 and 0.030 meV for the 3.678 and 3.807 meV incident neutron energies, respectively, to fit the measured data, considering the known 1 % resolution of the CNCS instrument [81, 82].

Raw and derived quantities, like ToF, flight-distance and energy transfer are simulated for validation purposes, and the energy transfer spectra are chosen to study the scattered neutron background in the CNCS geometry. The flight distance and the energy transfer are derived from the hit positions projected to the centre of the cell.

6.2.3 CSPEC module

The CSPEC detector model, unlike to the previous ones, is not based on a built demonstrator, but on the early design [83] of the detector module of the CSPEC instrument at the ESS. As the results of current thesis take part in the development of the Multi-Grid detector design, the CSPEC detector model is used for simulations for design optimisation.

This module is similar to the CSPEC module, being a two-column module placed in an aluminium vessel. This design has wider grids, made of 6 × 16 cells, and 140

grids are stacked in a column, and the application of the long blade coating is under consideration. The Geant4 model of the detector was derived from the general Multi-Grid detector model with the same parameters, as shown in Table 6.1, with a minor simplification of the aluminium vessel: it is rectangular, with a flat front window, unlike the one to be built, which is slightly curved, so that multiple modules can fit together. In this model the printed circuit boards (PCB) of the read-out electronics are also included, being placed in the detector vessel and represented as layers of aluminium and polyethylene at the top and the bottom of the vessel. Also, 2 sheets of shielding are applied at the top and bottom of the front window, adequately sized to shield the PCBs, as it is planned for the real detector (see Figure 6.13).

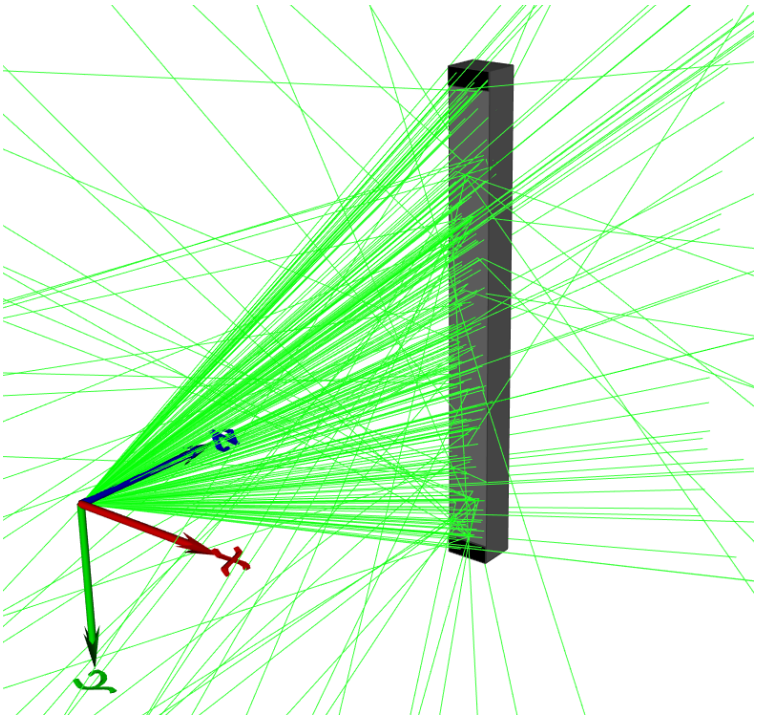

Figure 6.13: Geometry view of CSPEC Geant4 model with isotropic point source of neutrons (in green), targeted towards the detector window.

As this model is primarily used for shielding optimisation, it involves pre-defined volumes for shielding materials for three of the afore-introduced common shielding topologies. The size of all shielding volumes are maximised by the aim of having minimum dead area in the overall detector design:

- 'End-shielding': The surface of the shielding meets the dimensions of the cell. The maximum feasible thickness is 2 mm, defined by the space between the last coated blade and the end blade.

- 'Interstack-shielding': The shielding surface area meets the dimensions of the columns, and the maximum feasible thickness is 6 mm, i.e. the width of the gap between the columns.

- 'Side-shielding': The shielding surface is defined by the size of the vessel wall. The shielding sheets do not extend beyond the front face of the columns, as this would interfere with the neighbouring module placement. The maximum feasible thickness is 3.5 mm, i.e. the gap between the columns and the vessel wall.

The listed shielding topologies are modelled with both 'black material' (ideal total absorber) and common shielding materials. All shielding materials are used with natural isotope composition and in a realistic chemical form, with a representative carrier matrix, if necessary:

- B_4C
- Cd
- LiF
- 50% Gd_2O_3 + 50% polyethylene (representing acrylic paint as a typical carrier)
- black material

All materials in the model are the compositions of standard Geant4 materials except aluminium, whose poly-crystalline structure is enabled with the help of the NCrystal [63] library. The black material is emulated via an MCPL [53–55] particle filter, which is set to kill all particles that enter the respective volumes. A customised physics list is used for the simulations due to the thermal scattering on the high hydrogen-content of the polyethylene in the PCBs.

In order to get a clear view of the intrinsic scattering, the detector is irradiated with mono-energetic neutrons, and all instrument related effects are excluded from the Geant4 simulation. The neutrons are generated isotropically at the sample position as a point source and are targeting the detector window, as shown in Figure 6.13. The distance from the source to the detector front window is 3.5 m, and the sensitive area of the detector window covers a 0.080 sr solid angle. The neutron energies are chosen at and 511.3, 81.8, 25.3, 5.1 and 0.8 meV (0.4, 1, 1.8, 4.0 and 10.0 Å, respectively), meeting the operational range of the CSPEC instrument extended down to the Cd/Gd cutoff. All simulations are performed with 2×10^7 neutrons.

6.2.4 Simulated quantities for shielding optimisation

The primary, directly measured or derived quantities of the measurements and therefore the simulations have already been introduced in Section 6.2. However, as the final goal of the current thesis is the increase of Signal-to-Background Ratio via shielding and vessel design optimisation, this complex but practically highly relevant quantity serves as figure of merit.

In order to compare the different detector components, the vessel window, the long blade coating and the shielding geometries and materials, a 'reference detector' is defined: the detector in the vessel, with long blade coating, but without any shielding. This is the basic geometry to improve, and the SBR simulated in all geometry-variants are compared to the one of this starting point in the whole study.

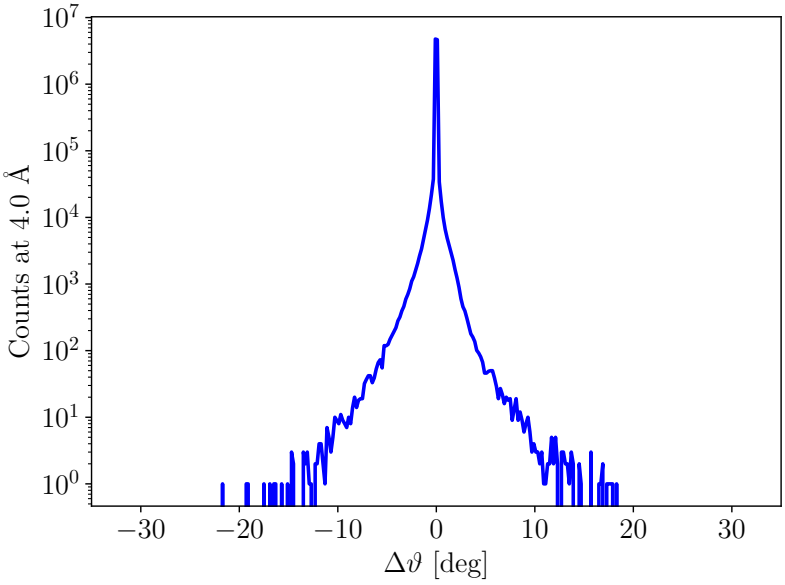

Figure 6.14: $\Delta\vartheta$ of initial polar angle and the one calculated from detection coordinates with 5.1 meV initial energy (4 Å).

The Signal/Background discrimination is based on the change of the polar angle (ϑ) of the neutrons initial direction, and the one calculated from detection coordinates, $\Delta\vartheta = \vartheta_{final} - \vartheta_{initial}$ as presented in Figure 6.14 for 5.1 meV (4 Å) neutrons. A trenchant peak of non-scattered neutrons is visible at $\Delta\vartheta = 0°$, and a continuous scattered neutron background from $-23°$ to $23°$, reflecting the size of the module. It has to be mentioned that this definition is slightly different from the one applied in the related publication [84], which is based on the momentum vector of the neutron. The current Signal/Background discrimination is more realistic, as it reflects the same concept of discrimination that is applied in real measurements, contrary to the highly

precise, but rather theoretical solution chosen in [84]. Compared to the publication, the changes in the simulation results are minor, and the conclusions remain the same.

The discrimination of scattered and non-scattered neutrons is performed in the following way: neutrons are taken as non-scattered, if $-0.2° \leq \Delta\vartheta \leq 0.2°$, which corresponds to the maximum resolution of the detector for the front cells, determined by the cell size. This discrimination allows to define the SBR with only the above defined non-scattered neutrons as signal, while the background only involves the intrinsic neutron scattering in the detector:

$$SBR_{converted\ neutrons} = \frac{N_{non-scattered}\Big|_{-0.2° \leq \Delta\vartheta \leq 0.2°}}{N_{scattered}} \tag{6.5}$$

Hereinafter this SBR definition is used without any further indication. It has to be emphasized that this definition is not the peak to background ratio that can be read from a measured spectrum, but it is calculated on the basis of this simulation-specific internal discrimination.

In Figure 6.15 and 6.16 the comparison of the total and non-scattered ToF and energy transfer spectra are given for 5.1 meV (4 Å) neutrons, respectively.

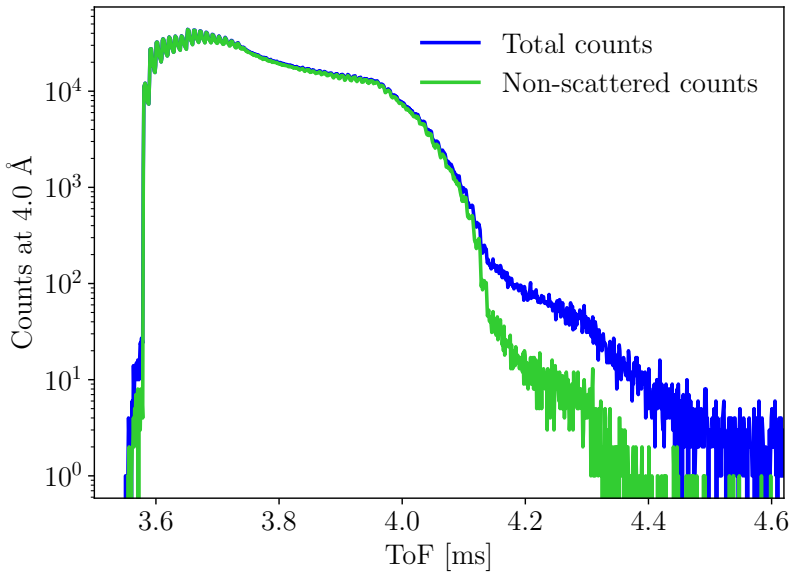

Figure 6.15: Comparison of ToF spectra from all and non-scattered neutrons at 5.1 meV initial energy (4 Å).

The afore-described scattered neutron background contributions in the ToF spectrum in Figure 6.15 are clearly identified by this definition. In Figure 6.16 the simulated energy transfer spectra are produced with mono-energetic incident neutrons

(Figure 6.16a) and with a typical Gaussian initial energy distribution (Figure 6.16b) with 1% standard deviation. It is shown that the applied realistic discrimination condition is imperfect, as the nominally 'Non-scattered' systematically contains scattered neutrons as well, but this is natural due to the physical resolution of the detector.

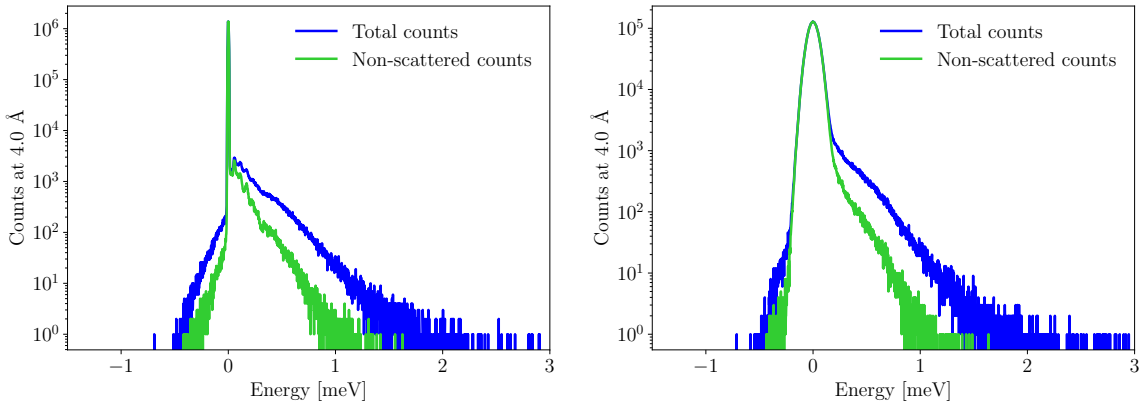

(a) (b)

Figure 6.16: Comparison of energy transfer spectra from all and non-scattered neutrons with mono-energetic (a and Gaussian b initial neutron energy distribution at 5.1 meV initial neutron energy (4 Å).

The so-defined SBR (Equation 6.5) is presented for the afore-introduced unshielded reference detector, as it is demonstrated in Figure 6.17. It reveals that the SBR monotonically increases with the wavelength of the incident neutrons, and covers a large dynamic range in the operational region of the CSPEC instrument. These observations indicate that the proper detector shielding is more important for thermal neutrons than for cold neutrons, where the SBR is inherently lower. The impact on the scattered neutron background for all studied components and shielding is compared to this SBR in the followings. In this and later upcoming figures, the results of different wavelengths or energies are only connected for better visibility.

The uncertainties of the simulations are determined and propagated through all the calculations. The simulated signal and background are independent quantities with Poisson error, and their uncertainties are propagated to SBR (Equations Equations (6.5) and (6.6)) and relative SBR (Equations Equations (6.7) and (6.8)) via the Gaussian Error Propagation Law:

$$\sigma_{SBR} = \sqrt{\left(\frac{1}{B}\right)^2 \sigma_S^2 + \left(\frac{-S}{B^2}\right)^2 \sigma_B^2} \tag{6.6}$$

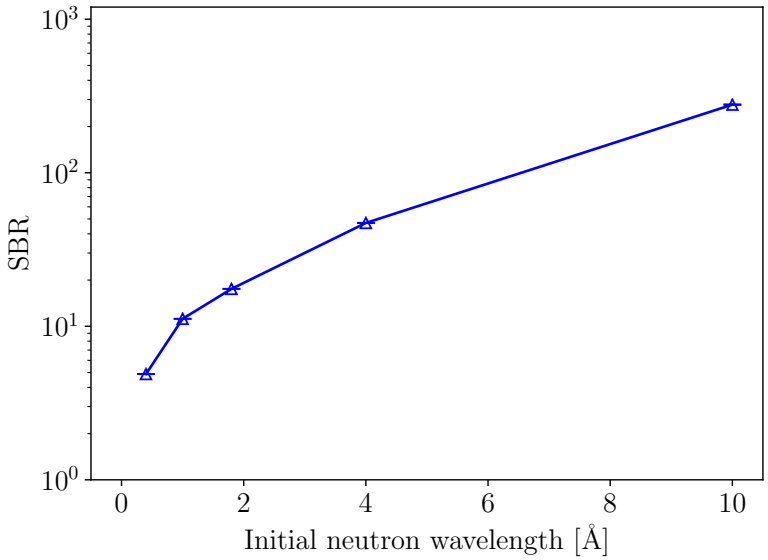

Figure 6.17: Simulated Signal-to-Background Ratio in the unshielded reference detector. The statistical uncertainties are too small to be discernible.

and

$$SBR_{Rel} = \frac{SBR - SBR_{Ref}}{SBR_{Ref}}, \tag{6.7}$$

$$\sigma_{SBR,Rel} = \sqrt{\left(\frac{1}{SBR_{Ref}}\right)^2 \sigma^2_{SBR} + \left(\frac{-SBR}{SBR^2_{Ref}}\right)^2 \sigma^2_{SBR_{Ref}}}. \tag{6.8}$$

With this, all the implemented detector models are introduced; the generic MCNP model for activity and gamma-background calculation, and the realistic Geant4 Multi-Grid detector model for the scattered neutron background study and shielding optimisation. All the quantities of interest are introduced for the background studies and the FoM is defined for the shielding study, as they are used in the subsequent chapters. In the following Part, the obtained results are presented and discussed for all tasks, starting with the activity and gamma background study in Chapter 7, followed by the validation of the Geant4 Multi-Grid model in Chapter 8 and its utilisation in the SBR optimisation in Chapter 9.

Part III

Results and discussion

Chapter 7

Neutron activation in Ar/CO_2-filled detectors

The neutron-induced activity and the prompt and decay gamma-production have been determined for the counting gas and aluminium vessel of a generic Ar/CO_2-filled detector model via analytical calculations and MCNP simulations, as well as their impact on the detector response, as described in Chapter 5 and Section 6.1.

For the whole study, the uncertainties of the simulation and the bibliographical data have all been taken into account. The MCNP6.1 simulations had high enough statistics, that the uncertainties of the simulated results were comparable to the uncertainties of the measured/bibliographical qualities used for the analytical calculations. The uncertainties of the total prompt photon production for all elements were below 5% for the entire neutron energy range, while the uncertainties of the main prompt gamma lines were below 10% for all elements, and less than 5% for argon and the elements of the aluminium alloy.

7.1 Neutron activation of detector filling gases

7.1.1 Prompt gamma intensity in detector counting gas

The total prompt photon production and its spectral distribution in Ar/CO_2 counting gas has been analytically calculated (Equation 5.3) on the basis of detailed prompt gamma data from IAEA PGAA Data-base [69]. The same data have been obtained with Monte Carlo simulation using MCNP6.1.

Prompt photon production normalised to incident neutron flux has been calculated for all mentioned wavelengths. The comparison of the results has shown that the

simulated and calculated total prompt photon yields qualitatively agree for argon, carbon, and oxygen within 2%, 11% and 21%, respectively.

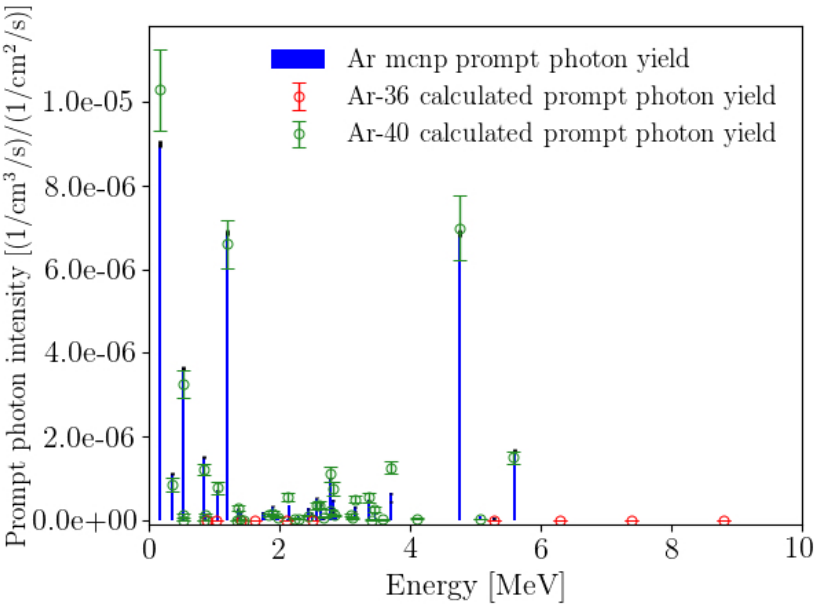

Figure 7.1: Prompt photon emission spectra from argon in Ar/CO_2, irradiated with unit flux of 25.3 meV (1.8 Å) neutrons. Results of analytical calculation with input data taken from IAEA PGAA Database [69] and MCNP6.1 simulation, as explained in the text.

It has also been shown that for these three elements proper cross-section libraries can be found (see Table A2), the use of which in MCNP simulations produces prompt photon spectra that qualitatively agree with the calculated ones. As an example Figure 7.1 shows the simulated and calculated prompt photon spectra from Ar in Ar/CO_2 for a 25.3 meV (1.8 Å), $\Phi = 1$ n/cm^2/s neutron flux, irradiating a 1 cm^3 volume. Since numerous databases lack proper prompt photon data, this agreement is not trivial to achieve for all the elements. For these three elements MCNP simulations can effectively replace analytical calculations, which is especially valuable for more complex geometries. For all these reasons hereinafter only the MCNP6.1 simulated results are presented. In addition, the obtained uncertainties of the photon intensities are generally within the size of the marker, here the error bars have been omitted. They are also omitted for some of the spectra for better visibility.

In Figure 7.2 it is shown that the prompt photon emission is dominated by argon, as expected due to the very small capture cross-section of the oxygen and the carbon; the argon total prompt photon yield is 3 orders-of-magnitude higher than the highest of the rest. According to Figure 7.1, within the argon prompt gamma spectrum, there

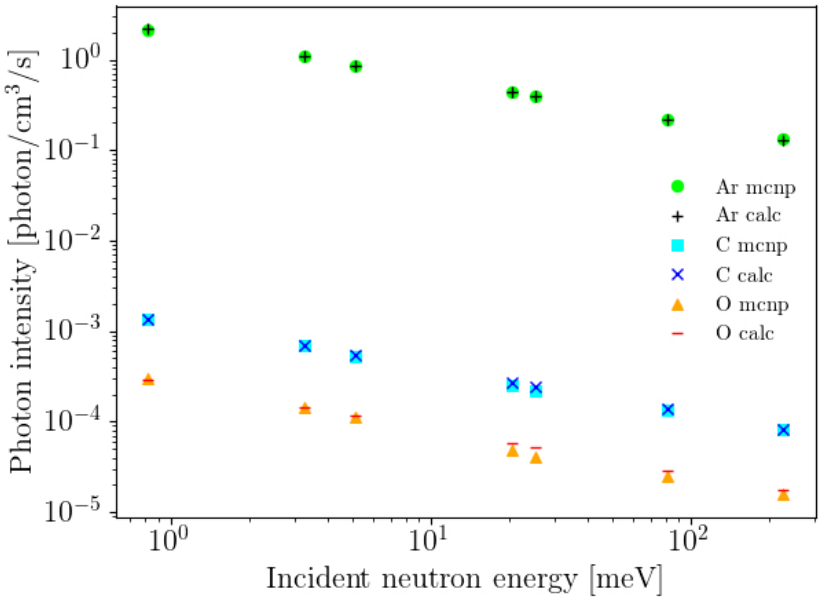

Figure 7.2: Elemental distribution of total prompt photon intensity in Ar/CO_2 counting gas irradiated with 10^4 n/cm^2/s flux of 25.3 meV (1.8 Å) neutrons. Results of MCNP6.1 simulation and analytical calculations with input data taken from IAEA PGAA Database [69], as explained in the text.

are 3 main gamma lines that are responsible for the majority of the emission; the ones at 167 ± 20 keV, 1187 ± 3 keV and 4745 ± 8 keV.

7.1.2 Activity concentration and decay gammas in detector counting gas

The induced activity in the irradiated Ar/CO_2 gas volume, as well as the photon yield coming from the activated radionuclei have been determined via analytical calculation, based on the bibliographical thermal (25.30 meV) neutron capture cross-sections and the half-lives of the isotopes in the counting gas (see Table A1). A similar calculation has been prepared on the bases of reaction rates determined with MCNP simulations for each isotope of the counting gas. Activity concentrations obtained from the calculation and the MCNP6.1 simulation agree within the margin of error, therefore only the MCNP simulations are presented.

As an example the build-up of activity during continuous irradiation time for 25.3 meV (1.8 Å) is given in Figure 7.3 for all the produced radionuclei.

It can be stated that the total activity of the irradiated counting gas practically equals the ^{41}Ar activity (see Figure 7.3), which is $1.28 \cdot 10^{-1}$ Bq/cm^3 at the end of

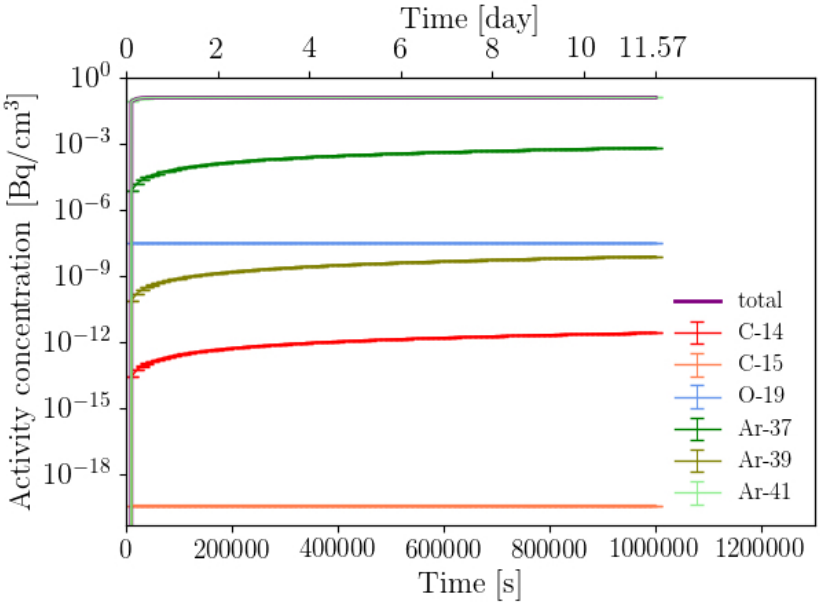

Figure 7.3: Build-up of isotopic and total activity concentration [Bq/cm^3] in Ar/CO_2 during 10^6 s irradiation time of 25.3 meV (1.8 Å) neutrons. Results of MCNP6.1 simulation, as explained in the text.

the irradiation time. This is 2 orders of magnitude higher than the activity of ^{37}Ar, which is $6.90 \cdot 10^{-4}$ Bq/cm^3, and 7 orders of magnitude higher than the activity of ^{38}Ar ($7.99 \cdot 10^{-9}$ Bq/cm^3) and ^{19}O ($3.19 \cdot 10^{-8}$ Bq/cm^3). The activity generated from of carbon is negligible.

The decrease of activity in the detector counting gas due to the natural radioactive decay is shown in Figure 7.4. After the end of the irradiation the main component of the total activity is the ^{41}Ar, although it practically disappears after a day (10^5 s), due to its short 109.34 m half-life with ^{37}Ar becoming the dominant isotope. However, in terms of gamma emission, all the remaining isotopes, ^{37}Ar, ^{39}Ar and ^{14}C are irrelevant, since they are pure beta-emitters. Therefore, with the above listed conditions there is only minimal gamma emission from the Ar/CO_2 counting gas after 10^5 s cooling time. For the same reason, the ^{41}Ar activity quickly saturates and accordingly it can contribute to the gamma emission during the irradiation as well. On the basis of these results, operational scenarios can be envisaged for instruments with Ar/CO_2-filled detectors. As for the planned operation mode of large area detectors at ESS, with a flushing of 1 detector volume of gas per day, assuming a V = 10^7 cm^3 detector volume (see Figure 5.1), $1.28 \cdot 10^6$ Bq/day activity production is expected. This means that by varying the flush rate and storing the counting gas up to 1 day before release, only negligible levels of activity will be present in the waste Ar/CO_2 stream.

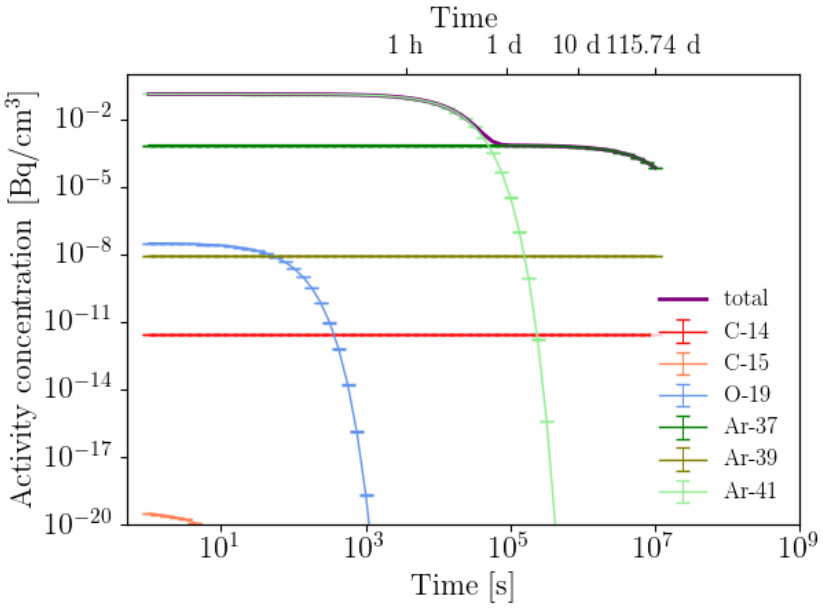

Figure 7.4: Decrease of activity concentration [Bq/cm^3] in Ar/CO_2 from end of the 10^6 s irradiation period with 25.3 meV (1.8 Å) neutrons. Results of MCNP6.1 simulation, as explained in the text.

Decay gamma emission of the activated radionuclei from a unit volume per second, with the activity reached by the end of the irradiation time has also been calculated. It is shown that the decay gamma yield practically wholly comes from the activated argon; the emission of the 1293.587 keV ^{41}Ar line is 8 orders of magnitudes higher than the yield of any other isotope.

Comparing the prompt and the decay gamma emission rates of all the isotopes, as it is shown in Table 7.1, it is revealed that for the argon, the prompt photon production ($3.9{\cdot}10^{-1}$ $\frac{\text{photon/cm}^3\text{/s}}{\text{n/cm}^2\text{/s}}$) and the saturated decay gamma production ($1.27 \cdot 10^{-1}$ $\frac{\text{photon/cm}^3\text{/s}}{\text{n/cm}^2\text{/s}}$) are comparable. There is a factor of 3 difference, whereas for carbon and oxygen the decay gamma production is negligible comparing with the prompt gamma production.

Figure 7.2 and Table 7.1 demonstrate that, as both the prompt and the decay gamma yield are determined by the neutron absorption cross-section, their energy dependence follows the $\frac{1}{v}$ rule within the observed energy range in case of all the isotopes of the Ar/CO_2 counting gas. Therefore activation with cold neutrons produces a higher yield, and the thermal fraction is negligible.

As it has been indicated, most of the activated nuclei are beta emitters, and some of the isotopes in the Ar/CO_2 are pure beta emitters, therefore the effect of beta radiation should also be evaluated. In Table 7.2, the activated beta-emitter isotopes in Ar/CO_2 and the most significant ones of them in aluminium housing have been collected. As an example, according to the calculated activity concentrations (see Figure 7.3), only

Table 7.1: Prompt and decay gamma emission from 80/20 V% Ar/CO_2 at 1 bar pressure and from Al5754 aluminium alloy, irradiated with 10^4 $\frac{1}{\text{cm}^2\ \text{s}}$ mono-energetic neutron flux for 10^6 s irradiation time. Results of MCNP6.1 simulation.

Element	Photon yield	Neutron wavelength [Å]																					
	$\left[\frac{1}{cm^3\ s}\right]$	0.6			1			1.8			2			4			5			10			
Ar	prompt	1.32	± 0.04	$\cdot 10^{-1}$	2.15	± 0.05	$\cdot 10^{-1}$	3.96	± 0.08	$\cdot 10^{-1}$	4.37	± 0.09	$\cdot 10^{-1}$	8.64	± 0.14	$\cdot 10^{-1}$	1.080	± 0.016	$\cdot 10^{0}$	2.150	± 0.025	$\cdot 10^{0}$
	decay	4.227	± 0.001	$\cdot 10^{-2}$	7.045	± 0.002	$\cdot 10^{-2}$	1.2667	± 0.0003	$\cdot 10^{-1}$	1.4090	± 0.0004	$\cdot 10^{-1}$	2.8179	± 0.0007	$\cdot 10^{-1}$	3.5224	± 0.0009	$\cdot 10^{-1}$	7.044	± 0.002	$\cdot 10^{-1}$
C	prompt	8.1	± 1.4	$\cdot 10^{-5}$	1.33	± 0.18	$\cdot 10^{-4}$	2.21	± 0.23	$\cdot 10^{-4}$	2.51	± 0.25	$\cdot 10^{-4}$	5.33	± 0.36	$\cdot 10^{-4}$	6.9	± 0.4	$\cdot 10^{-4}$	1.36	± 0.06	$\cdot 10^{-3}$
	decay	8.49	± 0.11	$\cdot 10^{-21}$	1.44	± 0.02	$\cdot 10^{-20}$	2.51	± 0.03	$\cdot 10^{-20}$	2.79	± 0.04	$\cdot 10^{-20}$	5.56	± 0.07	$\cdot 10^{-20}$	6.94	± 0.09	$\cdot 10^{-20}$	1.39	± 0.02	$\cdot 10^{-19}$
O	prompt	1.58	± 0.43	$\cdot 10^{-5}$	2.51	± 0.55	$\cdot 10^{-5}$	4.1	± 0.7	$\cdot 10^{-5}$	4.81	± 0.77	$\cdot 10^{-5}$	1.12	± 0.12	$\cdot 10^{-4}$	1.43	± 0.14	$\cdot 10^{-4}$	2.96	± 0.19	$\cdot 10^{-4}$
	decay	1.619	± 0.035	$\cdot 10^{-8}$	2.70	± 0.06	$\cdot 10^{-8}$	4.8	± 0.1	$\cdot 10^{-8}$	5.40	± 0.12	$\cdot 10^{-8}$	1.08	± 0.02	$\cdot 10^{-7}$	1.35	± 0.03	$\cdot 10^{-7}$	2.69	± 0.06	$\cdot 10^{-7}$
Al	prompt	8.27	± 0.11	$\cdot 10^{1}$	1.379	± 0.015	$\cdot 10^{2}$	2.47	± 0.02	$\cdot 10^{2}$	2.75	± 0.02	$\cdot 10^{2}$	5.44	± 0.03	$\cdot 10^{2}$	6.76	± 0.03	$\cdot 10^{2}$	1.300	± 0.005	$\cdot 10^{3}$
	decay	4.4419	± 0.0018	$\cdot 10^{1}$	7.401	± 0.003	$\cdot 10^{1}$	1.3288	± 0.0005	$\cdot 10^{2}$	1.4773	± 0.0006	$\cdot 10^{2}$	2.929	± 0.001	$\cdot 10^{2}$	3.6373	± 0.0015	$\cdot 10^{2}$	6.9981	± 0.0028	$\cdot 10^{2}$
Cr	prompt	2.0	± 0.1	$\cdot 10^{0}$	3.35	± 0.14	$\cdot 10^{0}$	6.0	± 0.2	$\cdot 10^{0}$	6.7	± 0.2	$\cdot 10^{0}$	1.34	± 0.03	$\cdot 10^{1}$	1.680	± 0.036	$\cdot 10^{1}$	3.35	± 0.05	$\cdot 10^{1}$
	decay	5.4774	± 0.0026	$\cdot 10^{-3}$	9.131	± 0.004	$\cdot 10^{-3}$	1.6418	± 0.0008	$\cdot 10^{-2}$	1.8263	± 0.0009	$\cdot 10^{-2}$	3.653	± 0.002	$\cdot 10^{-2}$	4.566	± 0.002	$\cdot 10^{-2}$	9.130	± 0.004	$\cdot 10^{-2}$
Cu	prompt	7.3	± 0.1	$\cdot 10^{-1}$	1.23	± 0.13	$\cdot 10^{0}$	2.20	± 0.17	$\cdot 10^{0}$	2.44	± 0.19	$\cdot 10^{0}$	4.88	± 0.29	$\cdot 10^{0}$	6.09	± 0.34	$\cdot 10^{0}$	1.22	± 0.05	$\cdot 10^{1}$
	decay	6.44	± 0.03	$\cdot 10^{-3}$	1.073	± 0.005	$\cdot 10^{-2}$	1.93	± 0.01	$\cdot 10^{-2}$	2.15	± 0.01	$\cdot 10^{-2}$	4.29	± 0.02	$\cdot 10^{-2}$	5.366	± 0.026	$\cdot 10^{-2}$	1.073	± 0.005	$\cdot 10^{-1}$
Fe	prompt	1.69	± 0.12	$\cdot 10^{0}$	2.84	± 0.16	$\cdot 10^{0}$	5.1	± 0.2	$\cdot 10^{0}$	5.7	± 0.2	$\cdot 10^{0}$	1.13	± 0.03	$\cdot 10^{1}$	1.412	± 0.037	$\cdot 10^{1}$	2.82	± 0.05	$\cdot 10^{1}$
	decay	2.34	± 0.06	$\cdot 10^{-4}$	3.9	± 0.1	$\cdot 10^{-4}$	7.0	± 0.2	$\cdot 10^{-4}$	7.80	± 0.21	$\cdot 10^{-4}$	1.56	± 0.04	$\cdot 10^{-3}$	1.95	± 0.05	$\cdot 10^{-3}$	3.9	± 0.1	$\cdot 10^{-3}$
Mg	prompt	1.61	± 0.12	$\cdot 10^{0}$	2.68	± 0.17	$\cdot 10^{0}$	4.84	± 0.23	$\cdot 10^{0}$	5.38	± 0.24	$\cdot 10^{0}$	1.08	± 0.03	$\cdot 10^{1}$	1.345	± 0.038	$\cdot 10^{1}$	2.67	± 0.05	$\cdot 10^{1}$
	decay	3.19	± 0.03	$\cdot 10^{-2}$	5.32	± 0.05	$\cdot 10^{-2}$	9.56	± 0.09	$\cdot 10^{-2}$	1.06	± 0.01	$\cdot 10^{-1}$	2.12	± 0.02	$\cdot 10^{-1}$	2.652	± 0.025	$\cdot 10^{-1}$	5.279	± 0.049	$\cdot 10^{-1}$
Mn	prompt	1.77	± 0.06	$\cdot 10^{1}$	2.95	± 0.08	$\cdot 10^{1}$	5.30	± 0.11	$\cdot 10^{1}$	5.89	± 0.12	$\cdot 10^{1}$	1.18	± 0.02	$\cdot 10^{2}$	1.48	± 0.02	$\cdot 10^{2}$	2.95	± 0.03	$\cdot 10^{2}$
	decay	9.3	± 0.1	$\cdot 10^{0}$	1.56	± 0.02	$\cdot 10^{1}$	2.80	± 0.03	$\cdot 10^{1}$	3.114	± 0.036	$\cdot 10^{1}$	6.23	± 0.07	$\cdot 10^{1}$	7.79	± 0.09	$\cdot 10^{1}$	1.56	± 0.02	$\cdot 10^{2}$
Si	prompt	2.75	± 0.18	$\cdot 10^{-1}$	4.52	± 0.23	$\cdot 10^{-1}$	8.1	± 0.3	$\cdot 10^{-1}$	9.1	± 0.3	$\cdot 10^{-1}$	1.815	± 0.046	$\cdot 10^{0}$	2.27	± 0.05	$\cdot 10^{0}$	4.55	± 0.07	$\cdot 10^{0}$
	decay	1.6812	± 0.0007	$\cdot 10^{-6}$	2.802	± 0.001	$\cdot 10^{-6}$	5.038	± 0.002	$\cdot 10^{-6}$	5.604	± 0.002	$\cdot 10^{-6}$	1.1207	± 0.0004	$\cdot 10^{-5}$	1.4008	± 0.0006	$\cdot 10^{-5}$	2.801	± 0.001	$\cdot 10^{-5}$
Ti	prompt	2.60	± 0.15	$\cdot 10^{0}$	4.4	± 0.2	$\cdot 10^{0}$	7.8	± 0.3	$\cdot 10^{0}$	8.70	± 0.35	$\cdot 10^{0}$	1.75	± 0.05	$\cdot 10^{1}$	2.18	± 0.06	$\cdot 10^{1}$	4.36	± 0.09	$\cdot 10^{1}$
	decay	1.595	± 0.008	$\cdot 10^{-3}$	2.66	± 0.01	$\cdot 10^{-3}$	4.779	± 0.025	$\cdot 10^{-3}$	5.316	± 0.028	$\cdot 10^{-3}$	1.063	± 0.006	$\cdot 10^{-2}$	1.329	± 0.007	$\cdot 10^{-2}$	2.66	± 0.01	$\cdot 10^{-2}$
Zn	prompt	4.93	± 1.38	$\cdot 10^{-1}$	8.3	± 1.9	$\cdot 10^{-1}$	1.49	± 0.27	$\cdot 10^{0}$	1.66	± 0.29	$\cdot 10^{0}$	3.32	± 0.43	$\cdot 10^{0}$	4.13	± 0.48	$\cdot 10^{0}$	8.3	± 0.7	$\cdot 10^{0}$
	decay	1.114	± 0.008	$\cdot 10^{-3}$	1.86	± 0.01	$\cdot 10^{-3}$	3.338	± 0.025	$\cdot 10^{-3}$	3.71	± 0.03	$\cdot 10^{-3}$	7.42	± 0.06	$\cdot 10^{-3}$	9.28	± 0.07	$\cdot 10^{-3}$	1.86	± 0.01	$\cdot 10^{-2}$

Table 7.2: Major endpoint energies and reaction energies of the main beta-emitters in Ar/CO_2 and in aluminium alloy Al5754 [3].

Isotope	Reaction product	Q_β [keV]	E_β [keV]	abundance	E_γ [keV]	abundance
^{40}Ar	^{41}Ar	2491.6 ± 0.7	1197	99%	1293	99%
			814	0.0525%	1677	0.0525%
			2491	0.8%	-	-
^{14}C	^{15}C	9771.7 ± 0.8	4472.88	63.2%	5297.817	63.2%
			9771.7	36.8%	-	-
^{18}O	^{19}O	4821 ± 3	3266.96	54%	1356.9	50%
					197.1	96%
			4623.86	45%	197.1	96%
^{27}Al	^{28}Al	4642.24 ± 0.14	2863.21	100%	1778.969	100%
^{55}Mn	^{56}Mn	3695.5 ± 0.3	735.58	14.6%	2113.123	14.3%
					846.771	98.9%
			1037.94	27.9%	1810.772	27.2%
					846.771	98.9%
			2848.72	56.3%	846.771	98.9%

^{41}Ar has a considerable activity in the counting gas. Therefore, the only beta emission that might be taken into account is the 1197 keV beta emission of ^{41}Ar. However, with the usual threshold settings [33] of proportional systems, the energy-deposition of the beta-radiation does not appear in the measured signal. Therefore on the one hand, the effect of beta radiation is negligible in terms of the detector signal-to-background ratio, while on the other hand, in terms of radiation protection, due to the few 10 cm absorption length in gas and few millimeters absorption length in aluminium, the beta exposure of the operating personnel from the detector is also negligible.

Consequently only the prompt and decay gamma emission have considerable yield to the measured background spectrum, and both of them are dominated by the ^{41}Ar, during and after the irradiation. A typical neutron beam-on gamma emission spectrum is shown in Figure 7.5, for 25.3 meV (1.8 Å), 10^4 n/cm^2/s incident neutron flux, calculated with saturated ^{41}Ar activity.

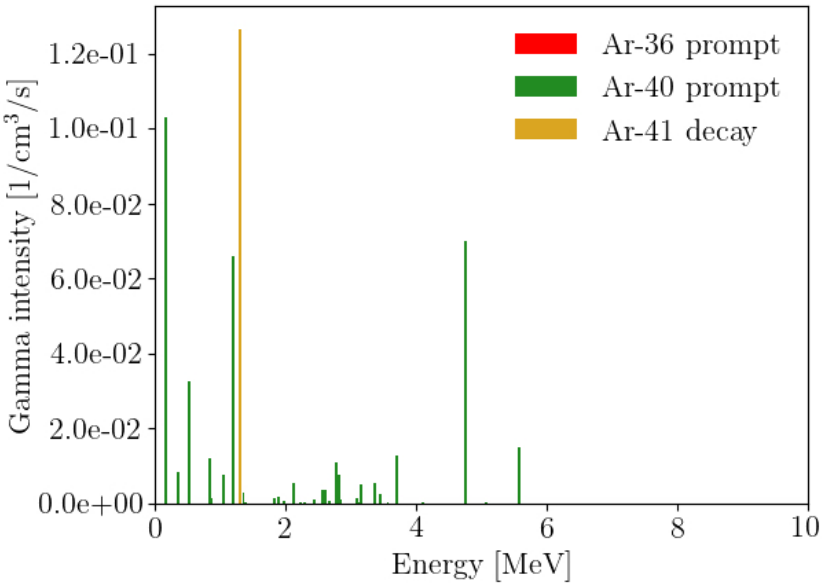

Figure 7.5: Overall prompt and saturated decay gamma spectrum from natural argon, irradiated with 10^4 n/cm^2/s flux of 25.3 meV (1.8 Å) neutrons. Result of calculation on the basis of reaction rates, simulated with MCNP6.1 and decay constant data from Table of Isotopes [3], as explained in the text.

In order to demonstrate how the gamma radiation background, induced by neutrons in the detector itself, affects the measured neutron signal, the NGR (Neutron-to-Gamma Response Ration, see Section 6.1) has been calculated for detector-filling gas, on the basis of Equations 6.2 and 6.3. As described before, Ar/CO_2 can be represented with ^{41}Ar in terms of gamma emission. According to its very small saturation

time, both the prompt and the decay gamma production have been considered in the background.

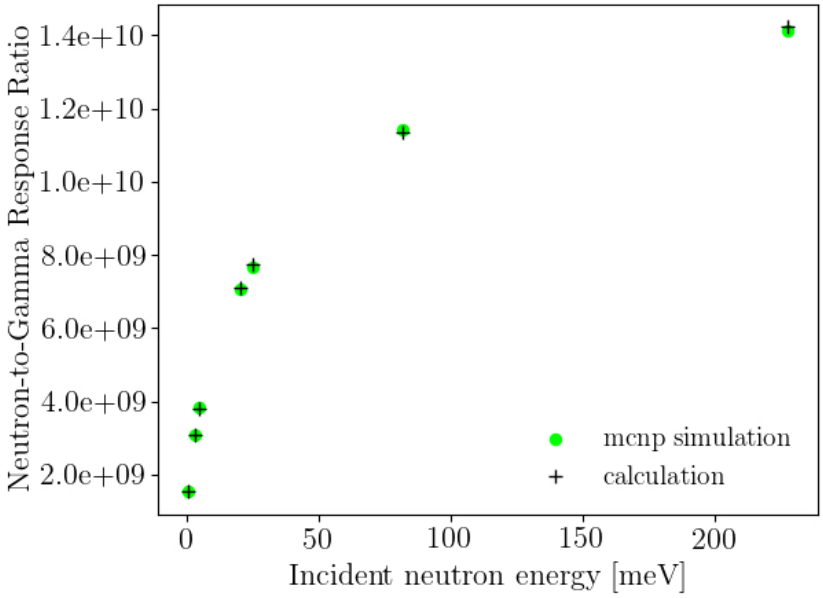

Figure 7.6: Simulated and calculated Neutron-to-Gamma Response Ratio of neutron-induced total gamma emission in argon, irradiated with 10^4 n/cm^2/s neutron flux.

In Figure 7.6 the good agreement of the calculated and the simulated signal-to-background ratios are shown, for the self-induced gamma background coming from neutron activation. For both cases, the signal-to-background ratio increases with the square root of the energy and varies between $10^9 - 10^{10}$ through the entire energy range. The calculation has been done with a 10^{-1} order of magnitude neutron efficiency, that is typical for a well-designed boron-carbide based neutron detector, and it has been shown that the effect of gamma background is really small, giving only a negligible contribution to the measured signal. Moreover, applying the same calculation for beam monitors, having the lowest possible neutron efficiency (approximated as 10^{-5}), the NGR is still 10^5, meaning that even for beam monitors the self-induced gamma background is vanishingly small.

7.2 Neutron activation of solid detector materials

7.2.1 Prompt gamma intensity in Al5754 aluminium frame

The prompt and decay photon yield of the aluminium frame or housing of the detectors have been determined via analytical calculation and MCNP6.1 simulation with the

same methods and parameters as the ones used for the Ar/CO_2. Prompt photon production normalised with incident neutron flux has been calculated.

For the Al5754 alloy as well, the calculated and MCNP6.1 simulated spectra qualitatively agree, although the agreement within the total prompt photon production varies from element to element, as shown in Table 7.3. Even with the best fitting choice of cross-section databases (Table A4), the difference is not higher than 10% for most elements, but for Mn and Zn the differences between the prompt photon productions are 28% and 23%, respectively. However, since for all isotopes of these elements the simulation results are conservative, the MCNP simulation remains reliable. Figure 7.7 is given as an example to show the produced prompt photon spectrum for $\Phi = 1$ n/cm^2/s neutron flux, irradiating an 1 cm^3 volume.

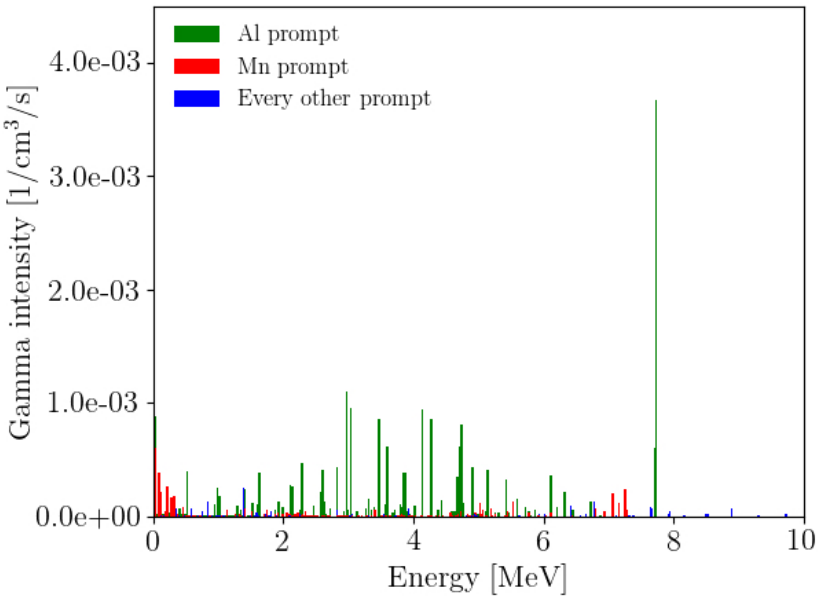

Figure 7.7: Prompt photon emission spectra from Al5754 aluminium alloy, irradiated with unit flux of 25.3 meV (1.8 Å) neutrons. Results of MCNP6.1 simulation, as explained in the text.

Comparing the prompt photon emission from a unit volume of Al5754 with the same for Ar/CO_2 (see Table 7.1) it can be stated that the prompt photon intensity coming from the aluminium housing is 3 orders of magnitude higher than the one coming from the counting gas. However, for large area detectors, like the ones used in chopper spectrometry, where the gas volume might be 10^5 cm^3 (see [21, 29, 85]) the prompt photon yield of the detector counting gas can become comparable to that of the solid frame.

The two main contributors to the prompt photon emission are the aluminium and the manganese (Figure 7.8); the aluminium total prompt photon yield is 2 order of

Table 7.3: Elemental composition of Al5754 [70], where m% is the mass fraction of each element in the alloy, and ΔI_{ph} is the maximum difference between calculated and simulated (MCNP6.1) total prompt photon production for all elements.

Element	m%	ΔI_{ph}
Al	97.4	10%
Cr	0.3	5%
Cu	0.1	9%
Fe	0.4	5%
Mg	3.6	6%
Mn	0.5	28%
Si	0.4	10%
Ti	0.15	10%
Zn	0.2	23%

magnitudes, while the manganese total prompt photon yield is 1 order of magnitude higher than the yield of the rest, respectively. Consequently, even the minor components in the aluminium alloy can be relevant for photon production, if they are having a considerable neutron capture cross-section. According to Figure 7.7, within the simulated Al5754 prompt gamma spectrum, there is one main gamma line that is responsible for the majority of the emission, 7724.03 ± 0.04 keV line of ^{27}Al. It has to be mentioned that in the analytically calculated spectrum a second main gamma line appears at 30.638 ± 0.001 keV, also from ^{27}Al; it only has a significant yield on the basis of IAEA data [69, 71], that is not reproduced within the simulation. However, the mentioned gamma energy is low enough that for practical purposes the MCNP simulation remains reliable.

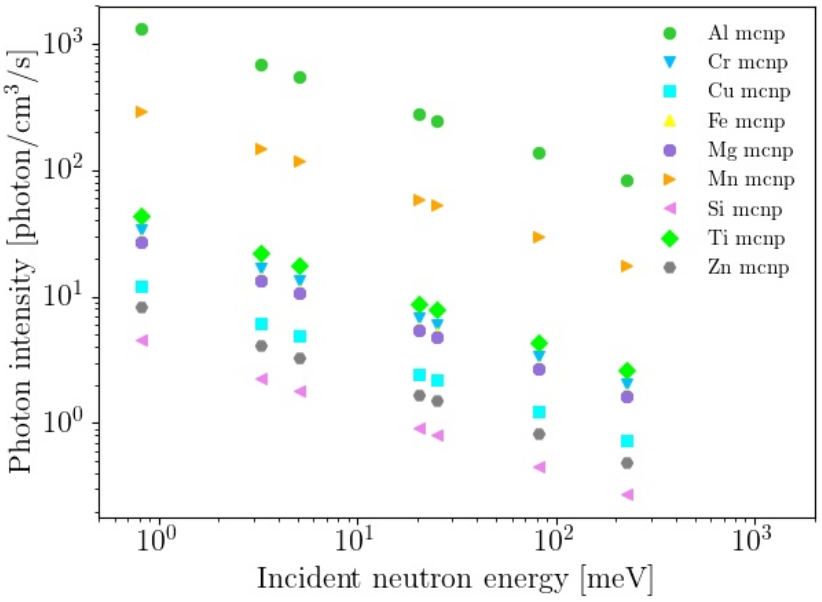

Figure 7.8: Elemental distribution of total prompt photon intensity in Al5754 aluminium alloy, irradiated with 10^4 n/cm^2/s flux of 25.3 meV (1.8 Å) neutrons. Results of MCNP6.1 simulation, as explained in the text.

7.2.2 Activity concentration and decay gammas in Al5754 aluminium frame

An analytical calculation has been performed using Equation 5.2 in order to determine the induced activity in the irradiated aluminium housing, as well as the photon yield coming from the activated radionuclides, with the same methods that have been used for the counting gas. The calculation was based on the bibliographical thermal neutron capture cross-sections and the half-lives of the isotopes in the AL5754 aluminium alloy (see Table A3).

An example of the activity build-up during irradiation time for 25.3 meV (1.8 Å) is presented in Figure 7.9 for all the produced radionuclei. According to Figures 7.9 and 7.11, for most of the isotopes in Al5754 the activity concentrations obtained from calculations and MCNP6.1 simulations agree within the margin of error or within the range of 5%. However, for a few isotopes the difference is significant. In the case of ^{51}Cr with the most suitable choice of cross-section libraries the largest discrepancy between the simulations and the calculations [86] is 13%. Also extra care is needed when treating Zn in the simulations; with calculations made on the basis of the thermal neutron cross-section data of Mughabghab [86], the discrepancies for ^{65}Zn, ^{69}Zn, ^{71}Zn are 5%, 7% and 10% respectively, while in the case of using the NIST database [87] for

the calculations, the differences were 18%, 3% and 1%. Since ^{64}Zn, the parent isotope of ^{65}Zn is the major component in the natural zinc, the usage of the first database is recommended. According to Table 7.1, the activity concentration of the zinc is 5 orders of magnitude smaller than the highest occurring activity concentration, hence the large difference between the calculated and the simulated result does not have a significant impact on the results of the whole alloy.

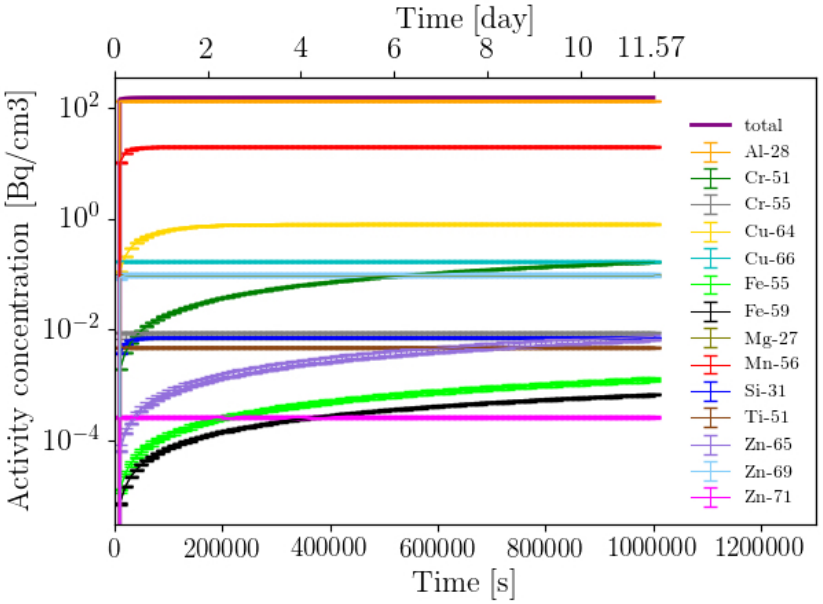

Figure 7.9: Build-up of isotopic and total activity concentration [Bq/cm^3] in Al5754 aluminium alloy during a 10^6 s irradiation time of 25.3 meV (1.8 Å) neutrons. Results of MCNP6.1 simulation and analytical calculations [3, 86], as explained in the text.

In Figure 7.9 it is demonstrated that the majority of the produced total activity is estimated to be due to ^{28}Al and ^{56}Mn, $1.33{\cdot}10^2$ Bq/cm^3 and $1.96{\cdot}10^1$ Bq/cm^3 at the end of the irradiation time, respectively. It is also shown that for all isotopes the activity concentration saturates quickly at the beginning of the irradiation time, therefore the decay gamma radiation is also produced practically during the entire irradiation time, with a yield constant in time.

The decay gamma intensity of the activated radionuclei from a unit volume has also been calculated, with the activity reached by the end of the irradiation time, like in case of Ar/CO_2 (see Table 7.1). It is shown that the decay gamma intensity is due to ^{28}Al and ^{56}Mn; their decay photon emission is 3 and 2 orders of magnitude higher then the rest. The decay gamma spectrum is dominated by the 1778.969 ± 0.012 keV line of ^{28}Al.

Figure 7.8 and Table 7.1 demonstrate that for aluminium and manganese the prompt photon production ($2.47 \cdot 10^2$ and $5.27 \cdot 10^1$ $\frac{\text{photon/cm}^3\text{/s}}{\text{n/cm}^2\text{/s}}$) and the saturated decay gamma production ($1.33 \cdot 10^2$ and $2.8 \cdot 10^1$ $\frac{\text{photon/cm}^3\text{/s}}{\text{n/cm}^2\text{/s}}$) are comparable; the yield of decay photons is 53–54% of that of the prompt photon ones, whereas for all the other isotopes the decay gamma production is less than 1% compared to the prompt gamma production.

Figure 7.10 depicts that the total gamma emission spectrum during the neutron irradiation is dominated by the aluminium. The majority of the total photon yield comes from the ^{27}Al prompt gamma emission, while the two main lines of the measured spectrum are the 1778.969 ± 0.012 keV ^{28}Al decay gamma and the 7724.03 ± 0.04 keV ^{27}Al prompt gamma line.

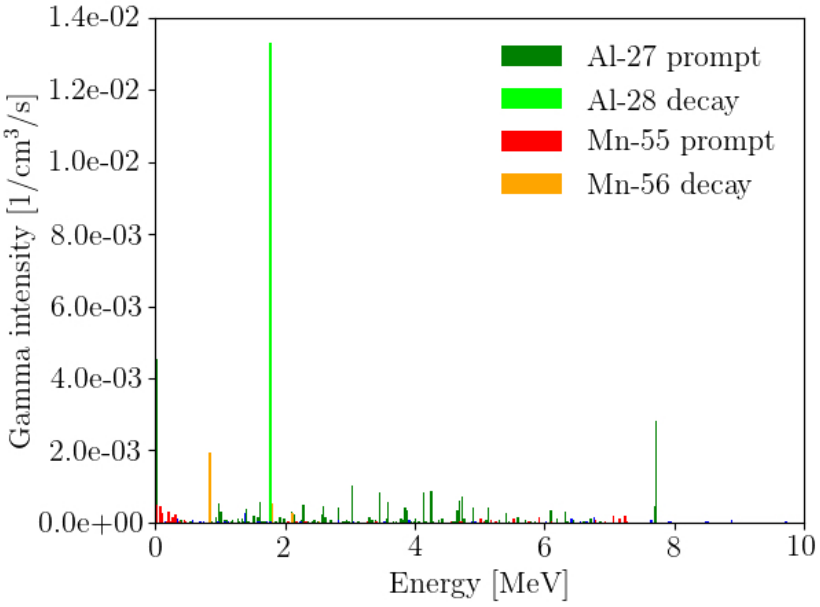

Figure 7.10: Overall prompt and saturated decay gamma spectrum from Al5754 aluminium alloy, irradiated with 10^4 n/cm^2/s flux of 25.3 meV (1.8 Å) neutrons. Result of calculation on the basis of reaction rates, simulated with MCNP6.1 and decay constant data from Table of Isotopes [3], as explained in the text.

The decrease of activity in the aluminium frame of the detector due to radioactive decay has also been calculated and the obtained results are shown in Figure 7.11, like in the case of Ar/CO_2 in Figure 7.4. There are three isotopes that become major components of the total activity for some period during the cooling time: ^{28}Al with 1 order of magnitude higher activity than the rest within 0–$6{\cdot}10^3$ s (10 min), ^{56}Mn with 2 orders of magnitude higher activity than the rest within $6{\cdot}10^3$–10^6 s (11 days), and ^{51}Cr with 1 order of magnitude higher activity than the rest from 10^6 s, therefore

the total activity decrease is relatively fast. However, because of the long half-life of ^{55}Fe, ($T_{\frac{1}{2}} = 2.73 \pm 0.03$ y), a small background activity is expected to remain for years after the irradiation.

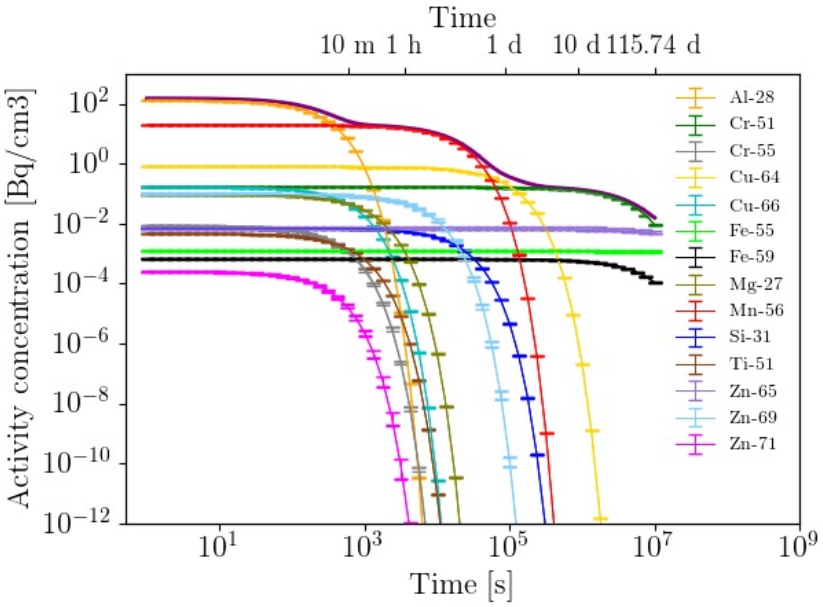

Figure 7.11: Decrease of activity concentration [Bq/cm^3] in Al5754 aluminium alloy from end of the 10^6 s irradiation period with 25.3 meV (1.8 Å) neutrons. Results of MCNP6.1 simulation and analytical calculations [3, 86], as explained in the text.

To sum up, the neutron-induced activity is determined for the aluminium detector housing and the Ar/CO_2 counting gas in a generic detector, and it was shown that the activity emission coming from flush mode operation is negligible for standard operation conditions. The prompt- and decay-gamma production was also determined for a generic detector, and the impact of gas activation sourced gamma background was also calculated, and found to be negligible compared to the neutron response. Consequently in the following the focus is moved to the scattered neutron background (Chapter 8) and its impact on the SBR (Chapter 9).

Chapter 8

The Multi-Grid detector model

A Geant4 model of the Multi-Grid detector has been developed with the aim to be used in the optimisation of the detector design, especially for shielding against scattered neutron background. Along these goals, the detector model has been implemented as described in Section 6.2, and validated against measured data from already published demonstrator tests (see Section 8.1). Along with the validation process, a preliminary study is also performed to explore the scattered neutron background in a Multi-Grid detector module (see Section 8.2), establishing the approaches for the optimisation of the shielding design in the CSPEC Multi-Grid module, which is planned to be used at the CSPEC Cold Chopper Spectrometer at ESS (see Section 1.2.1).

8.1 Validation of Geant4 Multi-Grid detector model

The implemented Geant4 model of the Multi-Grid detector is validated against measured data from demonstrator tests at the IN6 and CNCS instruments at the ILL and SNS, respectively. As the Multi-Grid detector is designed for inelastic instruments, the directly measured quantities are the ToF and the detection coordinates, and the information of interest is carried by derived quantities like the energy- and momentum-transfer. The ToF results of the IN6 irradiation are used for the qualitative validation (Section 8.1.1), while the measured ToF, flight distance and energy-transfer (Section 8.1.2) of the CNCS long-term test are used for the quantitative validation.

8.1.1 Validation against IN6 data

For the IN6 experiment, ToF spectra and 2D detection depth dependent ToF spectra are simulated with the IN6 detector model described in Section 6.2.1, and compared to the published measurements at 4.87, 3.87 and 3.15 meV energies (i.e. 4.1, 4.6 and

5.1 Å wavelengths, respectively). In Figures Figures 8.1 and 8.2 the comparison of the measured (Figures 8.1a, 8.1b and 8.2a) and the simulated ToF-spectra as a function of the depth of detection is presented with mono-energetic (Figures 8.1c, 8.1d and 8.2b) and Gaussian (Figures 8.1e, 8.1f and 8.2c) incident neutron energy distributions. At all wavelengths the main path of the incident detected neutrons clearly appears as a skewed line both in the measured and the simulated distributions. The angle of the path is related to the velocity of the neutrons.

Beside the main path, at 3.87 and 4.87 meV that are above the aluminium Bragg edge at 3.74 meV (i.e. 4.675 Å), [88, 89], the traces of the detected scattered neutrons appear as well. On the one hand, in the near surface region a triangle-shaped shadow appears beside the main neutron path, produced by the neutrons detected after scattering on the intermediate aluminium blades. On the other hand, a short, opposite direction skew line appears for these two wavelengths, both in the measured and simulated distributions, starting from the unshielded rear end of the detector, caused by a significant fraction of scattered neutrons coming from the detector end blade. Both effects are caused by the Bragg-scattering on aluminium and emphasise the need for targeted shielding in the detector.

With the reproduction of these ToF characteristics and scattering phenomena, the developed Geant4 model is qualitatively validated. For a quantitative validation, 1D ToF histograms are also simulated.

The simulated ToF spectra are quantitatively compared with the measured ones for all three energies. The simulations are produced with the same Gaussian initial energy distributions that were previously applied for the 2D ToF-depth studies. The standard deviations of the distributions are estimated to fit both the typical instrument energy resolution and the measured ToF data. In Figure 8.3 the measured and simulated ToF spectra are presented in a relative time scale. The IN6 Multi-Grid demonstrator has a considerable α-background [32], coming from the uranium and thorium content of the non-purified aluminium of the grids. This background is random and evenly distributed in time. Therefore, updated simulated spectra are reproduced for all wavelengths, where a subsequent background correction is applied. This is performed with a continuous, flat time-constant background added to the simulated ToF spectra, in order to obtain a better comparison with the measured results. The background is estimated to fit the average measured background. In the case of 3.15 meV, the background is not entirely flat, which is presumably caused by additional effects of the measurement setup and the instrument. As an example, adding the resolution [90] of the Fermi-chopper in the model would give a better description of the tails of the

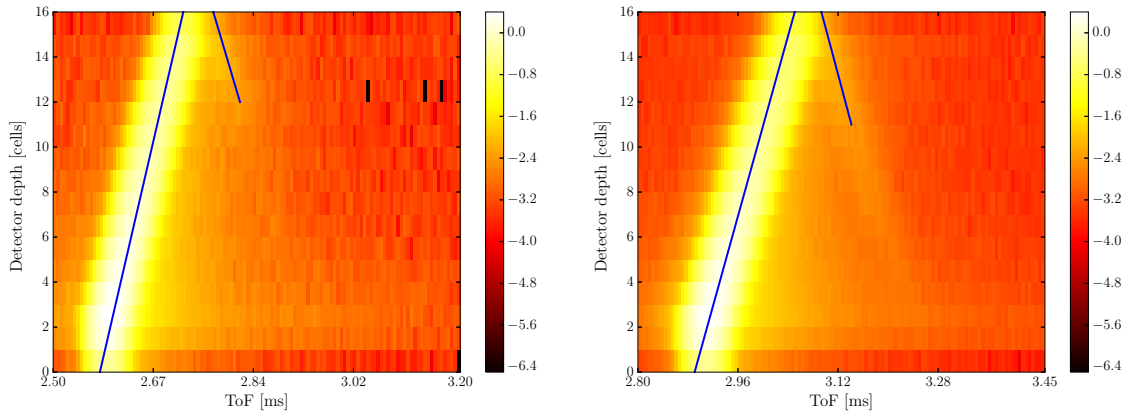

(a) Measured ToF at 4.87 meV (4.1 Å).

(b) Measured ToF at 3.87 meV (4.6 Å).

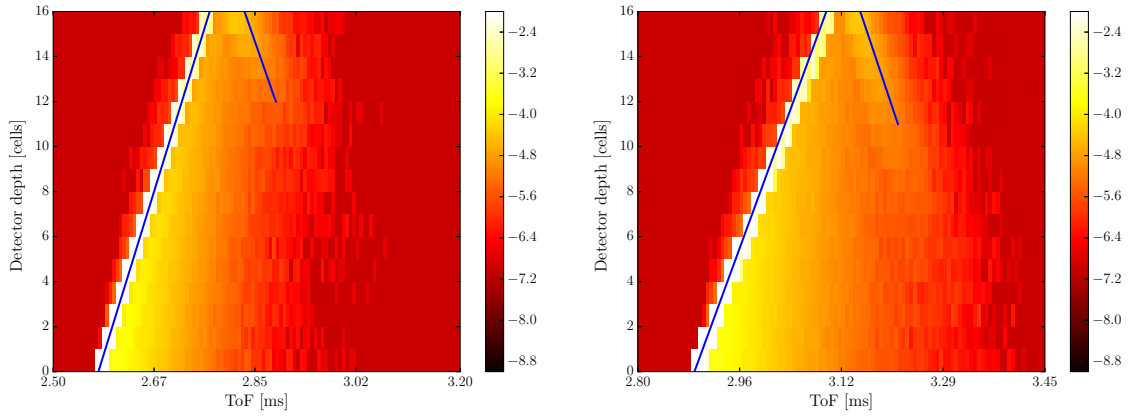

(c) Simulated ToF at 4.87 meV (4.1 Å).
E_{ini}: mono-energetic

(d) Simulated ToF at 3.87 meV (4.6 Å).
E_{ini}: mono-energetic

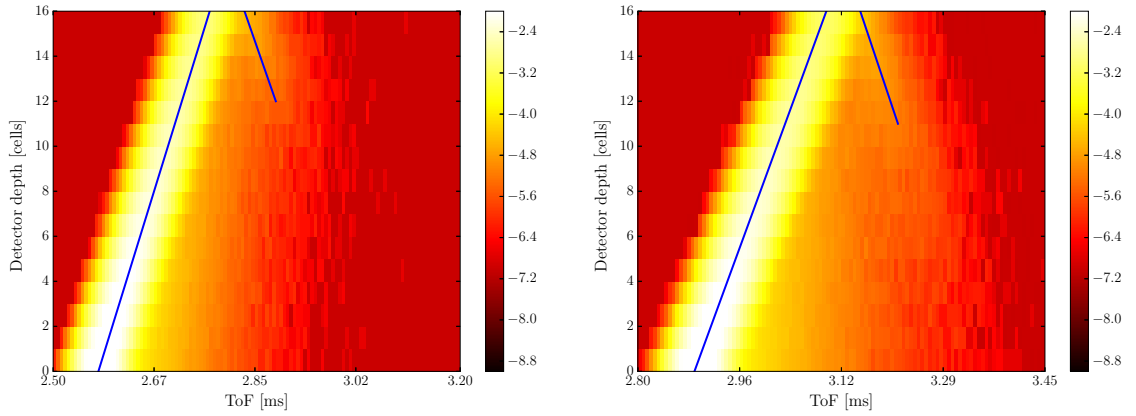

(e) Simulated ToF at 4.87 meV (4.1 Å).
E_{ini}: Gaussian

(f) Simulated ToF at 3.87 meV (4.6 Å).
E_{ini}: Gaussian

Figure 8.1: Time-of-Flight spectra as a function of the detection depth. Results of measurement at the IN6 experiment (Figures 8.1a and 8.1b, measured data taken from [30]) and Geant4 simulation with mono-energetic (Figures 8.1c and 8.1d) and Gaussian (Figures 8.1e and 8.1f) initial energy distributions. Time-of-Flight measured from sample position. Colorbars represent the count rate. (The 3 black lines in Figure 8.1a are given by pixels with 0 counts due to low statistics.)

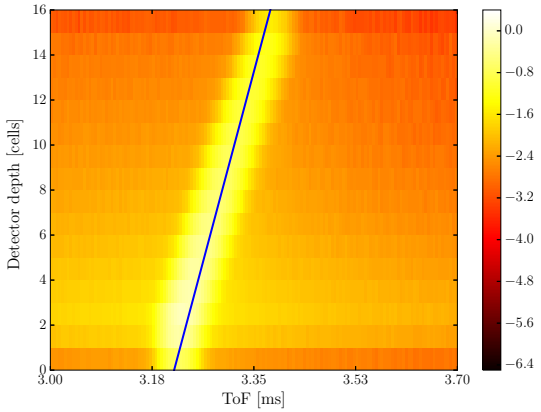

(a) Measured ToF at 3.15 meV (5.1 Å).

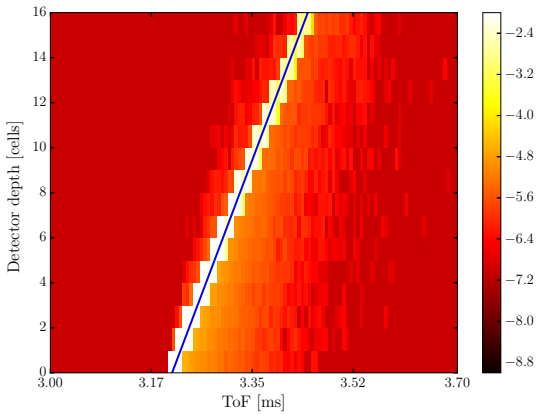

(b) Simulated ToF at 3.15 meV (5.1 Å).
E_{ini}: mono-energetic

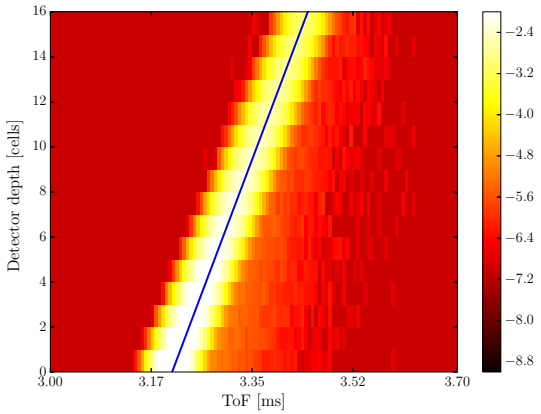

(c) Simulated ToF at 3.15 meV (5.1 Å).
E_{ini}: Gaussian

Figure 8.2: Time-of-Flight spectra as a function of the detection depth. Results of measurement at the IN6 experiment (8.2a, measured data taken from [30]) and Geant4 simulation with mono-energetic (8.2b) and Gaussian (8.2c) initial energy distributions. Time-of-Flight measured from sample position. Colorbars represent the count rate.

Gaussian ToF peaks. Due to lack of additional information it is impossible to estimate these effects.

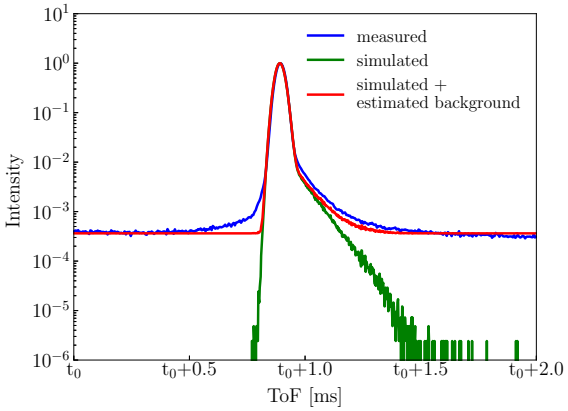

(a) Simulated ToF at 3.87 meV (4.6 Å).

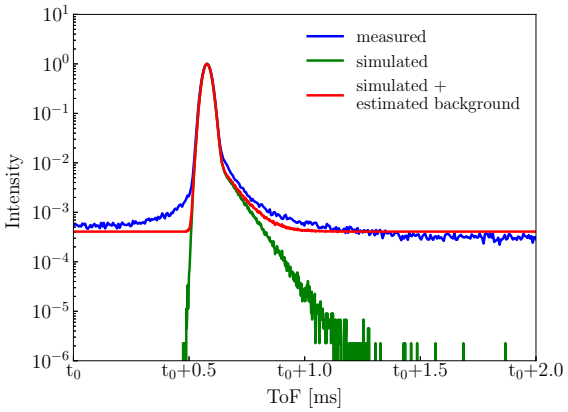

(b) Simulated ToF at 4.87 meV (4.1 Å).

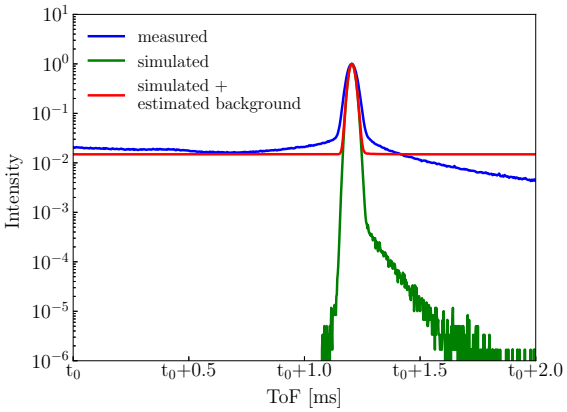

(c) Simulated ToF at 3.15 meV (5.1 Å).

Figure 8.3: Comparison of measured and simulated ToF spectra with and without α-background correction at 4.87 meV (8.3b), 3.87 meV (8.3a) and 3.15 meV (8.3c) in relative time-scale. Intensity of Time-of-Flight spectra is given as number of counts normalised to maximum. Measured data is taken from [30]. t_0 relates to the incidence of the neutron pulse on the sample position.

Figure 8.3 demonstrates that the measured and simulated ToF peaks agree at all the studied wavelengths. Moreover, by applying a correction of a continuous background, the right-hand-side decrease of the ToF spectrum is also reproduced quantitatively, with only a small discrepancy in the values at 4.87 and 3.87 meV.

These analysis results of the IN6 model and data serve as quantitative validation of the Multi-Grid simulation.

8.1.2 Validation against CNCS data

The simulations for the CNCS experiment are performed in the most detailed setup described in Section 6.2.2, involving all the afore-described geometrical and instrumental components, as a simplified sample environment (aluminium cryostat and radial collimators), the Ar/CO_2 atmosphere and the detector module irradiated with 1.0, 3.678 and 3.807 meV (i.e. 9.0, 4.7 and 4.6 Å, respectively) incident neutrons. A Gaussian initial energy distribution is applied with 1% standard deviation. The ToF and flight-distance data are compared only at 3.678 and 3.807 meV incident neutron energies (4.7 and 4.6 Å), below and above the aluminium Bragg-edge, as the measured as the raw data of the CNCS detector test [31] were provided for these two energies.

The measured and simulated ToF and flight distance spectra are compared in Figures 8.4 and 8.5. As shown in Figures 8.4a and 8.4b, a series of peaks appear in both measured and simulated flight distance spectra, relating to the geometrical cell structure of the grids. The resolution of the detector is affected by this cell structure, therefore these peaks are related to the rows of cells in the detector. The peaks are visible in the first 10–15 cm of the detector, where the majority of the neutrons are detected, therefore the statistics are the best. The falling tail of the spectra is determined by the neutrons detected in the rear cells of the detector, and by the scattered neutrons, having a longer flight distance. There is a difference in the cutoff of the two spectra, since the last row is not read out in the measurement, contrary to the simulation.

Both the overlaying peaks and the characteristics of the falling tails of the measured and simulated spectra are in good agreement at both energies below and above the aluminium Bragg-edge.

The measured and simulated ToF spectra are compared in Figure 8.5. The ToF is simulated from the sample position, while the experimental data are given relatively to the 16667 μs period of the SNS pulse. An arbitrary shift is applied on the measured spectra to overlay them with the simulated ones. This way the measured and simulated ToF peaks are fit at both energies; the shape and the width of the peaks give good agreement.

In both spectra the measured and simulated backgrounds also reasonably agree with the presence of some discrepancies between them. The source of these discrepancies is that not all instrument related effects are included in the simulation. For example instrument background radiation, initial ToF distribution of neutrons, and some of the sample environment components are omitted, since the aim of the current study focuses on understanding detector effects. However, the level of agreement of the measured

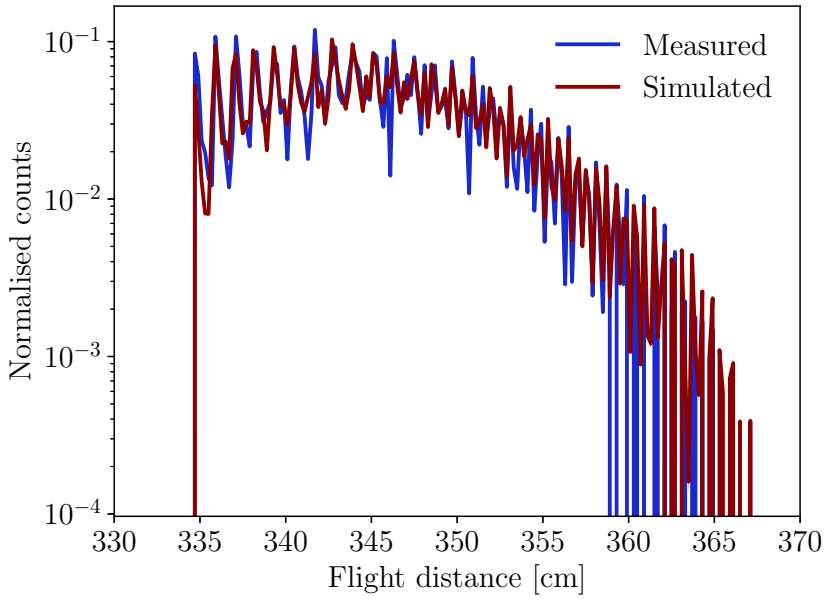

(a) Flight distance at 3.678 meV (4.7 Å).

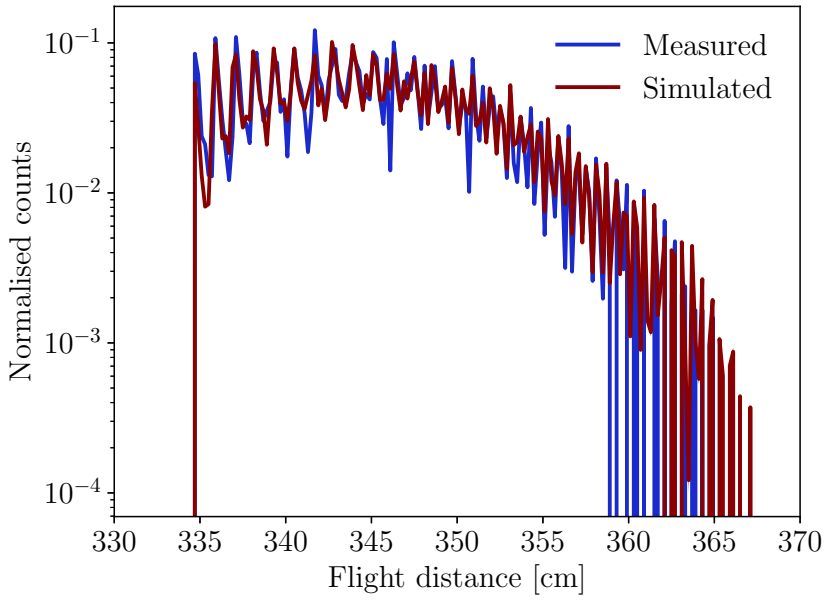

(b) Flight distance at 3.807 meV (4.6 Å).

Figure 8.4: Measured and simulated flight distance spectra at 3.678 (8.4a) and 3.807 meV (8.4b) incident neutron energies, normalised to area.

and simulated backgrounds is acceptable, considering the diversity of backgrounds of the existing chopper spectrometers. In essence, the measured and simulated ToF of elastic peaks agree well.

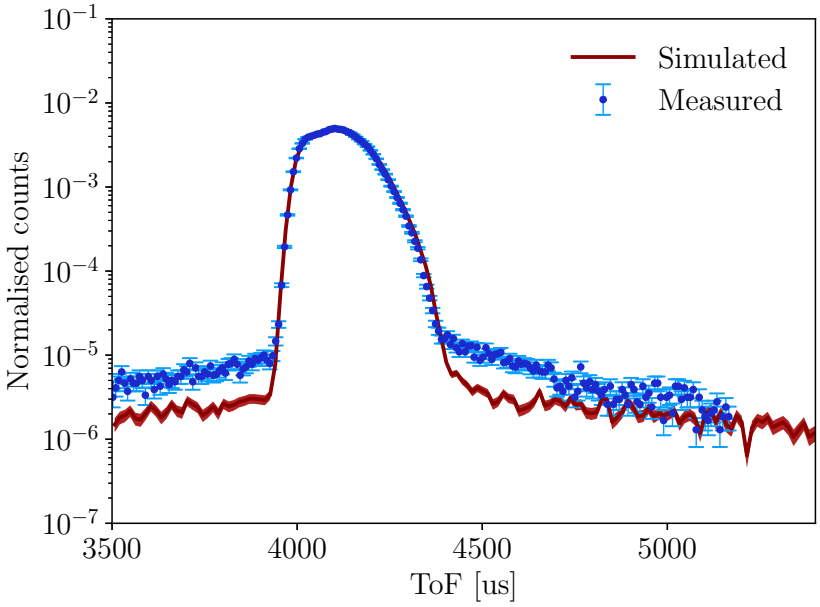

(a) ToF at 3.678 meV (4.7 Å).

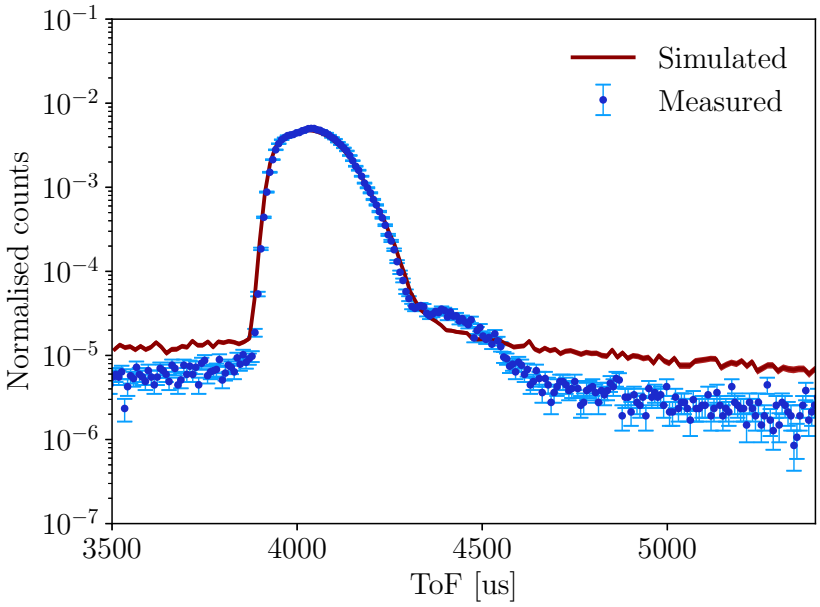

(b) ToF at 3.807 meV (4.6 Å).

Figure 8.5: Measured and simulated Time-of-Flight spectra at 3.678 (8.5a) and 3.807 meV (8.5b) incident neutron energies, normalised to area.

The energy transfer spectrum is defined as $E_{trf} = E_{initial} - E_{final}$, therefore the elastic peak appears centred around 0 meV, while the negative side represents the neutrons detected with energy gain, and the positive side represents the neutrons with real or apparent energy loss in comparison with the initial energy, as it is described

in Section 6.2. As it is shown in Figures 8.6a – 8.6c, the energy transfer spectra are reproduced by the simulation in all cases. In the case of 1.0 and 3.678 meV (9.0 and 4.7 Å) incident neutrons, below the aluminium Bragg-edge, the simulated background underestimates the measured one on both sides of the elastic peak. The discrepancy is about 80%. In the case of 3.807 meV (4.6 Å) incident neutrons, above the aluminum Bragg-edge, the simulated background slightly overestimates the measured one. The discrepancy is about 20% on the negative and 5% on the positive side of the elastic peak. The discrepancies in the background are attributed to the same reasons as for the ToF.

It also has to be mentioned that the two bumps at 0.25 and 0.5 meV only appear in the measured energy transfer. This effect is related to the instrument, as it also appears in the response of local ^{3}He-tubes. Its independence from the presence of the Multi-Grid detector is satisfactorily verified elsewhere. [81, 82] In essence the measured and simulated elastic peaks agree well and the backgrounds reasonably agree at all energies.

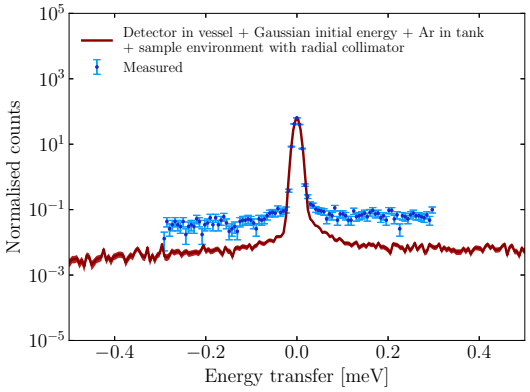

(a) Energy transfer at 1.0 meV (9.0 Å).

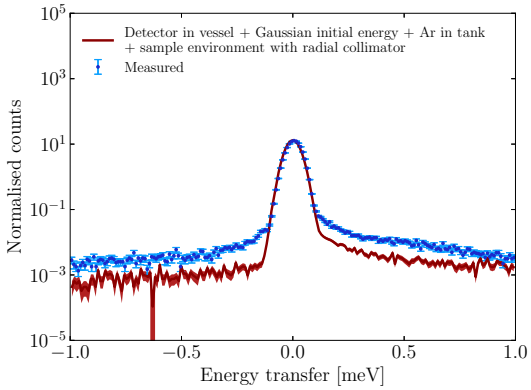

(b) Energy transfer at 3.678 meV (4.7 Å).

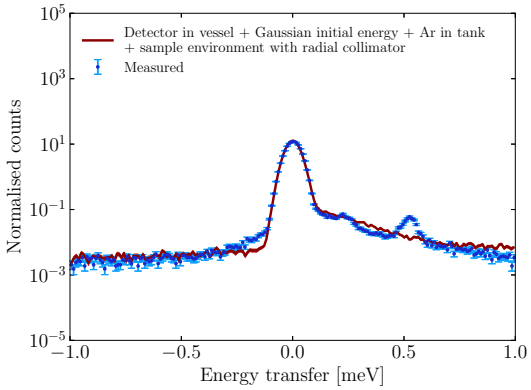

(c) Energy transfer at 3.807 meV(4.6 Å).

Figure 8.6: Measured and simulated energy transfer at 1.0 (8.6a), 3.678 (8.6b) and 3.807 meV (8.6c) incident neutron energy. Energy transfer spectra are normalised to area.

Based on the above presented agreement of simulated and measured results of independent experiments, the so-far developed Geant4 Multi-Grid detector model, and all the others reasonably and accurately derived from it, are regarded as validated. This now validated model is applicable to general Multi-Grid irradiation setups, providing a powerful tool in the development and optimisation of the Multi-Grid detector design and its tailoring for specific instruments, e.g. the CSPEC chopper spectroscope of the ESS.

Within the current thesis work, this model is already used to explore and understand the scattered neutron background in a single Multi-Grid detector module, for which study the afore-described CNCS detector module (see Section 6.2.2) is chosen as example. On the basis of the results of this study, a further model is derived to optimise the shielding against scattered neutron background in CSPEC instrument which is still being developed.

8.2 Scattering neutron background study

As measured and simulated energy transfer spectra are compared as part of the validation process of the implemented Multi-Grid detector model, these data have also been used for identifying and distinguishing the sources of neutron scattering. For this purpose, simulations are performed with the CNCS irradiation setup with level of detail. The background in energy transfer spectrum is chosen as 'figure of merit' defined as $E_{trf} = E_{initial} - E_{final}$, as it is introduced in Section 6.2.4.

The simulations are performed in the 1.0–8.0 meV incident neutron energy range (3.2–9.0 Å). The measured and simulated energy transfer spectra at 1.0, 3.678 and 3.897 meV incident neutron energy (9.0, 4.7 and 4.6 Å, respectively), below and above the aluminium Bragg edge are presented in Figures 8.6a – 8.6c respectively. Simulations are repeated adding one-by-one the geometrical and instrumental components (see Section 6.2.3) to the simulation. The spectra are compared in Figures 8.7a – 8.7c, while the obtained scattered neutron background data are given in Table 8.1. 'Bare detector grids' means two columns of grids, without the aluminium vessel.

In the energy transfer spectrum of the bare grids the elastic peak is mono-energetic at 0 meV and an asymmetric scattered neutron background also appears. The source of the background on the negative side is the neutrons that gained energy via inelastic scattering. The major source of higher and broader background on the positive side is the contribution of the elastically scattered neutrons. Figure 8.7c a fine structure of peaks also appears near the elastic peak on the positive side: this peak relates to the grid structure, the coherent scattering between the aluminium blades. Therefore this effect appears only above the aluminium Bragg-edge.

A similar spectrum is obtained with the complete detector model inside the vessel. The scattered neutron background increases in comparison to the case of the bare grids.

The effect of a Gaussian initial neutron energy distribution appears in Figures 8.7a – 8.7c; the initial energy distribution defines the shape of the elastic peak, while its impact on the background is negligible. The inclusion of the realistic Gaussian distribution only affects the background by the increased peak width. It is also apparent that the coherent scattering effects of the blades are hidden in the case of realistic incident neutron energy distributions.

Including the tank gas and components of the sample environment, a continuous, flat scattered neutron background appears in the spectra. In all cases, the asymmetric detector background has a comparable shape, appearing as a shoulder on the side of the elastic peak. While at 1.0 meV (Figure 8.7a) and 3.678 meV (Figure 8.7b) the background coming from the tank gas and the sample environment are comparable,

at 3.807 meV (Figure 8.7c) the aluminium sample environment becomes the dominant source of background, significantly increasing the background. This background is slightly reduced by the collimator, eliminating the scattered fraction of the cryostat and the rear of the aluminium window. However, the sample environment remains the main background source above the Bragg-edge even in the presence of the collimator.

In essence, in this Chapter the Geant4 Multi-Grid detector model got validated and was used to distinguish sources of scattered neutron background. It is shown that instrument related phenomena define the continuous, flat background and the primary distribution of the elastic peak in the energy transfer spectrum, while the intrinsic scattering in the detector has a comparable impact, determining the background distribution in the close proximity of the peak. This background component appears due to the scattering on the grid structure and is enhanced by the detector vessel. Hereinafter the model is used to optimise the detector design in order to reduce this intrinsic scattered neutron background (Chapter 9).

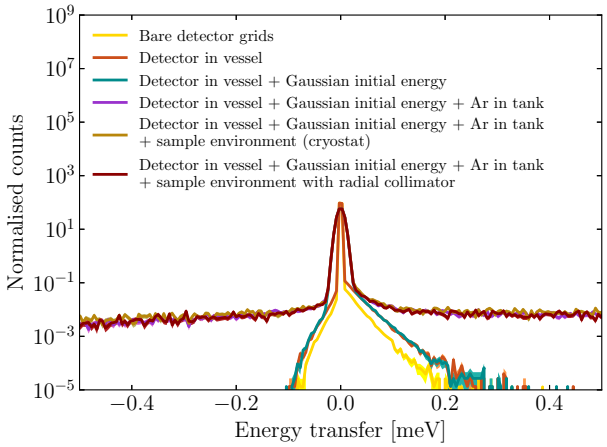

(a) Energy transfer at 1.0 meV (9.0 Å).

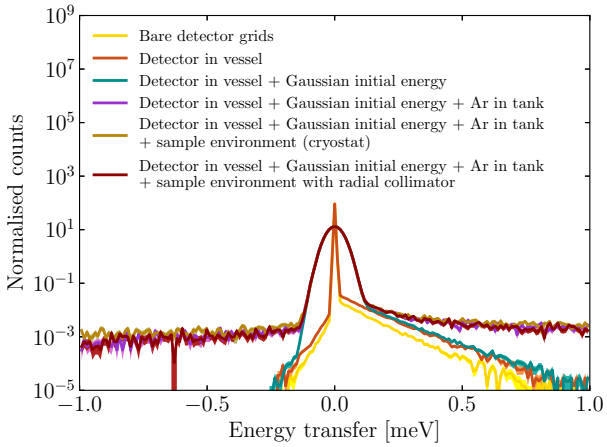

(b) Energy transfer at 3.678 meV (4.7 Å).

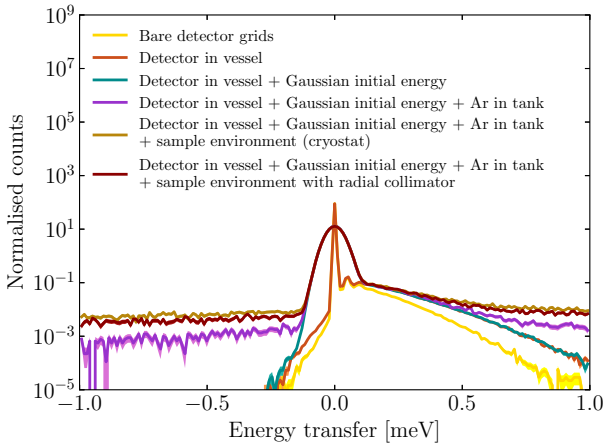

(c) Energy transfer at 3.807 meV (4,6 Å).

Figure 8.7: Comparison of the effect of different geometrical and instrumental parameters on energy transfer 1.0 (8.7a), 3.678 (8.7b) and 3.807 meV (8.7c) incident neutron energy. Energy transfer spectra are normalised to area.

Table 8.1: Simulated scattered neutron background ratio, normalised to elastic peak area (See Equation 9.1). The peak is defined in two ways: manually fitted peak width, and fix Δ0.052 meV and Δ0.24 meV peak width, equal to peak width of results with $E_{ini,Gaussian}$ for 1 meV and 3.678 and 3.807 meV, respectively.

	1.0 meV		3.678 meV		3.807 meV	
Model components	Adaptive peak width	Fix ± 0.026 meV width	Adaptive peak width	Fix ± 0.12 meV width	Adaptive peak width	Fix ± 0.12 meV width
	Background ratio [%]	Background ratio [%]	Background ratio [%]	Background ratio [%]	Background ratio [%]	Background ratio [%]
Bare grids	0.18	0.04	0.23	0.06	1.80	0.82
Detector in vessel	0.39	0.12	0.42	0.13	2.81	1.60
Detector in vessel + Gaussian E_{ini}	0.14	0.12	0.16	0.16	1.70	1.57
Detector in vessel + Gaussian E_{ini} + Ar in tank	1.31	1.32	1.10	1.09	2.64	2.57
Detector in vessel + Gaussian E_{ini} + Ar in tank + sample environment	1.72	1.71	1.42	1.42	6.90	6.62
Detector in vessel + Gaussian E_{ini} + Ar in tank + sample environment with collimator	1.30	1.26	1.08	1.07	5.11	4.88

Chapter 9

Detector optimisation with the Multi-Grid detector model

The implemented Geant4 model of the Multi-Grid detector was validated against measured data, and now can be used for optimisation, where the main goal of the process is to improve the SBR via background reduction.

The intrinsic scattered neutron background of the detector is explored and discussed in Section 8.1, revealing that the impact of the intrinsic detector background is comparable with the ones of instrument-related sources. These results and the upcoming ideas of the developers provide the basis and the approach for the vessel and shielding design optimisation.

In this thesis, three detector components are examined in terms of their impact on the scattered neutron background:

- Long blade coating
- Vessel window
- Internal detector shielding

9.1 Impact of long blade coating

The planned CSPEC detector module has an improved design in comparison with the so far built, tested and simulated demonstrators. One key difference is that, unlike the previous ones, in this module the long blades of the grids are under consideration to be coated with 1 μm boron-carbide [91]. The impact of the long blade coating is studied in the afore-defined reference detector (as illustrated in Figure 9.1), by comparing the signal (9.1a), the background (9.1b), the efficiency (9.1c, 9.1e) and the SBR (9.1d, 9.1f)

– as they are defined in Section 6.2 – for the wavelengths of interest, with and without the long blade coating.

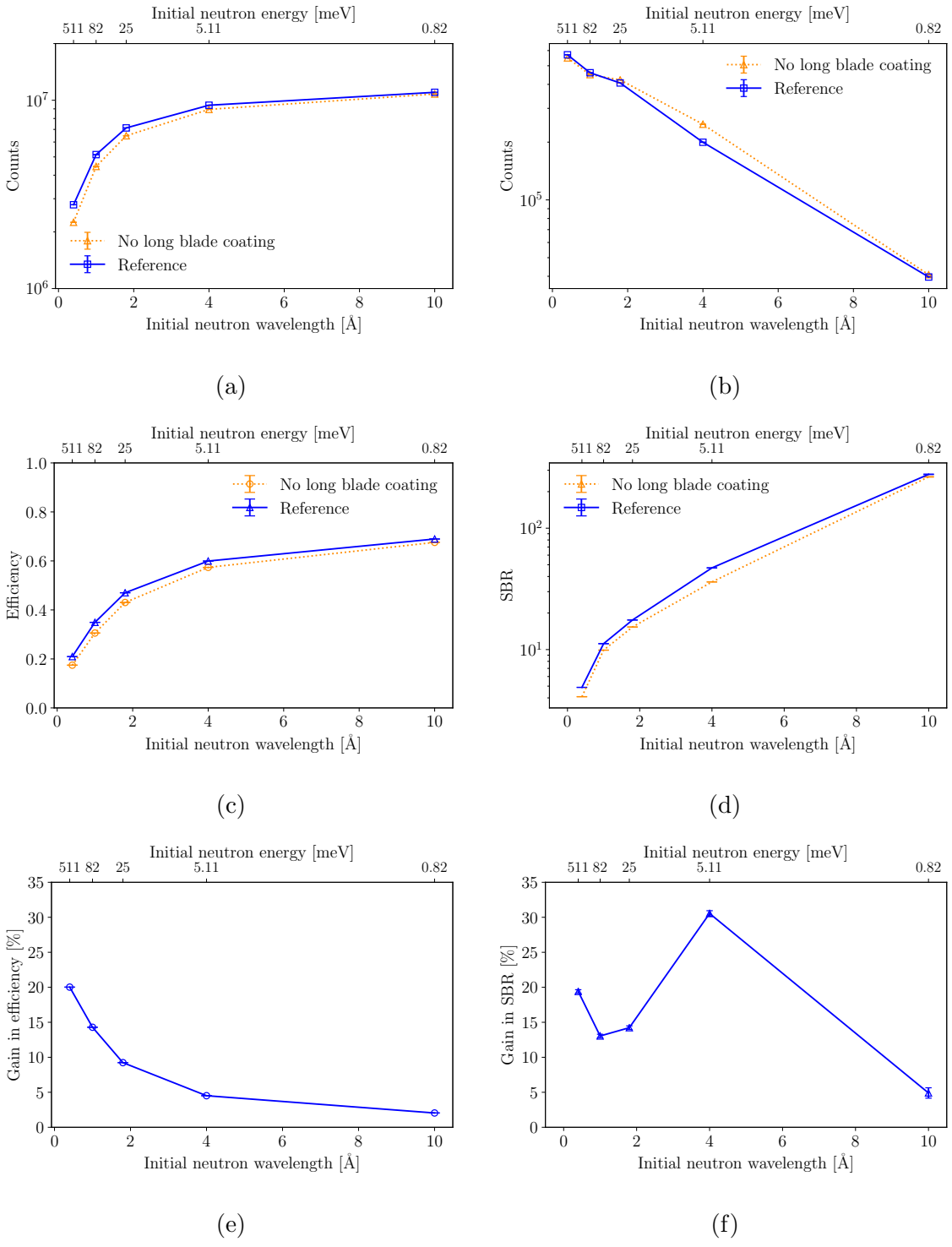

Figure 9.1: Simulated signal (a), background (b), neutron detection efficiency (c) and SBR (d) as functions of incident neutron wavelength in the unshielded reference detector, with and without coating on the long blades, and change of efficiency (e) and SBR (f) with long blade coating compared to no long blade coating case. The statistical uncertainties are too small to be discernible.

Figure 9.1c and 9.1e demonstrate a systematic efficiency increase in the presence of long blade coating for all wavelengths, with the increase being more significant, 9–20%, for the lower conversion efficiencies below 4.0 Å. Comparing the SBRs in Figure 9.1d and 9.1f, the SBR is increased in the presence of long blade coating at all wavelengths. The reason of this trend is that the long blade coating increases the signal (see 9.1a) via the increase of the total efficiency, and affects the scattered neutron background via two different aspects of the same process: on the one hand, with the increase of efficiency the probability of detection raises for all neutrons, both for signal and background counts, to different, energy dependent extent. This effect is dominant at low wavelengths, where the absorption cross-section of ^{10}B is low, as it is shown in Figure 9.1b. On the other hand, neutrons more probably get converted in the long blade coating, before they could scatter e.g. on the long blade or on side of the vessel. Therefore, a reduction of background appears at 4 Å in Figure 9.1b, where the Bragg-scattering on the aluminium has the dominant impact on the scattered neutron background. This way the shift in the background is determined by the competing reactions of scattering and absorption, and therefore by the respective cross-sections of aluminium and $^{10}B_4C$.

The SBR is determined by the combination of all the impacts on signal and background. In total, 5–31% increase of SBR can be reached in the whole studied wavelength region with the application of 1 μm long blade coating, as it is presented in Figure 9.1f.

Due to the positive impact on the efficiency and SBR in the low wavelength region, the application of long blade coating is recommended for the CSPEC instrument, if it can be done at moderate cost, and sufficient mechanical properties, and should be considered for any instrument with respect to the costs and requirements.

9.2 Vessel study

The scattering on the detector window – which is an important mechanical structure item as it is part of the vacuum interface – is a well-known challenge of neutron detector development. In the case of the Multi-Grid detector the comparable importance of the scattering on the aluminium vessel has been demonstrated in [92]. Therefore, as a first part of the optimisation, the impact of the vessel and the window on neutron scattering is studied. For this purpose, a set of simulations is performed on different configurations of the CNCS and CSPEC detector modules: in the case of the 'bare grids', the aluminium vessel is removed. For the other configurations, the vessel is

present, but the thickness of the entry window varies between 0 mm ('no window') and 22 mm.

9.2.1 Al window for the CNCS model

For the window scattering study on the CNCS demonstrator model the window thickness is defined as the sum of the vessel window and the entry grid thickness. The 0.5 mm grid entry thickness relates to the B_4C-coated blade, while bigger thicknesses indicate the presence of an additional entry blade. The effects of the other parts of the vessel, the side and the rear end are also considered. These components either appear with their realistic dimensions or are removed. Combination of thicknesses are tested and compared in the energy range of 1.0–8.0 meV in Figure 9.2.

For this study the detector background is defined as all neutron events in the energy transfer spectrum outside of the elastic peak. Since the peaks are sharp and well-identifiable, the peak boundaries are selected by-eye. The background is always given normalised to the peak:

$$background\ fraction = \frac{Total\ counts - Counts\ in\ peak}{Counts\ in\ peak} \tag{9.1}$$

The set of simulated setups and the obtained backgrounds are presented in Table 9.1. The simulations are performed with mono-energetic incident neutrons irradiating the entire detector volume. Sample environment and tank gas are not present.

Comparing the results in the whole energy range it is shown that except for the 22 mm total window thickness, which is unrealistically thick, the difference in the background is negligible. However, the presence of the side wall causes a significant increase in the background on the positive side of the spectrum. Therefore, a realistically chosen window thickness (2–5 mm) practically does not change the scattered neutron background, but the application of shielding on the inner wall of the vessel might be considered.

Table 9.1: Simulated scattered neutron background ratio, normalised to elastic peak area (See Equation 9.1). The peak was defined with manually fitted peak width.

				1.0 meV	3.678 meV	3.807 meV	8.0 meV
Vessel window	Grid entry	Vessel side	Vessel end	Background ratio [%]	Background ratio [%]	Background ratio [%]	Background ratio [%]
0 mm	0.5 mm	0 mm	0 mm	0.18	0.23	1.80	2.32
0 mm	0.5 mm	3 mm	0 mm	0.30	0.33	2.63	3.20
0 mm	2 mm	3 mm	0 mm	0.33	0.36	2.70	3.47
3 mm	2 mm	3 mm	0 mm	0.39	0.41	2.79	3.84
20 mm	2 mm	3 mm	0 mm	0.73	0.68	3.58	5.91
3 mm	2 mm	3 mm	10 mm	0.39	0.41	2.81	3.86

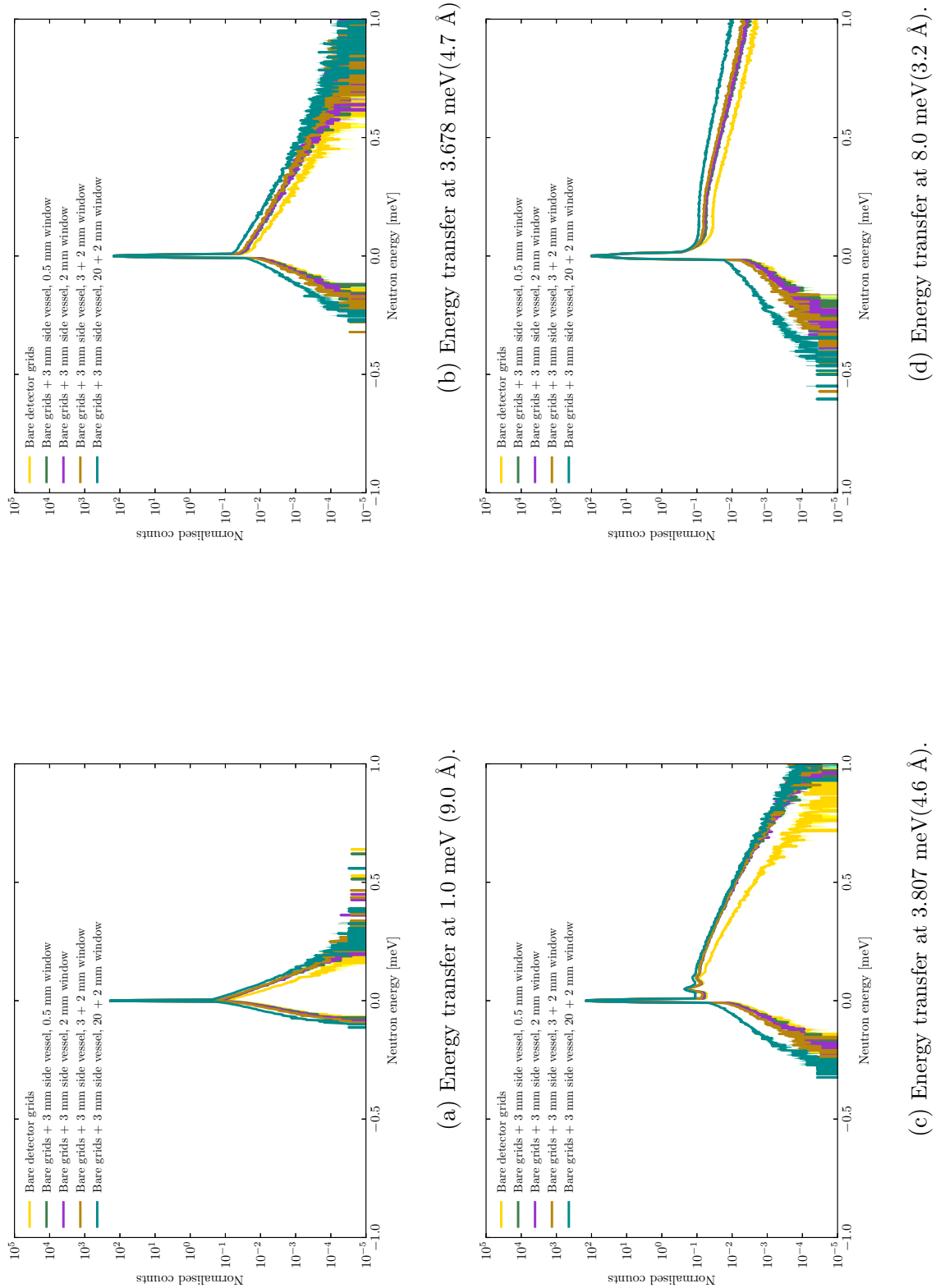

(a) Energy transfer at 1.0 meV (9.0 Å).

(b) Energy transfer at 3.678 meV(4.7 Å).

(c) Energy transfer at 3.807 meV(4.6 Å).

(d) Energy transfer at 8.0 meV(3.2 Å).

Figure 9.2: Simulated energy transfer with the presence of different window thicknesses and vessel components. Results are normalised to area.

9.2.2 Al window for the CSPEC model

The scattering on the detector window is studied in the CSPEC module as well, in the 'Reference detector', as introduced in Section 6.2.4. The different window thicknesses are compared by their impact on the obtained SBRs, as presented in Figure 9.3. The characteristics of the SBR are the same for all configurations, and a continuous decrease of SBR appears with the increased entry window thickness. Also, except of the bare grids and the 10 mm window case, which are unphysical and unrealistic cases respectively, no significant difference appears in the SBR. Therefore, to emphasize the discrepancies between the results of the different configurations, in Figure 9.4 the SBRs are normalised to the no window configuration, so the that impact of scattering on the window can be compared to the respective ideal case.

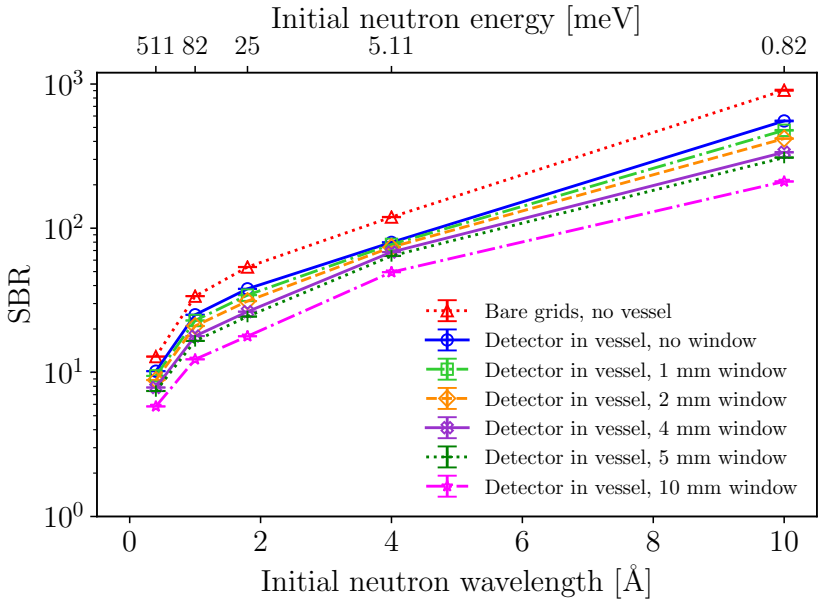

Figure 9.3: Simulated Signal-to-Background Ratio as a function of incident neutron wavelength, with different window thicknesses and vessel components in the reference detector. The statistical uncertainties are too small to be discernible.

In Figure 9.4 it is shown that for realistic window thicknesses (1–5 mm), the decrease of the SBR, compared to the ideal, no window configuration, is less than 20% at 4 Å, the wavelength for which the CSPEC instrument is optimised, and the scattering increase is roughly linear with window thickness. The difference is larger in the region where Bragg scattering is dominant, and at long wavelengths: up to 45% at the most extreme value. However, the incoming wavelength intensity is much larger for intermediate wavelengths around 4 Å at which the scattering is minimal. Given that the no window configuration is unphysical, and that the scattering increase is relatively small for an

increase in window thickness, it means that the currently applied 4 mm window, which has been chosen for structural purposes, is confirmed to be a suitable choice between performance and mechanical design optimisation.

On the other hand, it is also revealed that in the bare grids configuration the SBR is increased by 26–64% due to the lack of scattering on the vessel. The increase of SBR is higher for higher wavelengths, and being 50% at the optimal 4 Å. This confirms that a significant increase of the SBR can be achieved with suppression of scattering on the vessel, so internal side-shielding should be included.

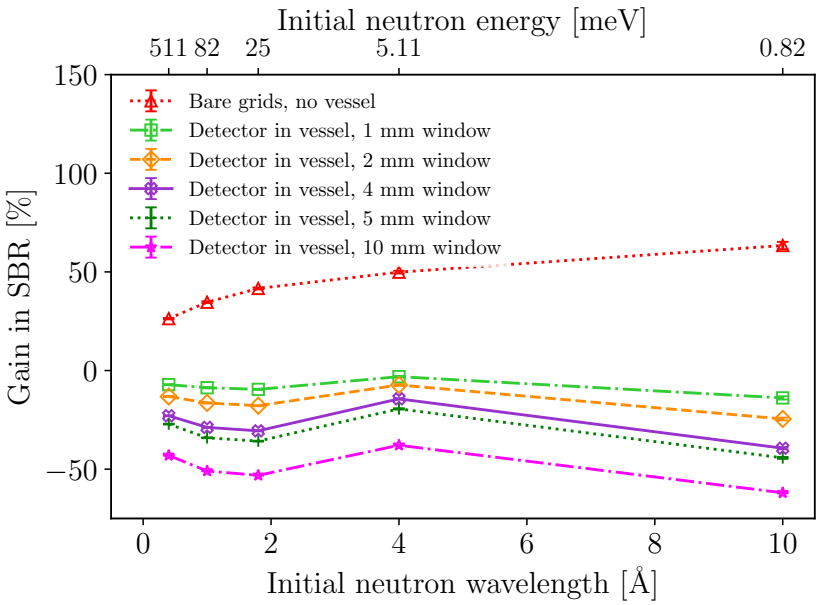

Figure 9.4: Simulated Signal-to-Background Ratio as a function of incident neutron wavelength, with different window thicknesses and vessel components, normalised to the unshielded reference detector with no window. The statistical uncertainties are too small to be discernible.

9.3 Study of shielding against scattering neutrons

The complex structure of the Multi-Grid detector is proven to be source of a significant intrinsic scattered neutron background [30, 92]. However, this complex geometry also leaves space for background reduction via optimisation of shielding design.

9.3.1 Scattered neutron background suppression with black shielding

To obtain an optimised shielding design, the background reduction capacity of the potential shielding geometry has to be determined. For this purpose 'black material' is applied for each afore-mentioned shielding geometry, to study their impact on the SBR through the whole 0.4–10.0 Å (511.3–0.8 meV) operational range of the CSPEC instrument. With the application of the black material, the highest obtainable background reduction can be determined for each shielding geometry. For this purpose different shielding topologies are applied both individually and in combination in the reference detector.

The evaluation of the background reduction capacity is performed based on the number of neutrons absorbed in every shielding volume, normalised to the incident neutrons (Figure 9.5). The neutrons absorbed by the converter are also displayed for the sake of completeness.

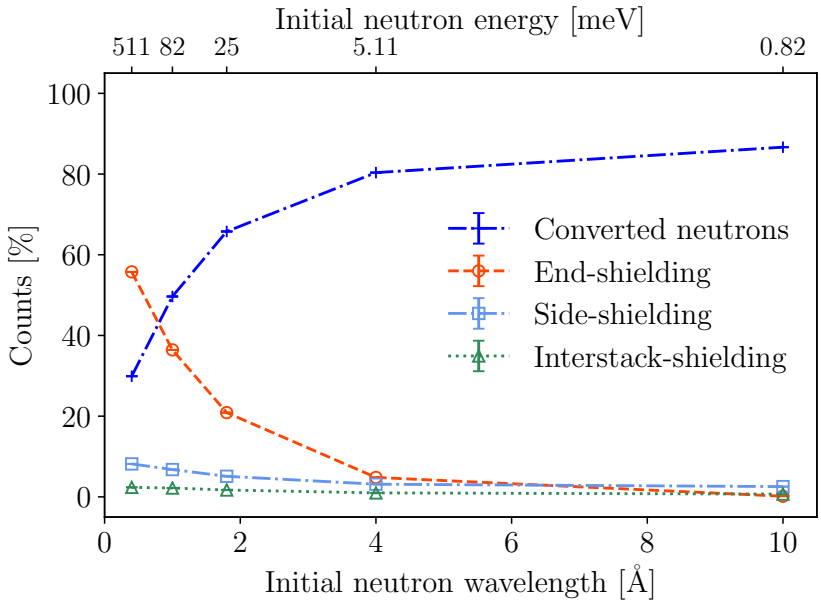

Figure 9.5: Neutron conversion and absorption is different shielding topologies with black material in the reference detector. The different shielding topologies are applied individually. The statistical uncertainties are too small to be discernible.

The neutron absorption in the end-shielding and the neutron conversion have similar, but opposed trend through the wavelength range. The reason for this is that these are competing processes; as the neutron absorption cross-section in the boron-carbide converter increases with the wavelength, more neutrons are converted, and fewer neu-

trons reach the end-shielding, so fewer neutrons are absorbed in the end shielding. However, the end-shielding can absorb a significant amount of neutrons below 4 Å (above 5.1 meV), and 56% of the neutrons can be absorbed in the end-shielding at 0.4 Å (511.3 meV). On the other hand at 10 Å (0.8 meV) the absorption in the end-shielding is practically zero, as the neutrons do not reach the end of the grid. It is also shown that the absorption is more even in the other two geometries, i.e. 8–2.5% of the neutrons are absorbed in the side-shielding, 8% at 0.4 Å (511.3 meV), and less than 2% is absorbed in the interstack-shielding.

Consequently, the end-shielding is the dominant shielding topology in the Multi-Grid detector, and there is a high background suppression potential in the low-wavelength region, where the SBR is the smallest.

The effect of the different shielding topologies on the SBR is also determined, as it is shown in Figure 9.6. The shielding topologies are added one-by-one to the simulation, starting from the reference detector. The SBR is increased in the whole wavelength range; the end-shielding has a high contribution in the low wavelength region, while the other two shielding geometries are responsible for the increase of SBR at high wavelengths. The relative increase of the SBR compared to the SBR of the unshielded reference detector is depicted in Figure 9.7, both for individually applied shielding topologies (9.7a) and for their combinations (9.7b).

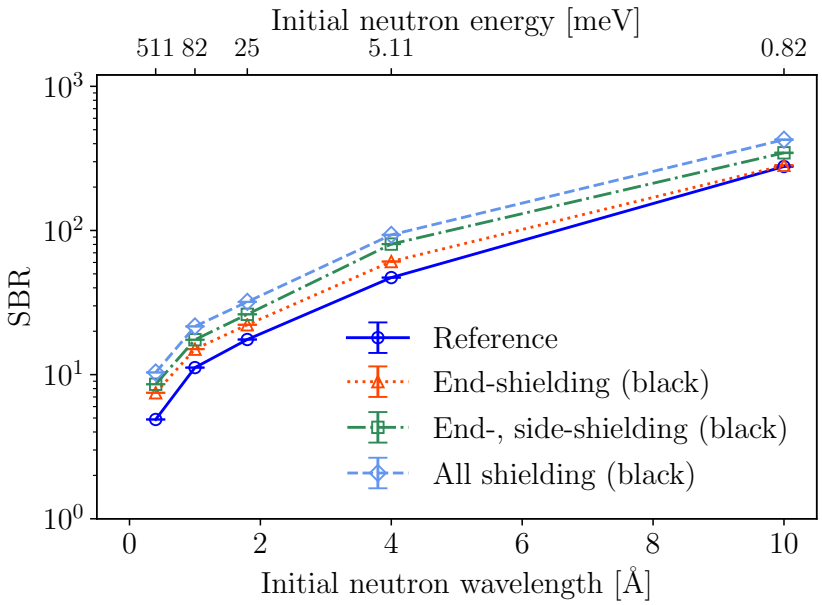

Figure 9.6: Simulated Signal-to-Background Ratio in presence of different shielding topologies with black material in the reference detector. The different shielding topologies are applied in combination. The statistical uncertainties are too small to be discernible.

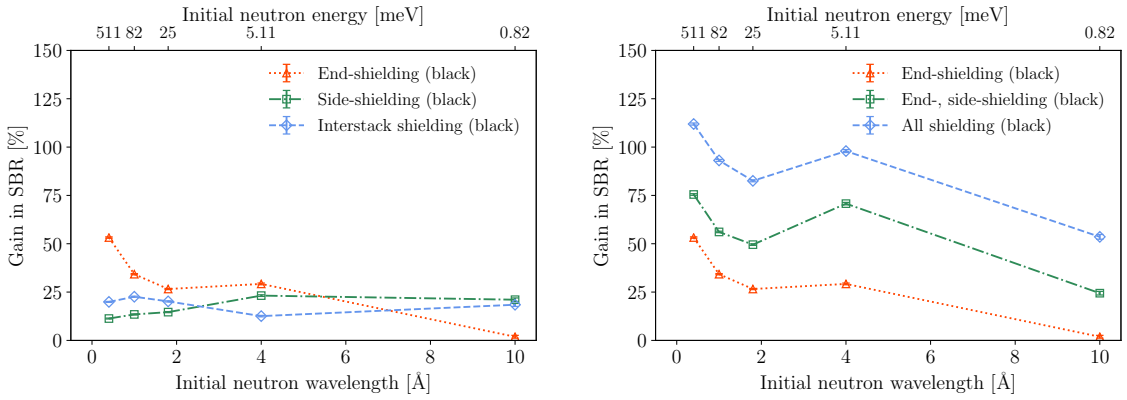

(a) (b)

Figure 9.7: Simulated Signal-to-Background Ratio in presence of different shielding topologies with black material, normalised to the unshielded reference detector. The different shielding topologies are applied individually (9.7a) and in combination (9.7b). The statistical uncertainties are too small to be discernible.

In Figure 9.7a the significance of the end-shielding is confirmed; the SBR is increased with 53–29% in the 0.4–4.0 Å (511.3–5.1 meV) region with the application of black material. Moreover, the increase is the highest in the low wavelength region, where the SBR otherwise is the lowest. The increase of SBR due to the presence of side-shielding is 11–23%, and 13–20% due to the interstack-shielding. It is important to highlight the opposite impact of the side-shielding and the interstack-shielding, that is most significant at 4.0 Å (5.1 meV); the side shielding has a higher impact at this wavelength and above, as the isotropic scattering becomes the dominant source of background. At 4.0 Å (5.1 meV) the majority of the scattered neutron background still comes from the Bragg-scattering from the rear blade of the grid. As the respective angle of the Bragg-scattering is 117°, the scattered neutrons in the Bragg-cone are targeted towards the vessel sides with 63° opening angle, so these neutrons do not reach the interstack-shielding. Therefore the interstack-shielding only absorbs the minority of neutrons scattered in the inner blades of the grids, and has a low impact at 4.0 Å (5.1 meV), but has higher impact at lower wavelength, where the overall background is higher due to the lower absorption cross-section of ^{10}B. All these phenomena emphasize the potential of a combined shielding design.

In Figure 9.7b the different shielding topologies are added one-by-one to the reference detector in order of their individually shown relevance. It is shown that the trend of the increase of the SBR is determined by effect of the end-shielding, although, the combination of the end-shielding and the side-shielding has a peak of SBR increase at 4.0 Å (5.1 meV), the optimal wavelength of the CSPEC instrument. This effect is

caused by the side-shielding, as it is explained in the case of the individual shielding topologies in Figure 9.7a. However, it is magnified in the combination of shieldings. In the presence of all three shielding topologies, the trend of the SBR increase is again dictated by the end-shielding, with a uniform increase along the whole studied wavelength range. It is demonstrated that the SBR can be increased by up to 75–24% with the combination of the end-shielding and the side-shielding, by 75% and 71% at 0.4 and 4.0 Å (511.3 and 5.1 meV), respectively. Also, the SBR can be increased up to 112–54% with the combination of all three shielding topologies, and by 112% and 98% at 0.4 and 4.0 Å (511.3 and 5.1 meV), respectively. To sum up, complex shielding design is confirmed to have a remarkable potential to increase the SBR via background suppression. This impact is higher in the low wavelength region, where the efficiency and the SBR are inherently lower, and it is proven that an ideal, combined shielding has the potential to increase the SBR by 98% at the 4.0 Å (5.1 meV) operating optimum of the CSPEC instrument, and to more than double it at 0.4 Å (511.3 meV).

9.3.2 Shielding optimisation in a Multi-Grid detector module for CSPEC instrument at ESS

The effectiveness of a combined shielding for background suppression has been proven in the previous section (Section 9.3.1). In order to obtain the best realisation of the ideal, combined shielding, common shielding materials (B_4C, Cd, Gd with polyethylene and LiF) are tested for the studied relevant shielding topologies. The impact of the different shielding materials are compared to that of the black material at each shielding geometries in Figure 9.8.

It can be seen that 1 mm of B_4C or Cd as end- (9.8a) or side-shielding (9.8b), and 2 mm of either of them as interstack-shielding (9.8c), practically have equal background suppression capacity with the black material in the respective topologies. It is also shown that the impact of the Gd-polyethylene mixture is also approximately same as the one of the black material through the whole studied wavelength range, except at 0.4 Å (511.3 meV), where the impact of Gd is significantly lower in the case of the end-shielding and side-shielding. The SBR is increased with the application of end-shielding by 53–47% in the case of black material, B_4C and Cd, and by 34% in the case of the Gd with polyethylene. The same SBR increases for the side-shielding are 11% and 3%, respectively. On the one hand, these results confirm the effectiveness of Gd as shielding material at higher wavelengths, on the other hand they highlight the impact of the carrier media, especially the thermal scattering on the high hydrogen-content of typical carriers, like acrylic paint, glue, etc.

In Figure 9.8 it is also shown that while the SBR can also significantly increase with the application of LiF shielding, this impact is much lower than the one of the previously discussed materials, due to their cross-sections (see Figure 3.3). The highest obtainable increase with LiF is 24% at 4 Å (5.1 meV) as end-shielding, and 22% at 4 Å (5.1 meV) as side-shielding. The respective quantities for black material are 29% and 23%.

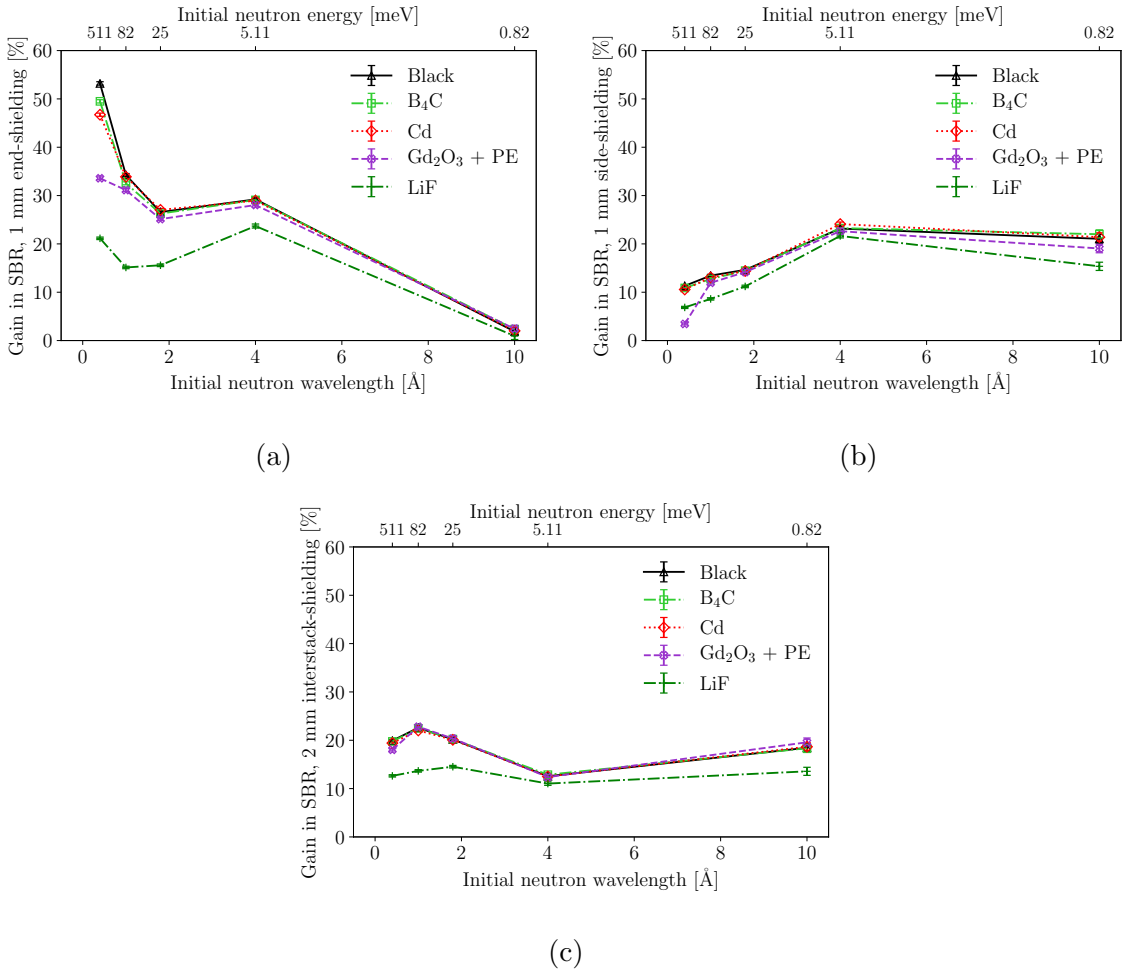

Figure 9.8: Simulated Signal-to-Background Ratio with different materials (including black material) for end- (9.8a), side- (9.8b) and interstack-shielding (9.8c), normalised to the unshielded reference detector. The statistical uncertainties are too small to be discernible.

As B_4C and Cd are proven to be an appropriate realisation of black material in the CSPEC detector module, they are also applied in the afore-described complex shielding design. The realistic, complex shielding's impact on the SBR is shown and compared to the impact of black shielding in Figure 9.9. It is revealed that whether B_4C (9.9a) or Cd (9.9b) are applied for each shielding topologies, the total increase of SBR meets the one of the black material, as expected on the basis of results of the individually

applied shielding geometries. However, it has to be noted that the pure Cd shielding is less effective at 0.4 Å (5.1 meV). Here the obtained SBR increase is 112% and 107% with black absorber and B_4C, and 102% with Cd, respectively. In Figure 9.9c it is also shown that this is the highest discrepancy between the impact of the different shielding combinations, and that the differences between the respective SBR increases are within 1–2% for all other wavelengths. The beneficial effect of the combined shielding also demonstrated in Figure 9.10 on the simulated ToF-spectrum: the background tail is cut down by one order-of-magnitude in the presence of the combined B_4C shielding.

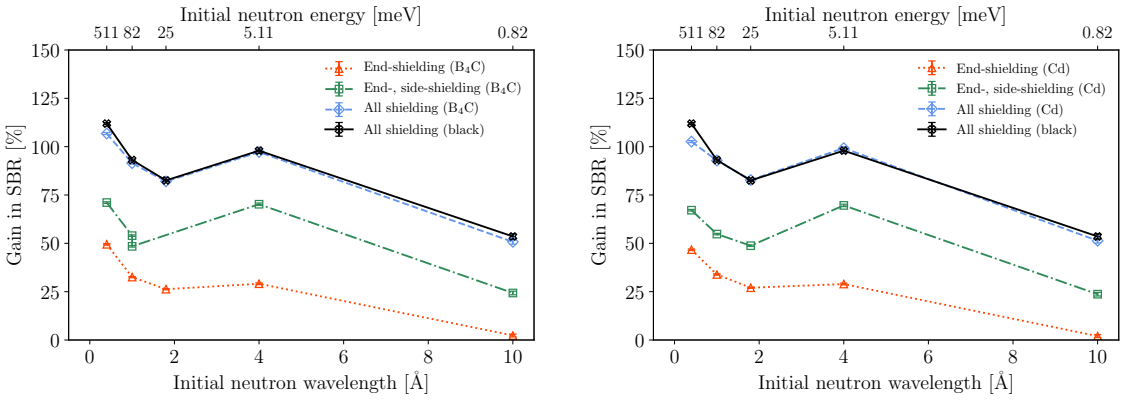

(a) (b)

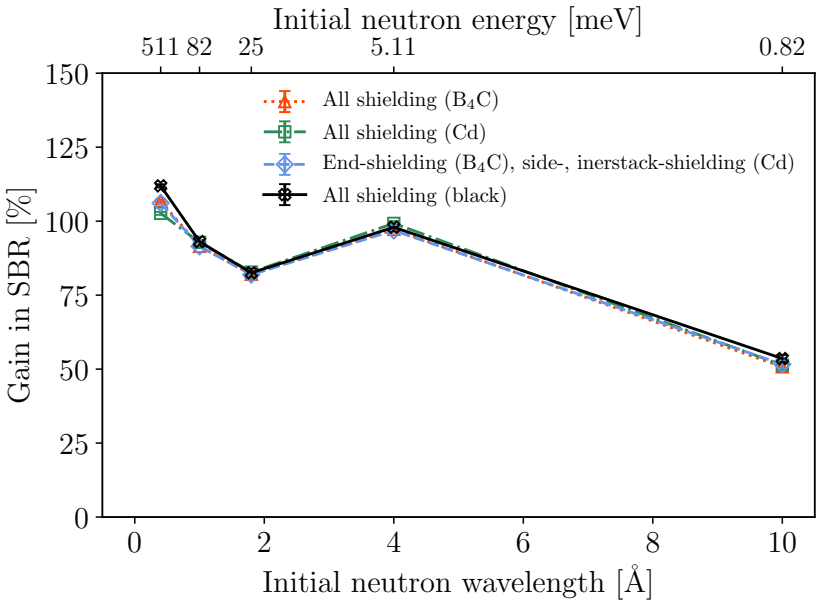

(c)

Figure 9.9: Simulated Signal-to-Background Ratio with combined shielding with boron-carbide (9.9a), cadmium (9.9a), and both of them (9.9c) compared to black material, normalised to the unshielded reference detector. The statistical uncertainties are too small to be discernible.

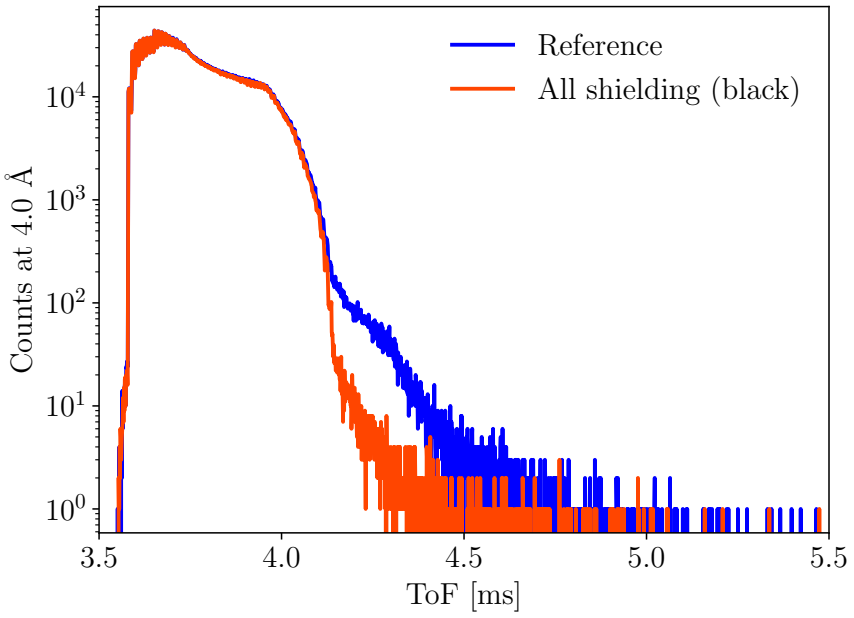

Figure 9.10: Comparison of ToF spectra with and without shielding at 4 Å initial neutron wavelength.

Accordingly, with a realistic, B_4C and/or Cd based complex shielding design the SBR can be increased sufficiently close to the maximum theoretically obtainable value with the current operational parameters and design of the CSPEC detector module. Gd is also proven to be a good shielding material, although the scattering on any carrier medium should be considered, especially at lower wavelengths. In essence, common shielding materials are proven to be satisfactory for the CSPEC detector, and details of the complex shielding design can be chosen with regard to additional criteria, like cost, availability and engineering requirements.

Chapter 10

Summary

A novel, holistic approach is presented for shielding optimisation and background reduction in Ar/CO_2-filled solid boron-converter based thermal and cold neutron detectors. The different sources of neutron-induced 'intrinsic' radiation background, – gamma and scattered neutron radiation produced within the detector itself, – are identified, distinguished, and quantified via detailed Monte Carlo simulations, and validated against analytical calculations and measured data.

As the potential activation of the counting gas is a generic problem for all large-volume Ar/CO_2-filled neutron detectors, the neutron activation of detector components is studied in a generic, easy-to-scale model, developed in MCNP6. The phenomenon of neutron activation is discussed both in terms of the produced gamma-background and its impact during the measurement, especially on the Signal-to-Background Ratio (SBR), and in terms of the potential activity emission of airborne radioactivity. For these purposes the produced flux and incident neutron energy dependent prompt- and decay-gamma yield of the counting gas and a typical aluminium housing are determined for standard ESS operational conditions, as well as the produced activity. All results are given and published in a ready-to-use and easy-to-scale form, providing input for quick and conservative estimations on activity-production and gamma-background in detector-development.

In regard of the various capacities of nuclear databases available for Monte Carlo modelling, the simulated results are compared to analytical calculations as well. With this a set of MCNP6.1 cross-section databases are also provided for Ar/CO_2 counting gas and aluminium detector housing estimated as Al5754, which both give good agreement with the analytical calculations, or give an acceptable, conservative estimation both for prompt gamma production and activity calculations. These databases are

recommended for use in more complex geometries, where the analytical calculations should be replaced by MCNP simulations.

It is revealed that, in accordance with the expectations, the total gamma yield and activity are all determined by the $^{27}Al/^{28}Al$ and $^{55}Mn/^{56}Mn$, and the $^{40}Ar/^{41}Ar$ content in the aluminium housing and the counting gas, respectively. Due to the short half-life of these isotopes the decay gamma-yield also appears during the irradiation, i.e. the measurement, and is comparable with the prompt-gamma yield. For the counting gas sourced gamma-background, the NTR (Neutron-to-Gamma Response ratio) is determined for typical neutron energies of ESS, revealing that the NTR changes within the range of $10^9 - 10^{10}$ for general boron-carbide-based detector geometries, and still being 10^5 even for beam monitors, having the lowest possible efficiency, and therefore the neutron-induced gamma-background is found to be negligible in terms of measurement.

In terms of activity emission, the counting gas activity was found to saturate at $1.28 \cdot 10^{-1}$ Bq/cm^3 under standard ESS operational conditions, from which a conservative $1.28 \cdot 10^6$ Bq/day activity production is expected. By varying the flush rate and storing the counting gas up to 1 day before release, only negligible levels of activity will be present in the waste Ar/CO_2 stream.

The other main source of intrinsic detector background is the scattered neutron background. This phenomenon became relevant for the newly developed boron-carbide-based neutron detector due to their complex aluminium structure. Due to this the scattered neutron background is studied in a specific large area detector, the Multi-Grid, via Geant4 simulations. A detailed, realistic, flexible and scalable Monte Carlo model of the detector is built and validated against measured data from demonstrator tests at IN6 and CNCS instruments at ILL and SNS, respectively. Measured ToF data are reproduced for the IN6 experiment both qualitatively (ToF - detection depth spectra) and quantitatively (ToF spectra) in the 3.1–4.9 meV energy region. The validated model is also adopted for a more extensive set of measurements using a Multi-Grid detector at CNCS, including a more complete setup description. The model is verified with the comparison of measured and simulated ToF and flight distance data and energy-transfer at 3.678 and 3.807 meV (below and above the aluminum Bragg edge at 3.74 meV).

With this model the sources of scattered neutron background and their impact on the SBR are distinguished in the CNCS detector model, revealing that the neutron scattering in the detector geometry (e.g. window, vessel, grid-structure) is minor in comparison with the effect of the scattering on instrument components: the tank gas and the sample environment; these are the major sources of the measured continuous

flat background. This is the first time sources of thermal neutron scattering background are modelled in a detailed simulation of detector response.

The developed validated model is finally applied for background suppression via optimisation of detector design, especially the development of complex internal detector shielding. The impact of different internal detector components is studied in the CSPEC and CNCS detector models in the 0.8–511 meV and 1–8 meV neutron energy regions.

The effect of the long blade coating on the efficiency and SBR is studied. It is revealed that the efficiency can be increased by 8–19%, and the SBR can be increased by 8–14% in the 5.1–511 meV energy region (4.0–0.4 Å) with the application of 1 μm $^{10}B_4C$ coating on the long blades. The increase is 8% and 13% at the 5.1 meV optimum of CSPEC, respectively. In terms of cost over neutron or SBR, the moderate increase in cost that can be expected by coating the long blades can be justified by the accompanying increase in SBR. The contribution of the vessel and window on scattering is also studied. It is shown that a decrease of SBR with the increasing window thickness remains acceptable for a realistic, 1–5 mm thickness increase: 35% maximum decrease with 5 mm thickness at 0.8 meV, and <10% decrease for all thicknesses at the 5.1 meV optimum of the CSPEC instrument. For this reason, the window thickness can be chosen by engineering requirements. The impact of the aluminium vessel of the detector on the scattering is also determined, and proven to be equal or higher than the scattering on the window, pointing out the necessity of background suppression via internal detector shielding. The background-reduction capacities of common shielding geometries, end-shielding, interstack-shielding and side-shielding are compared by applying a black material. It is demonstrated that the dominant shielding geometries are the end-shielding, absorbing 10–60% of neutrons above 5.1 meV, and the side-shielding, absorbing 5–10% of neutrons through the whole energy range.

In order to develop a combined internal shielding, common shielding materials, B_4C, Cd, Gd_2O_3 and LiF are tested for each shielding type, and 1 mm of B_4C or Cd is proven to provide equally good shielding as the total absorber. It is shown that with these materials as a combination of end-, side- and interstack-shielding, the SBR can be raised by 50–106% for 0.8–511 meV (0.4-–10 Å) region, respectively.

With this the potential of the holistic approach of background reduction via detailed Monte Carlo simulation is proven. The obtained results have served as input for detector design development and decision making in the ESS Detector Group. The developed and validated Geant4 Multi-Grid model became a potential tool for the op-

timisation of the detectors for the T-REX and the region VOR instrument, and also planned to be used in the future for full-scale detector simulations.

Acknowledgement

I would like to thank my supervisor, Dr. Péter Zagyvai for all his help and contribution during my PhD studies. This work has been supported by the In-Kind collaboration between ESS ERIC and the Centre for Energy Research of the Hungarian Academy of Sciences (MTA EK), and would like to express my gratitude to Prof. Dr. Richard Hall-Wilton for the opportunity to work with the ESS Detector group, and for his continuous support during all these years. I would like to thank Dr. Szabolcs Czifrus for his guidance in the MCNP simulations and the PhD School.

I would like to express my gratitude to Dr. Kalliopi Kanaki for her unabated moral and professional support through my whole work, her assistance with the Geant4 modelling and the endless proofreading; without her this thesis would not have been fulfilled.

I am thankful to my Head of Laboratory, Dr. Szabina Török, Director General Dr. Ákos Horváth and the MTA EK for all the opportunities and support through these years.

Furthermore I would like to acknowledge the ILL and the SNS for the measured data. A portion of this research used resources at the Spallation Neutron Source, a DOE Office of Science User Facility operated by the Oak Ridge National Laboratory. CNCS data was measured at SNS under ID IPTS-17219.

I would like to acknowledge the DMSC Computing Centre (https://europeanspallationsource.se/datamanagement-software/computing-centre) for providing computing resources.

Finally I would like to thank Dr. Anton Khaplanov for his assistance with the Multi-Grid detector, as well as Dr. Francesco Piscitelli, Dr. Thomas Kittelmann and all the members of the ESS Detector Group and the MTA EK Environmental Physics Laboratory; I am grateful that I could learn from Them.

Bibliography

[1] *European Spallation Source ESS ERIC*. URL: http://europeanspallationsource.se/.

[2] S. Peggs et al. *ESS Technical Design Report, ESS-2013-001*. Tech. rep. ESS, 2013. URL: https://europeanspallationsource.se/sites/default/files/downloads/2017/09/TDR_online_ver_all.pdf.

[3] *The Lund/LBNL Nuclear Data Search*. URL: http://nucleardata.nuclear.lu.se/toi/.

[4] D.A. Shea and D. Morgan. *The Helium-3 shortage: supply, demand, and options for congress*. Tech. rep. R41419. Congressional Research Service, 2010.

[5] F. Sauli. "Principles of operation of multiwire proportional and drift chambers". *CERN 77-09* (1977).

[6] F Sauli. *Gaseous Radiation Detectors: Fundamentals and Applications*. Cambridge Monographs on Particle Physics, Nuclear Physics and Cosmology. Cambridge University Press, 2014. DOI: 10.1017/CBO9781107337701.

[7] *International Collaboration for the Development of Neutron Detectors*. URL: http://icnd.org/.

[8] *Institute Laue-Langevin*. URL: http://www.ill.eu.

[9] *Forschungs-Neutronenquelle Heinz Maier-Leibnitz (FRM II)*. URL: http://www.frm2.tum.de/startseite/.

[10] *Linköping University*. URL: https://liu.se/en.

[11] C. Höglund et al. "B4C thin films for neutron detection". *J. Appl. Phys.* 111 (2012), p. 104908. DOI: 10.1063/1.4718573.

[12] C. Höglund et al. "Stability of $^{10}B_4C$ thin films under neutron radiation". *Radiation Physics and Chemistry* 113 (2015), pp. 14–19. DOI: 10.1016/j.radphyschem.2015.04.006.

[13] S. Schmidt et al. "Low-temperature growth of boron carbide coatings by direct current magnetron sputtering and high-power impulse magnetron sputtering". *Journal of Materials Science* 51.23 (2016), p. 10418. DOI: 10.1007/s10853-016-0262-4.

[14] K. Andersen et al. "10B multi-grid proportional gas counters for large area thermal neutron detectors". *Nucl. Instr. and Meth. A* 720 (2013), pp. 116–121. DOI: 10.1016/j.nima.2012.12.021.

[15] A. Khaplanov et al. "10B multi-grid proportional gas counters for large area thermal neutron detectors". *Neutron News* 23.4 (2013), pp. 20–25. DOI: 10.1080/10448632.2012.725329.

[16] L. Zanin et al. "The neutron moderators for the European Spallation Source". *J. Phys.: Conf. Ser.* 1021 (2018), p. 012066. DOI: 10.1088/1742-6596/1021/1/012066.

[17] F. Messi et al. "The Multi-Blade: The ^{10}B-based neutron detector for reflectometry at ESS". *Nuclear Inst. and Methods in Physics Research, A* xxx (2018), p. xxx. DOI: 10.1016/j.nima.2018.10.058.

[18] URL: https://europeanspallationsource.se/ess-mandate.

[19] B.T.M. Willis and C.J. Carlile. "Neutron Spectroscopy". In: *Experimental Neutron Scattering*. Ed. by B.T.M. Willis and C.J. Carlile. Oxford: Oxford University Press, 2009. Chap. 14-16, pp. 249–309.

[20] J. Ollivier, H. Mutka, and L. Didier. "The new cold neutron time-of-flight spectrometer IN5". *Neutron News* 21.2 (2010), pp. 22–25.

[21] W. Lohstroh et al. "ESS Instrument Construction Proposal C-SPEC - Cold chopper spectrometer" (2013).

[22] G.F. Knoll. *Radiation Detection and Measurement*. 4th ed. JohnWiley & Sons, Inc., 2010.

[23] D. Bódis. *Atommagsugárzások méréstechnikái*. TYPOTEX, 2009. ISBN: 978-963-9664-31-9.

[24] G.F. Knoll. "Radiation Detection and Measurement". In: 4th ed. JohnWiley & Sons, Inc., 2010. Chap. 5-6, pp. 131–207.

[25] B. Guerarad and J.-C. Buffet. US 2011215251. (Laue Max Inst, France), 2010.

[26] *ILL patent application FR 10/51502*. 2010.

[27] *The Cluster of Research Infrastructures for Synergies in Physics*. URL: www.crisp-fp7.eu.

[28] *BrightnESS*. URL: https://brightness.esss.se/.

[29] T. Brückel et al. "ESS Instrument Construction Proposal T-REX: A Time-of-flight Reciprocal space Explorer" (2015).

[30] J. Birch et al. "In-beam test of the Boron-10 Multi-Grid neutron detector at the IN6 time-of-flight spectrometer at the ILL". *J. Phys.: Conf. Ser.* 528.012040 (2014). DOI: 10.1088/1742-6596/528/1/012040.

[31] M. Anastasopoulos et al. "Multi-Grid Detector for Neutron Spectroscopy: Results Obtained on Time-of-Flight Spectrometer CNCS". *JINST* 12 (2017), P04030. DOI: 10.1088/1748-0221/12/04/P04030.

[32] J. Birch et al. "Investigation of background in large-area neutron detectors due to alpha emission from impurities in aluminium". *Journal of Instrumentation* 10 (2015), P10019. DOI: 10.1088/1748-0221/10/10/P10019.

[33] A. Khaplanov et al. "Investigation of gamma-ray sensitivity of neutron detectors based on thin converter films". *JINST* 8 (2013). DOI: 10.1088/1748-0221/8/10/P10025.

[34] G. Mauri et al. "Fast neutron sensitivity of neutron detectors based on boron-10 converter layers". *Journal of Instrumentation* 13 (2018), P03004. DOI: 10.1088/1748-0221/13/03/P03004.

[35] Byung Jin Jun et al. "Estimation of aluminium and argon activation sources in the HANARO coolant". *Nuclear Engineering and Technology (2014)* Vol. 42.2 (2010).

[36] M. Ajijul Hoq et al. "Estimation of ^{41}Ar activity and release rate from the TRIGA MARK-II research reactor". *Journal of Environmental Radioactivity* 153 (2016), pp. 68–72.

[37] C. Rojas-Palma et al. "Experimental evaluation of gamma fluence-rate predictions from argon-41 releases to the atmosphere over a nuclear research reactor site". *Radiation Protection Dosimetry* Vol. 108.2 (2004), pp. 161–168.

[38] B. Lauritzen et al. "Atmospheric dispersion or argon-41 from nuclear research reactor: measurement and modelling of plume geometry and gamma radiation field". *Int. J. of Environmental and Pollution* 20.1-6 (2013), pp. 47–54.

[39] J.J. Kunst et al. "Mediciones de Ar-41 y la preparaciónpara emergencias nucleares". In: *VIII Congresso Regiónal de Seguridad Radiologica y Nuclear, Congreso Latinoamericano del IRPA y el V Congreso Nacional de Protección Radiológica DSSA., 11 al 15 de octubre de 2010.* Medellín, Colombia, 2010.

[40] "Production and atmospheric release of activation products". In: *Savannah River Site Environmental Dose Reconstruction Project; Phase II: Source Term Calculation and Ingestion Pathway Data Retrieval; Evaluation of Materials Released from the Savannah River Site*. 2012. Chap. 4.3.

[41] M.J. McDonald et al. *Radioactive air effluent emission measurements at two research reactors.* URL: http://digital.library.unt.edu/ark:/67531/metadc678287.

[42] T. Chandrasekaran, J.Y. Lee, and C.A. Willis. *Calculation of Releases of Radioactive Materials in Gaseous and Liquid Effluents from Pressurized Water Reactors: PWR-GALE Code (NUREG-0017, Revision 1)*. Division of Systems Integration, Office of Nuclear Reactor Regulation, U.S. Nuclear Regulatory Commission, Washington, DC 20555-0001, 1985.

[43] *COUNCIL DIRECTIVE 2013/59/EURATOM*. 2013.

[44] *Radiological Safety Review of Siting Aspects of the ESS Technical Design Report*. Tech. rep.

[45] D. Ene et al. "Radiation Protection Studies for ESS Superconducing Linear Accelerator". *Progress in NUCLEAR SCIENCE and TECHNOLOGY* Vol. 2 (2011), pp. 382–388.

[46] K.G. Andersson and S.P. Nielsen. *External doses from the most important potential contaminants from routine airborne releases at ESS*. Tech. rep. SSM-2012-131-83. European Spallation Source ESS AB and DTU Nutech, Technical University of Denmark, 2012.

[47] *Evaluated Nuclear Data File.* URL: https://www-nds.iaea.org/exfor/endf.htm.

[48] V. Santoro et al. "MeV Neutron Production from Thermal Neutron Capture in ^{6}Li Simulated With Geant4". *J. Phys.: Conf. Ser.* 746 (2016), p. 012012. DOI: 10.1088/1742-6596/746/1/012012.

[49] *Mirrotron Radiation Shielding.* URL: https://mirrotron.com/en/products/radiation-shielding.

[50] *Mirrotron Ltd.* URL: https://mirrotron.com/en.

[51] *MCNP — A General Monte Carlo N-Particle Transport Code, Version 5*. LA-UR-03-1987. Los Alamos National Security, LLC. 2013.

[52] I. Lux and L. Koblinger. *Monte Carlo Particle Transport Methods: Neutron and Photon Calculation*. Tech. rep. Boca Raton: CRC Press, 1991.

[53] T. Kittelmann et al. "Monte Carlo Particle Lists: MCPL". *Comput. Phys. Commun.* 218 (2017), pp. 17–42. DOI: 10.1016/j.cpc.2017.04.012.

[54] *MCPL documentation and github repository*. URL: https://mctools.github.io.mcpl/.

[55] *MCPL 1.2.0 with native python support*. URL: https://github.com/mctools/mcpl/tree/v1.2.0.

[56] C. Zendler et al. *Neutron Optics and Shielding Guidelines, Requirements and Standards*. Tech. rep. ESS-0039408. European Spallation Source ESS ERIC, 2015.

[57] *GEANT4*. URL: http://geant4.cern.ch.

[58] S. Agostinelli et al. "Geant4: A simulation toolkit". *Nucl. Instr. and Meth. A* 506 (2003), pp. 250–303. DOI: 10.1016/S0168-9002(03)01368-8.

[59] J. Allison et al. "Geant4 developments and applications". *IEEE Trans. Nucl. Sci.* 53 (2006), p. 270. DOI: 10.1109/TNS.2006.869826.

[60] *NXSG4 website*. URL: http://cern.ch/nxsg4.

[61] T. Kittelmann and M. Boin. "Polycrystalline neutron scattering for Geant4: NXSG4". *Comput. Phys. Commun.* 189 (2015), pp. 114–118. DOI: 10.1016/j.cpc.2014.11.009.

[62] K. Kanaki et al. "Simulation tools for detector and instrument design". *Physica B, Proceedings of the ICNS conference* (2017). DOI: 10.1016/j.physb.2018.03.025.

[63] X.X. Cai and T. Kittelmann. *NCrystal: a library for thermal neutron transport in crystals*. URL: https://mctools.github.io/ncrystal/.

[64] T. Kittelmann et al. "Geant4 based simulations for novel neutron detector development". *J. Phys: Conf. Ser.* 513 (2014), p. 022017. DOI: 10.1088/1742-6596/513/2/022017.

[65] A. Vértes, S. Nagy, and Z. Klencsár. *Handbook of Nuclear Chemistry. Volume 3: Chemical Applications of Nuclear Reactions and Radiations*. 1st. Vol. 3. Kluwer Academic Publisher, 2003.

[66] A. Simonits, F. De Corte, and J. Hoste. "Single-Comparator Methods in Reactor Neutron Activation Analysis". *Journal of Radioanalytical Chemistry* Vol. 24 (1975), pp. 31–46.

[67] F. De Corte et al. "k_0-Measurements and Related Nuclear Data Compilation for (n, gamma) Reactor Neutron Activation Analysis". *Journal of Radioanalytical and Nuclear Chemistry* Vol. 133.No. 1 (1989), pp. 43–130.

[68] G.L. Molnár. *Handbook of Prompt Gamma Activation Analysis: with Neutron Beams*. 1st. Kluwer Academic Publisher, 2004.

[69] *Database for Prompt Gamma-ray Neutron Activation Analysis*. URL: https://www-nds.iaea.org/pgaa.

[70] MakeItFrom.com. *5754 Aluminium*. URL: https://www.makeitfrom.com/material-properties/5754-AlMg3-3.3535-A95754-Aluminum/.

[71] *Reference neutron activation library*. Tech. rep. IAEA-TECDOC-1285. IAEA, 2002.

[72] D.B. Pelowitz, ed. *MCNP6 ™ USER'S MANUAL*. Version 1.0. Los Alamos National Security, LLC. 2013.

[73] *TALYS*. URL: http://www.talys.eu/.

[74] J.L. Conlin et al. *Listing of Available ACE Data Tables*. Rev 4. Los Alamos National Security, LLC.

[75] J. Allison et al. "Recent developments in Geant4". *Nucl. Instrum. Meth. A* (2016). DOI: 10.1016/j.nima.2016.06.125.

[76] T. Kittelmann et al. "Geant4 based simulations for novel neutron detector development". *J. Phys.: Conf. Ser* Vol. 513 (2013). DOI: doi:10.1088/1742-6596/513/2/022017.

[77] T. Kittelmann et al. "Using backscattering to enhance efficiency in neutron detectors". *IEEE Transactions on Nuclear Science* 64.6 (2017), pp. 1562–1573. DOI: 10.1109/TNS.2017.2695404.

[78] *Cold neutron time-focussing time-of-flight spectrometes*. URL: https://www.ill.eu/instruments-support/instruments-groups/instruments/in6/description/instrument-layout/.

[79] *CNCS Cold Neutron Chopper Spectrometer at SNS*. URL: http://neutrons.ornl.gov/cncs.

[80] *CATIA6*. URL: https://www.3ds.com/products-services/catia/products/v6/.

[81] G. Ehlers et al. "The New Cold Neutron Chopper Spectrometer at the Spallation Neutron Source: Design and Performance". *Review of Scientific Instruments* 82.085108 (2011). DOI: 10.1063/1.3626935.

[82] G. Ehlers et al. "The New Cold Neutron Chopper Spectrometer at the Spallation Neutron Source - A review of the first 8 years of operation". *Review of Scientific Instruments* 87.093902 (2016). DOI: 10.1063/1.4962024.

[83] A. Khaplanov et al. "Multi-Grid detector design for direct geometry spectrometers CSPEC and T-REX at the ESS". *International Workshop on Position Sensitive Neutron Detectors PSND* (2018).

[84] E. Dian et al. "Suppression of intrinsic neutron background in the Multi-Grid detector". *JINST* (2018).

[85] P.P. Deen et al. "A design study of VOR: a Versatile Optimal Resolution chopper spectrometer for the ESS". *EPJ Web of Conferences* 83.03002 (2015). DOI: 10.1051/epjconf/20158303002.

[86] S.F. Mughabghab, M. Divadeenam, and N.E. Holden. "Neutron resonance parameters and thermal cross sections". Vol. 1 (1981) (1981).

[87] *NIST Neutron scattering lengths and cross sections*. URL: https://www.ncnr.nist.gov/resources/n-lengths/.

[88] S.T. Thornton and A. Rex. *Modern Physics for Scientists and Engineer*. Saunders College Publishing, 1993.

[89] E.A. Owen and E.L. Yates. "Precision measurements of crystal parameters". *Philosophical Magazine* 15 (1933), pp. 472–488.

[90] J. Peters et al. "Using Fermi choppers to shape the neutron pulse". *NIM A* 557.2 (2006), pp. 580–584. DOI: 10.1016/j.nima.2005.11.111.

[91] *Brightness deliverables*. URL: https://brightness.esss.se/about/deliverables.

[92] E. Dian et al. "Scattered neutron background in thermal neutron detectors". *Nuclear Inst. and Methods in Physics Research A* 902 (2018), pp. 173–183. DOI: 10.1016/j.nima.2018.04.055.

Appendix

Table A1: (n,γ) reaction cross sections at 25.30 meV [86], reaction products, their decay constants and respective uncertainties [3] ($\sigma(^{14}C)$ is from TENDL-2014 database [47]).

Isotope	Reaction product	σ [barn]	$\Delta\sigma$ [barn]	λ [s^{-1}]	$\Delta\lambda$ [s^{-1}]
^{36}Ar	^{37}Ar	$5.20 \cdot 10^{0}$	$5.00 \cdot 10^{-1}$	$2.29 \cdot 10^{-7}$	$2.61 \cdot 10^{-10}$
^{38}Ar	^{39}Ar	$8.00 \cdot 10^{-1}$	$2.00 \cdot 10^{-1}$	$8.17 \cdot 10^{-11}$	$9.11 \cdot 10^{-13}$
^{40}Ar	^{41}Ar	$6.60 \cdot 10^{-1}$	$1.00 \cdot 10^{-2}$	$1.06 \cdot 10^{-4}$	$1.16 \cdot 10^{-7}$
^{16}O	^{17}O	$1.90 \cdot 10^{-4}$	$1.90 \cdot 10^{-5}$	stable	-
^{17}O	^{18}O	$5.38 \cdot 10^{-4}$	$6.50 \cdot 10^{-5}$	stable	-
^{18}O	^{19}O	$1.60 \cdot 10^{-4}$	$1.00 \cdot 10^{-5}$	$2.58 \cdot 10^{-2}$	$7.66 \cdot 10^{-5}$
^{12}C	^{13}C	$3.53 \cdot 10^{-3}$	$2.00 \cdot 10^{-3}$	stable	-
^{13}C	^{14}C	$1.37 \cdot 10^{-3}$	$4.00 \cdot 10^{-5}$	$3.84 \cdot 10^{-12}$	$2.67 \cdot 10^{-14}$
^{14}C	^{15}C	$8.11 \cdot 10^{-7}$	-	$2.83 \cdot 10^{-1}$	$5.78 \cdot 10^{-4}$

Table A2: Cross section for Ar/CO_2 libraries used in MCNP6.1 simulations [74].

Element	Prompt gamma production		(n,γ) reaction rate calculation	
Ar	18000.42c	LANL	18036.80c	ENDF/B-VII.1
			18038.80c	ENDF/B-VII.1
			18040.80c	ENDF/B-VII.1
C	6000.80c	ENDF/B-VII.1	6012.00c	TALYS-2015
			6013.00c	TALYS-2015
			6014.00c	TALYS-2015
O	8000.80c	ENDF/B-VII.1	8016.00c	TALYS-2015
			8017.00c	TALYS-2015
			8018.00c	TALYS-2015

Table A3: (n,γ) reaction cross sections at 25.30 meV [86], reaction products, their decay constants and respective uncertainties [3].

Isotope	Reaction product	σ [barn]	$\Delta\sigma$ [barn]	λ [s^{-1}]	$\Delta\lambda$ [s^{-1}]
^{27}Al	^{28}Al	$2.31 \cdot 10^{-1}$	$3.00 \cdot 10^{-3}$	$5.15 \cdot 10^{-3}$	$2.76 \cdot 10^{-6}$
^{50}Cr	^{51}Cr	$1.59 \cdot 10^{1}$	$2.00 \cdot 10^{-1}$	$2.90 \cdot 10^{-7}$	$2.51 \cdot 10^{-11}$
^{52}Cr	^{53}Cr	$7.60 \cdot 10^{-1}$	$6.00 \cdot 10^{-2}$	stable	-
^{53}Cr	^{54}Cr	$1.82 \cdot 10^{1}$	$1.50 \cdot 10^{0}$	stable	-
^{54}Cr	^{55}Cr	$3.60 \cdot 10^{-1}$	$4.00 \cdot 10^{-2}$	$3.30 \cdot 10^{-3}$	$2.83 \cdot 10^{-6}$
^{63}Cu	^{64}Cu	$4.50 \cdot 10^{0}$	$2.00 \cdot 10^{-2}$	$1.52 \cdot 10^{-5}$	$2.39 \cdot 10^{-9}$
^{65}Cu	^{66}Cu	$2.17 \cdot 10^{0}$	$3.00 \cdot 10^{-2}$	$2.26 \cdot 10^{-3}$	$6.17 \cdot 10^{-6}$
^{54}Fe	^{55}Fe	$2.25 \cdot 10^{0}$	$1.80 \cdot 10^{-1}$	$8.05 \cdot 10^{-9}$	$8.85 \cdot 10^{-11}$
^{56}Fe	^{57}Fe	$2.59 \cdot 10^{0}$	$1.40 \cdot 10^{-1}$	stable	-
^{57}Fe	^{58}Fe	$2.48 \cdot 10^{0}$	$3.00 \cdot 10^{-1}$	stable	-
^{58}Fe	^{59}Fe	$1.28 \cdot 10^{0}$	$5.00 \cdot 10^{-2}$	$1.80 \cdot 10^{-7}$	$2.43 \cdot 10^{-11}$
^{24}Mg	^{25}Mg	$5.10 \cdot 10^{-2}$	$5.00 \cdot 10^{-3}$	stable	-
^{25}Mg	^{26}Mg	$1.90 \cdot 10^{-1}$	$3.00 \cdot 10^{-2}$	stable	-
^{26}Mg	^{27}Mg	$3.82 \cdot 10^{-2}$	$8.00 \cdot 10^{-4}$	$1.22 \cdot 10^{-3}$	$1.55 \cdot 10^{-6}$
^{55}Mn	^{56}Mn	$1.33 \cdot 10^{1}$	$2.00 \cdot 10^{-1}$	$7.47 \cdot 10^{-5}$	$5.79 \cdot 10^{-9}$
^{28}Si	^{29}Si	$1.77 \cdot 10^{-1}$	$5.00 \cdot 10^{-3}$	stable	-
^{29}Si	^{30}Si	$1.01 \cdot 10^{-1}$	$1.40 \cdot 10^{-2}$	stable	-
^{30}Si	^{31}Si	$1.07 \cdot 10^{-1}$	$2.00 \cdot 10^{-3}$	$7.34 \cdot 10^{-5}$	$1.40 \cdot 10^{-7}$
^{46}Ti	^{47}Ti	$5.90 \cdot 10^{-1}$	$1.80 \cdot 10^{-1}$	stable	-
^{47}Ti	^{48}Ti	$1.70 \cdot 10^{0}$	$2.00 \cdot 10^{-1}$	stable	-
^{48}Ti	^{49}Ti	$7.84 \cdot 10^{0}$	$2.50 \cdot 10^{-1}$	stable	-
^{49}Ti	^{50}Ti	$2.20 \cdot 10^{0}$	$3.00 \cdot 10^{-1}$	stable	-
^{50}Ti	^{51}Ti	$1.79 \cdot 10^{-1}$	$3.00 \cdot 10^{-1}$	$2.01 \cdot 10^{-3}$	$3.48 \cdot 10^{-6}$
^{64}Zn	^{65}Zn	$7.60 \cdot 10^{-1}$	$2.00 \cdot 10^{-2}$	$3.28 \cdot 10^{-8}$	$3.50 \cdot 10^{-11}$
^{66}Zn	^{67}Zn	$8.50 \cdot 10^{-1}$	$2.00 \cdot 10^{-1}$	stable	-
^{67}Zn	^{68}Zn	$6.80 \cdot 10^{0}$	$8.00 \cdot 10^{-1}$	stable	-
^{68}Zn	^{69}Zn	$1.00 \cdot 10^{1}$	$1.00 \cdot 10^{-1}$	$2.05 \cdot 10^{-4}$	$3.27 \cdot 10^{-6}$
^{70}Zn	^{71}Zn	$8.30 \cdot 10^{-2}$	$5.00 \cdot 10^{-3}$	$4.72 \cdot 10^{-3}$	$1.92 \cdot 10^{-4}$

Table A4: Cross section libraries for Al5754 used in MCNP6.1 simulations [74].

Element	Prompt gamma production		(n,γ) reaction rate calculation	
Al	13027.66c	ENDF/B-VI.6	13027.80c	ENDF/B-VII.1
Cr	24050.80c	ENDF/B-VII.1	24050.80c	ENDF/B-VII.1
	24052.80c	ENDF/B-VII.1	24052.80c	ENDF/B-VII.1
	24053.80c	ENDF/B-VII.1	24053.80c	ENDF/B-VII.1
	24054.80c	ENDF/B-VII.1	24054.80c	ENDF/B-VII.1
Cu	29063.80c	ENDF/B-VII.1	29063.80c	ENDF/B-VII.1
	29065.80c	ENDF/B-VII.1	29065.80c	ENDF/B-VII.1
Fe	26054.80c	ENDF/B-VII.1	26054.00c	TALYS-2015
	26056.80c	ENDF/B-VII.1	26056.00c	TALYS-2015
	26057.80c	ENDF/B-VII.1	26057.00c	TALYS-2015
	26058.80c	ENDF/B-VII.1	26058.00c	TALYS-2015
Mg	12000.62c	ENDF/B-VI.8	12024.80c	ENDF/B-VII.1
			12025.80c	ENDF/B-VII.1
			12026.80c	ENDF/B-VII.1
Mn	25055.62c	ENDF/B-VI.8	25055.80c	ENDF/B-VII.1
Si	14000.60c	ENDF/B-VI.0	14028.80c	ENDF/B-VII.1
			14029.80c	ENDF/B-VII.1
			14030.80c	ENDF/B-VII.1
Ti	22000.62c	ENDF/B-VI.8	22046.80c	ENDF/B-VII.1
			22047.80c	ENDF/B-VII.1
			22048.80c	ENDF/B-VII.1
			22049.80c	ENDF/B-VII.1
			22050.80c	ENDF/B-VII.1
Zn	30064.80c	ENDF/B-VII.1	30064.00c	TALYS-2015
	30066.80c	ENDF/B-VII.1	30066.00c	TALYS-2015
	30067.80c	ENDF/B-VII.1	30067.00c	TALYS-2015
	30068.80c	ENDF/B-VII.1	30068.00c	TALYS-2015
	30070.80c	ENDF/B-VII.1	30070.00c	TALYS-2015

New scientific results

1. I developed a general MCNP model for the neutron activation in Ar/CO_2-filled detectors with aluminium housing. I determined the neutron induced activity, decay and prompt-gamma yield of 80/20% by volume Ar/CO_2 and Al5457 materials of this typical detector, irradiated with mono-energetic beams in the range of 0.6–10 Å incident neutron energy. I optimised the selection of data from appropriate cross-section libraries to be used for further similar studies, giving sufficient agreement with the analytical calculations in terms of spectra, yield (max. 5–10% difference for main components) and activity (agreement within the margin of estimated uncertainty). I studied the activation of ^{40}Ar as source of gamma background for neutron signal and as source of activity release. I found that the typical daily activity production in Ar/CO_2-filled detectors, e.g. a large area detector of a chopper spectrometer, is $1.3 \cdot 10^6$ Bq/day (with 1.8 Å neutron irradiation of $\sim$107 cm^3 volume), which can be reduced to a negligible level (considering the targeted few GBq/day total release of the facility) with 1 day retention. I also determined a particular Signal-to-Background Ratio (SBR), with the background limited to the prompt- and decay-gamma yield of the counting gas, and I found that the SBR is between 10^9-10^{10} for the whole energy range, meaning that the neutron induced gamma background of the Ar/CO_2 counting gas is negligible and no suppression is required.

2. I developed a detailed, realistic and scalable Geant4 model of the solid ^{10}B-enriched boron-carbide converter based, Ar/CO_2-filled Multi-Grid detector. The model was developed within the ESS Coding Framework, where I used the NXSG4 and NCrystal tools for handling the crystal structure of specific materials, therefore the effects of neutron absorption, coherent and incoherent scattering were simulated. This is the first implementation of scattering model in cold neutron scattering, which allows quantifying continuous scattered neutron background effects, they are narrower that the apparent resolution. The modelled background levels are 5–7 orders-of-magnitude lower that the always present

elastic peak. The models given in **Thesis 1** and **Thesis 2** allow a detailed understanding of very low level gamma and scattered neutron background effects, giving a new approach for neutron detector development and optimisation of design for best available SBR.

3. I derived the models of two demonstrators from the general scalable model of **Thesis 2**: the 6-column Multi-Grid demonstrator detector that had been tested on the IN6 at ILL and the 2-column Multi-Grid demonstrator detector that had been tested on the CNCS at SNS. With these I validated the built model against the measured data both qualitatively (matching scattering profiles) and quantitatively within a sufficiently low margin of error. For this purpose I reproduced the measured Time-of-Flight spectra and the studied scattering phenomena from the IN6 experiment with 4.1, 4.6 and 5.1 Å incident neutrons. I also reproduced Time-of-Flight, energy transfer and flight distance results from the CNCS experiment, within a sufficiently low margin of error in terms of the elastic peak, and the profile of the scattered neutron background. In addition, in the CNCS model I simulated several detector and instrument effects (e.g. scattering on the detector grid, the detector vessel, the Ar/CO_2 tank gas and a simplified sample environment) that had appeared in the measured data sets at different energies in 1.0–8.0 meV incident neutron energy range.

4. I performed a simulation study on the 2-column Multi-Grid demonstrator model of **Thesis 3** and determined the impact of various effects apparent in the scattering neutron background on the measured data, e.g. Time-of-Flight, energy transfer, flight distance. In the simulation I highlighted the background contribution of the different neutron scattered components, e.g. scattering on the detector grid, the detector vessel, the Ar/CO_2 tank gas and a simplified sample environment. I found that the contribution of scattered neutron background from the detector is 10% of the total simulated background below the aluminium Bragg edge, and 60% above the Bragg edge. The detector's scattered neutron background contribution is 0.1–2% of the elastic peak for the whole energy range, evenly given by the grid structure and the housing. This background contribution shows high energy-dependence and scales with the volume. Therefore, these sources of background have to be considered and optimised for full-scale detectors.

5. Due to **Thesis 4**, I performed a simulation study on the aluminium detector window as a source of scattering neutron background with different incident neutron energies in the range of 1.0–8.0 meV. I determined the scattering neutron

rate coming from the sidewalls of the aluminium vessel and the entrance window at different thicknesses and incident neutron energies. I showed that below the aluminium Bragg edge, the background contribution of the neutron scattering on the detector frame and aluminium vessel is 0.2–0.4% of the elastic peak, that is negligible. Above the Bragg edge the total background contribution is 1.7–4% of the elastic peak. I found that with a realistic 2–5 mm window thickness 80–96% of the total scattered neutron background contribution of the detector and the vessel is given by the detector frame and the sidewalls of the vessel. Therefore, the aluminium window has only a minor contribution to the scattered neutron background, and its thickness can be optimised for engineering requirements, without any relevant influence on detector operation.

6. On the basis of **Thesis 4** and **Thesis 5**, I used the developed and validated Geant4 detector model to reduce the intrinsic neutron scattering in the Multi-Grid module of the CSPEC Cold Chopper Spectrometer of ESS. I performed this study with two different approaches. On one hand, as the conversion layer can also be interpreted as shielding, I determined the effect of the long blade coating on the efficiency and SBR. I concluded that the efficiency can be increased by 8–19%, and the SBR can be increased by 8–14% in the 5.1–511 meV energy region with the application of 1 μm $^{10}B_4C$ coating on the long blades. In terms of cost over neutron or SBR, the moderate increase in cost that can be expected by coating the long blades can be justified by the accompanying increase in SBR. On the other hand, I determined the background-reducing capacity of common shielding geometries, end-shielding, interstack-shielding and side-shielding, by applying black material. I showed that the most effective shielding geometries are the end-shielding, absorbing 10–60% of neutrons above 5.1 meV, and the side-shielding, absorbing 5–10% of neutrons through the whole energy range, while the interstack-shielding, that is the most difficult to apply, has only minor importance. Common shielding materials, B_4C, Cd, Gd_2O_3 and LiF are tested for each shielding type, and 1 mm of B_4C or Cd is proven to be equally efficient shielding as the total absorber. With these materials as a combination of end-, side- and interstack-shielding, the SBR can be raised by 50–106% for the 0.81–511 meV region.

Additional acknowledgement

Hereby the Author of this Thesis would like to express her gratitude towards the Members of the Exam Committee, Prof. Dr. Attila Aszódi, Dr. Imre Szalóki (Budapest University of Technology and Economics, Hungary), Dr. Márton Markó and Dr. Alex Szakál (Wigner RCP, Hungary) for their contribution in the defence. Furthermore, the Author would like to acknowledge Dr. Dániel P. Kis (Budapest University of Technology and Economics, Hungary), Dr. Ralf Engels (Forschungszentrum Jülich, Germany) and Dr. Dezső Varga (Wigner RCP, Hungary), the opponents during the defence process. This Thesis greatly improved and gained its final form thank to their detailed and thoughtful comments.